



UNIVERSIDAD NACIONAL
AUTÓNOMA DE
MÉXICO

UNIVERSIDAD NACIONAL AUTÓNOMA DE MÉXICO

PROGRAMA DE MAESTRÍA Y DOCTORADO EN
INGENIERÍA

CENTRO DE INVESTIGACIÓN EN ENERGÍA

ESTUDIO EXPERIMENTAL DE FLUJOS
EN DISPOSITIVOS DE BOMBEO Y
AGITACIÓN ELECTROMAGNÉTICOS

TESIS

QUE PARA OBTENER EL GRADO DE

DOCTOR EN INGENIERÍA

ENERGÍA - SISTEMAS ENERGÉTICOS

P R E S E N T A:

MICHEL ALEJANDRO RIVERO CORONA

DIRECTOR DE TESIS:

DR. SERGIO CUEVAS GARCÍA



2012



Universidad Nacional
Autónoma de México

Dirección General de Bibliotecas de la UNAM

Biblioteca Central



UNAM – Dirección General de Bibliotecas
Tesis Digitales
Restricciones de uso

DERECHOS RESERVADOS ©
PROHIBIDA SU REPRODUCCIÓN TOTAL O PARCIAL

Todo el material contenido en esta tesis esta protegido por la Ley Federal del Derecho de Autor (LFDA) de los Estados Unidos Mexicanos (México).

El uso de imágenes, fragmentos de videos, y demás material que sea objeto de protección de los derechos de autor, será exclusivamente para fines educativos e informativos y deberá citar la fuente donde la obtuvo mencionando el autor o autores. Cualquier uso distinto como el lucro, reproducción, edición o modificación, será perseguido y sancionado por el respectivo titular de los Derechos de Autor.

JURADO ASIGNADO

Presidente: Dr. Eduardo Ramos Mora

Secretario: Dr. Sergio Cuevas García

1er. Vocal: Dr. Jorge Antonio Rojas Menéndez

2do. Vocal: Dr. Raúl Alejandro Ávalos Zúñiga

3er. Vocal: Dr. Martín de Jesús Nieto Pérez

Lugares donde se realizó la tesis:

CENTRO DE INVESTIGACIÓN EN ENERGÍA - UNAM (México)
ILMENAU UNIVERSITY OF TECHNOLOGY[§] (Alemania)

TUTOR:

Dr. Sergio Cuevas García

[§]Sólo se realizó la parte experimental del Capulo III.

RESUMEN

Esta tesis está enfocada principalmente al análisis experimental de distintos flujos magnetohidrodinámicos (MHD) que tienen lugar en dispositivos que usan fuerzas electromagnéticas para bombear, monitorear o agitar fluidos eléctricamente conductores, tanto electrolitos como metales líquidos. La interacción de campos magnéticos con corrientes eléctricas (inducidas o aplicadas) que circulan en líquidos conductores crean la fuerza de Lorentz que da lugar a una variedad de patrones de flujo que muestran un amplio comportamiento dinámico. El propósito principal de esta tesis es proporcionar un entendimiento físico más profundo de algunos de estos flujos, además de desarrollar metodologías para su análisis. El estudio está motivado por las distintas aplicaciones en microfluídica (bombeo MHD) y en el procesamiento electromagnético de materiales (agitación MHD y Velocimetría por Fuerza de Lorentz) en donde los flujos MHD juegan un papel importante. Se estudian tres diferentes problemas. En la primera parte analizamos analítica y experimentalmente las consecuencias de considerar deslizamiento en la interfaz fluido-pared en microbombas MHD. Se muestran los modelos uni- y bi-dimensionales más usados en la descripción de microbombas MHD. Asimismo se investiga la influencia en el flujo de considerar diferentes combinaciones de las condiciones de frontera de deslizamiento y no-deslizamiento. La validación de los modelos se hizo con datos experimentales disponibles en la literatura. Adicionalmente, este análisis es complementado con el estudio experimental del flujo de un electrolito en una bomba MHD a escala milimétrica. A pesar de que el experimento no se realizó en condiciones de microfluídica (microescala), se observaron flujos muy interesantes mediante Velocimetría por Imágenes de Partículas. En la segunda parte, flujos de metal líquido a través de campos magnéticos localizados no uniformes se caracterizaron mediante Velocimetría Doppler Ultrasónica (UDV). Primero se estudia el flujo de metal líquido que pasa entre dos imanes rectangulares con tamaños menores que el ancho del canal. El flujo es producido por una bomba de inducción MHD a base de imanes permanentes rotando. Segundo, se analiza el flujo producido por el arrastre de un imán permanente sobre la superficie libre de metal líquido en reposo. Además, se hace la caracterización del flujo de GaInSn a la entrada y salida de un imán con una dimensión mayor al ancho del canal. Con base en los resultados se obtiene el flujo másico. La parte experimental de esta sección se realizó en las instalaciones de la Universidad Tecnológica de Ilmenau, Alemania. Por último se presenta el diseño y análisis de un dispositivo de agitación MHD a base de un campo magnético localizado rotatorio en coordenadas cilíndricas. El campo magnético es producido por un arreglo circular de hasta cinco imanes, 12.7 mm de diámetro, ubicados equidistantemente. Las mediciones de la componente radial de la velocidad se hacen mediante UDV y se analizan usando la transformada rápida de Fourier (FFT). El flujo es también se caracterizado mediante la visualización de las oscilaciones de la superficie libre. Se propone una estructura tridimensional del flujo que es consistente con las mediciones.

ABSTRACT

This thesis was devoted mainly to the experimental analysis of different magneto-hydrodynamic (MHD) flows that take place in devices that use electromagnetic forces to pump, monitor or stir electrically conducting fluids, both electrolytes and liquid metals. The interaction of magnetic fields with electric currents (either induced or applied) circulating in conducting liquids creates a Lorentz force that gives rise to a variety of flow patterns that show a rich dynamic behaviour. The main purpose of this thesis is to provide a deeper physical understanding of some of these flows and to develop methodologies for their analysis. The study is motivated by several applications in microfluidics (MHD pumping) and in electromagnetic processing of materials (MHD stirring and Lorentz Force Velocimetry) where MHD flows play a key role. Three different problems are studied. In the first part we analyse analytically and numerically the consequences of considering fluid/wall slippage in MHD micropumps. One- and two-dimensional flow models commonly used to describe MHD micropumps are revisited and different combinations of slip and no slip conditions at the walls of the micropump are investigated focusing on its influence on the flow rate. Validation of the results is made with available experimental data. Additionally, the analysis is complemented with the experimental study of an electrolytic flow in a MHD pump at millimetric scale. Although the experiment was not performed at microfluidic conditions, interesting flow patterns are observed through Particle Image Velocimetry. In the second part, liquid metal flows past localized and non-uniform magnetic fields are characterized by Ultrasound Doppler Velocimetry (UDV). First, a pump driven flow in a duct of constant rectangular cross-section that passed through the gap of two permanent rectangular magnets smaller than the duct's width is considered. Second, the flow generated by a rectangular magnet dragged upon the free surface of a quiescent liquid metal layer is explored. Additionally, characterisation of a liquid metal channel flow in a fringing magnetic field is done and the mass flow rate determined. The experimental part of this analysis was performed at the facilities of the Ilmenau University of Technology, Germany. Finally, the design and analysis of a liquid metal MHD stirring device based on a localized rotating magnetic field in a cylindrical container is presented. The magnetic field is produced by a circular array of up to five permanent magnets, 12.7 mm in diameter, equidistantly located. The radial velocity component was recorded using Ultrasound Doppler Velocimetry (UDV) and analysed through the Fast Fourier Transform. The flow is also characterized by visualizing the free surface oscillations. A three dimensional flow structure which is consistent with the observed features is proposed.

CONTENTS

1	Introduction	1
1.1	Overview	1
2	Flow in magnetohydrodynamic pumps	7
2.1	Theoretical analysis of the slip condition in MHD micropumps	7
2.1.1	A simple hydraulic resistance model	10
2.1.2	Formulation of the problem	12
2.1.3	Hartmann flow between infinite plates with slip	14
2.1.4	Flow in a rectangular duct with slip at the Hartmann walls	15
2.1.5	Flow in a rectangular duct with slip at the side walls	18
2.1.6	Flow in a rectangular duct with slip at all walls	21
2.1.7	Comparison of model results with experimental data	23
2.1.8	Conclusions	25
2.2	Experimental study of a MHD pump in an open channel	26
2.2.1	Experimental Setup	27
2.2.2	Results	29
2.2.3	Hydrodynamic zone	29
2.2.4	Pumping zone	32
2.2.5	Conclusions	34
3	Duct flows in localized and non-uniform magnetic fields	37
3.1	Liquid metal flow past a magnetic obstacle	37
3.1.1	Magnetic obstacle in a rectangular duct	39
3.1.2	Magnetic obstacle in free surface flow	42
3.2	Electromagnetic flow control channel	43
3.2.1	Experimental facility	45
3.2.2	Duct flow in a non-uniform magnetic field	46
3.2.2.1	Hydrodynamic flow upstream the magnet system	48
3.2.2.2	MHD flow downstream the magnet system	52
3.2.2.3	Calculation of flow rate	53
3.3	Conclusions	55
4	Electromagnetic stirring with localized rotating magnetic field	57
4.1	Introduction	57
4.2	Experimental setup	60
4.3	Results	63
4.3.1	Methodology	63
4.3.2	UDV analysis	63
4.3.2.1	Proposed flow patterns	70
4.3.2.2	Velocity fluctuations	71
4.3.3	Image processing	74
4.3.3.1	UDV and Image Processing results comparison	81

4.4	Conclusions	83
5	Concluding remarks	85
A	MHD equations	87
	References	93

Chapter 1

Introduction

In this chapter an overview of some of the main applications of magnetohydrodynamics (MHD) which provide a motivation for the study of the basic phenomena explored in this work are presented. In particular, the role of MHD in the Electromagnetic Processing of Materials (EPM) and in microfluidics is highlighted. In addition, the fundamental equations of MHD are presented.

1.1 Overview

Many natural and man-made flows are influenced by magnetic fields. The galactic magnetic fields affect the formation, dynamics and evolution of stars and galaxies^[1]. In turn, the magnetic fields of the Earth and the Sun are induced by the fluid motions in their cores, a phenomenon that is usually known as the dynamo effect^[2-4]. In addition to interesting technological applications of magnetic fields for energy production, there are many industrial applications where the use of magnetic fields may help to improve or control a given process. For instance, in metallurgical industry, magnetic fields are commonly used to stir^[5], levitate^[6], splash^[7], heat^[8,9] and pump^[10,11] liquid metals, among others applications^[12]. On the other hand, in the last two decades, the tendency to miniaturization of processes has open a new area of application of magnetic fields, namely, microfluidics^[13-15], where microelectromechanical systems (MEMS) are used. In this systems, magnetic fields can be used for many different purposes such as stirring, pumping, controlling and monitoring of conducting fluids, mainly electrolytes, chemical or biological fluids^[16,17].

The branch of physics that deals with all these topics is Magnetohydrodynamics. MHD studies the motion of electrically conducting fluids (no magnetizable) in the presence of magnetic fields and sometimes is also referred as “hydromagnetics” or “magneto-fluid dynamics”. The motion of a conducting fluid in an existing magnetic field will induce electric currents in the medium. In turn, these currents will produce an induced magnetic field which modifies the existing field. Additionally, the interaction of induced and applied magnetic fields with electric currents circulating in the fluid generates a body force, the Lorentz force, that affects the

velocity field. In general, we can say that the main characteristic of MHD flows is that velocity and magnetic fields are coupled. However, the strength of this coupling is determined by a dimensionless parameter called the magnetic Reynolds number, $Re_m = UL\mu\sigma$, which can be interpreted as the ratio of the induced and applied magnetic fields, where U and L are the characteristic velocity and length, respectively, while σ is the conductivity of the fluid and μ its magnetic permeability. For instance, in order for the dynamo effect to arise, $Re_m > 1$, this means that the velocity and magnetic fields are strongly coupled and that one is able to modify the other. On the other hand, in most of the industrial and technological applications as well as in laboratory scale experiments where liquid metals or electrolytes are used, $Re_m \ll 1$, and therefore, the coupling between these two vector fields is broken in one direction. In other words, magnetic field is able to modify the velocity field through the action of magnetic forces but the influence of the velocity field on the magnetic field is negligible.

Let us summarize the fundamental equations governing MHD flows. This set of equations is composed by the electromagnetic field equations in its pre-Maxwellian form and the fluid dynamics equations[§], namely,

$$\nabla \cdot \vec{u} = 0 , \quad (1.1)$$

$$\frac{\partial \vec{u}}{\partial t} + (\vec{u} \cdot \nabla) \vec{u} = \frac{1}{\rho} \nabla p + \nu \nabla^2 \vec{u} + \frac{1}{\rho} \vec{j} \times \vec{B} , \quad (1.2)$$

$$\nabla \times \vec{E} = -\frac{\partial \vec{B}}{\partial t} , \quad (1.3)$$

$$\nabla \times \vec{B} = \mu \vec{j} , \quad (1.4)$$

$$\nabla \cdot \vec{B} = 0 , \quad (1.5)$$

$$\vec{j} = \sigma \left(\vec{E} + \vec{u} \times \vec{B} \right) . \quad (1.6)$$

where u , p , j , B and E are the velocity, pressure, electric current density, magnetic and electric fields, respectively. In turn, ρ and ν are the density and kinematic viscosity of the fluid, respectively. Countless attempts of solving these equations by analytical and numerical procedures in a variety of natural, industrial, and academic problems have been reported in the literature, mainly since the second half of last century. In fact, the numerical simulation of different MHD flows is a very active research topic that, as many others, has strengthened its capabilities due to recent advances in computing science. In particular, the Centro de Investigación en Energía of the Universidad Nacional Autónoma de México (CIE-UNAM) is currently engaged in an effort to develop numerical methods for the numerical simulation of MHD flows. It is expected, however, that numerical results are supported by experimental information that may provide confirmation of theoretical predictions. Nevertheless, experimental results of MHD flows are rather limited

[§]A more detailed explanation can be found in Appendix A.

and therefore, new data obtained with a sound experimental basis are always welcome. It is in this context that the present thesis aims to contribute by providing experimental data for some MHD flows of interest.

As previously mentioned, in part the motivation for some of the flows explored in this work comes from the possibilities that MHD offers in microfluidics. In fact, many new chemical, medical, and biological applications rely on microfluidic devices, known as micro Total Analysis Systems (μ TAS). These are systems in which several chemical or biological techniques, or almost any classical laboratory method, can be accomplished on *chips* small enough to fit in the palm of a hand. These are commonly named *Lab on a Chip*. In all these systems tiny volumes of a fluid, as small as some *pl*^[18,19] ($10^{-9}ml$), *fl*^[20] ($10^{-12}ml$) or even *al*^[21] ($10^{-15}ml!$), need to be moved within different parts of the device. Just for the sake of comparison, 1 *ml* is equivalent to 20 droplets of water. With the aim of transport fluid at these scales, several options have been proposed in the literature, including mechanical and nonmechanical micropumps whose characteristics have been analysed in specialized reviews^[15,22-25]. Among different possibilities, magnetohydrodynamic (MHD) micropumps have attracted the attention of many researchers due to certain advantages such as simple fabrication process, the absence of moving parts, low voltage operation, and the possibility to achieve relatively high flow rates, being able to produce forward and reverse flows^[26-28]. MHD micropumps are nonmechanical devices that use an electromagnetic force, the Lorentz force, as the driving source in the flow. Although MHD pumps have been widely explored in the literature, the present work aims at contributing in some aspects that deserve a deeper understanding. In particular, the theoretical analysis of the effect of the slip condition on MHD micropumps and the experimental measurement of the flow field in a conduction MHD pump.

On the other hand, magnetic fields have been widely used since long ago for different technological applications related with material processing. However, a more rational use of electromagnetic fields for industrial applications began in the last two decades of twentieth century^[2]. The term *Electromagnetic Processing of Materials* (EPM) was coined to denominate this technological area. EPM is a multidisciplinary area that involves different fields such as magnetohydrodynamics (MHD), heat and mass transfer, thermodynamics, electrochemistry, plasma physics and other branches of physics, material science, and engineering. A schematic view of the multiple applications of EPM is shown in Figure 1.1^[29]. The disciplines that constitute the foundations of EPM are represented as the roots of a tree while the branches include most of the applications and processes related with this area. In fact, not all applications or processes are included in this tree but it just tries to illustrate the wide range of areas and applications that the EPM gathers. In chapter 3, where experiments on liquid metal electromagnetic stirring with localized magnetic fields is addressed, a more extensive review of EPM is presented.

The increasing demand of high quality metals and low consumption energy processes makes necessary a good understanding of how electromagnetic interac-

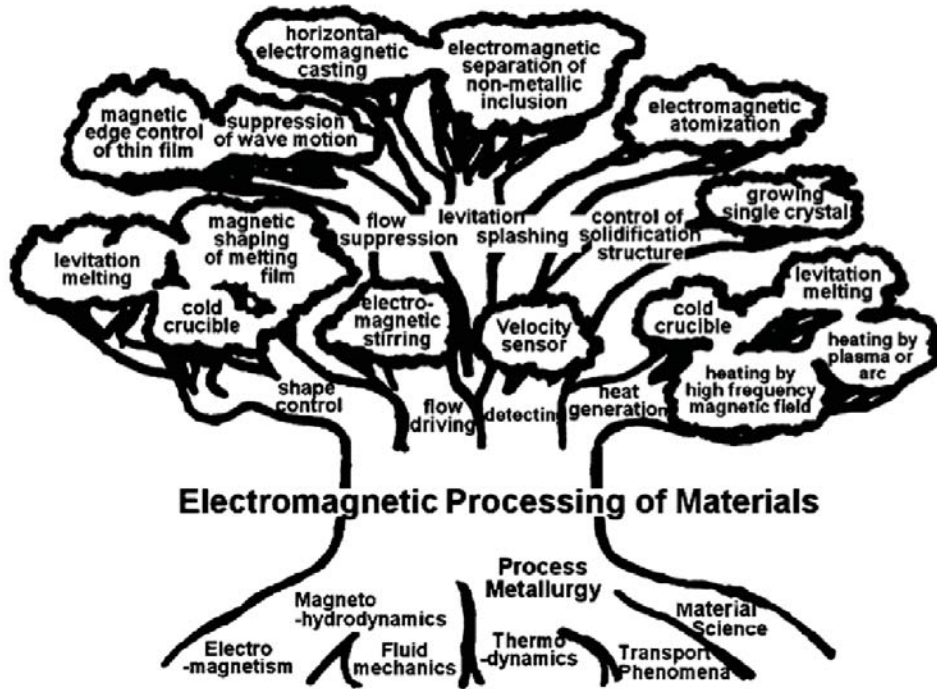


Fig. 1.1. Tree of electromagnetic processing of materials (taken from Ref. [29]).

tions may help to improve conventional procedures and lead to cleaner and more efficient processes. With this motivation, in this work we explore experimentally from the basic point of view different liquid metal MHD flows in ducts or containers which have the characteristic feature of taking place under localized or non-uniform magnetic fields. While flows under uniform magnetic fields have been widely explored, flows in localized fields are less known but they are interesting from the fundamental and applied points of view. In fact, it has been recently shown theoretically^[30–33] and experimentally^[34] that a localized magnetic field may act as an obstacle for the flow and produce flow patterns that resemble those of flows past bluff bodies. For this reason the term *magnetic obstacle* has been coined^[30] to characterise the action of a localized magnetic field in the flow of a conducting liquid. As a matter of fact, flows past magnetic obstacles present an even richer dynamic behaviour than hydrodynamic flows past bluff bodies and deserve attention for their own sake. But apart from the fundamental interest, these flows are relevant due to a quite recent technological application, namely, the *Lorentz force velocimeter*^[35–38]. This is a device which allows the contactless measurement of flow rates in electrically conducting fluids, mainly liquid metals. In this system the conducting fluid flows in the presence of a localized field generated by a magnet and by measuring the force on the magnet system created by the flow it is possible to determine the flow rate.

The present work is part of an effort of the CIE-UNAM to develop an infrastructure to perform experimental studies of MHD flows with suitable measuring

techniques. Although some experimental studies of electromagnetically driven vortices in shallow layers of electrolytes have been previously accomplished at this research Center^[39,40], liquid metal MHD flows had not been experimentally explored so far. This work gathers three problems that in some way reflect the development of experimental capabilities at the CIE-UNAM during the time in which this thesis project was carried out. In this process, the collaborative work with the Ilmenau University of Technology, Germany, was fundamental.

Apart from the present introductory chapter, the thesis contains four additional chapters. In Chapter 2, flows in MHD pumps are explored theoretically and experimentally. First, the theoretical analysis of the fluid/wall slippage condition in MHD micropumps is presented. Commonly used flow models to describe MHD micropumps are revisited. Different combinations of slip and no slip conditions at the walls of the micropump are investigated, and the influence of the slip length on the flow rate is analysed. In addition, the experimental characterization of an electrolytic flow in a MHD pump at millimetric scale is presented. The flow is recirculated in an open channel and flow patterns were studied through Particle Image Velocimetry (PIV).

In Chapter 3, experimental results of liquid metal flows past localized magnetic fields, also known as magnetic obstacles, are presented in two configurations. In the first one, a pump driven flow in a duct of constant rectangular cross-section passes through the gap of two permanent rectangular magnets smaller than the duct's width. Secondly, a rectangular magnet is dragged upon the free surface of a quiescent liquid metal layer. Different flow regimes are analysed by varying the Reynolds number, paying particular attention to vortical flow patterns. In addition, results of the pump driven liquid metal MHD flow in a closed loop called Electromagnetic Flow Control Channel (EFCO) are presented. Parabolic hydrodynamic velocity profiles as well as M-shape profiles characteristic of MHD flows in fringing magnetic fields are studied. From the experimental data, the mass flow rate is computed. Experimental measurements were obtained through Ultrasound Doppler Velocimetry (UDV). All the experiments reported in this chapter were performed at the facilities of the Ilmenau University of Technology, Germany.

In chapter 4, the electromagnetic stirring produced by localized rotating magnetic fields in a shallow liquid metal layer (GaInSn) is studied experimentally. The magnetic field is produced by an array of small rotating permanent magnets located at the bottom of a cylindrical plexiglas container. The fluid layer is 13 mm thick and the maximum analysed rotation frequency is 7 Hz. The explored magnet arrays vary from one single magnet up to 5 magnets eccentrically located. The radial velocity component was recorded using Ultrasound Doppler Velocimetry (UDV) and analysed through the Fast Fourier Transform. The flow is also characterized by visualizing the free surface oscillations. It was found that the flow pattern organizes itself in a rotating ring where vorticity is concentrated and that pulsates with different characteristic frequencies. A three dimensional flow structure which is consistent with the observed features is proposed. Finally, in Chapter 5 the main conclusions of this thesis are offered.

Chapter 2

Flow in magnetohydrodynamic pumps[§]

In this chapter, flows in MHD pumps are explored theoretically and experimentally. First, the attention is focused on the theoretical analysis of the fluid/wall slippage condition in MHD micropumps. One- and two-dimensional flow models commonly used to describe MHD micropumps are revisited by assuming the slip condition in low-Hartmann number flows. Different combinations of slip and no slip conditions at the walls of the micropump are investigated, and the influence of the slip length on the flow rate is analysed. In addition, the experimental characterization of an electrolytic flow in a MHD pump at millimetric scale is presented. The flow is recirculated in an open channel and flow patterns are studied through Particle Image Velocimetry (PIV) in the electrode region (pumping zone) as well as in a zone separated from the pumping area (hydrodynamic zone) where MHD effects can be neglected.

2.1 Theoretical analysis of the slip condition in MHD micropumps

Many microfluidic devices, known as micro Total Analysis Systems (μ TAS), for chemical, medical, and biological applications rely on suitable pumping systems able to transport substances within different parts of the device. With this aim, several options have been proposed in the literature, including mechanical and nonmechanical micropumps whose characteristics have been analyzed in specialized reviews^[15,22–25]. Among different possibilities, magnetohydrodynamic (MHD) micropumps have attracted the attention of many researchers due to certain advantages such as simple fabrication process, the absence of moving parts, low voltage operation, and the possibility to achieve relatively high flow rates, being able to

[§]Part of this chapter was published in: M. Rivero, S. Cuevas, *Analysis of the slip condition in magnetohydrodynamic (MHD) micropumps*, Sensors and Actuators B: Chemical, 166-167, May 2012, Pages 884-892

produce forward and reverse flows^[26–28,41–46]. MHD micropumps are nonmechanical devices that use an electromagnetic body force (the Lorentz force) as the driving source in the flow. In fact, it has been recognized that Lorentz forces can be used for the control and manipulation of fluid flows in microdevices^[17,47].

The principle of operation of MHD pumps is well known and has been used for decades in macroscopic devices employed in many technological applications, mainly in the nuclear and metallurgical industries. A typical MHD conduction pump consists of a duct of constant rectangular cross-section, filled with an electrically conducting liquid, immersed in a uniform applied magnetic field. The walls transverse to the field are electrically insulated while those parallel to the field are electrically conducting (electrodes). When an electric potential difference is applied between the electrodes, an electric current circulates through the fluid perpendicularly to the magnetic field so that a driving Lorentz force is produced in the axial direction of the duct, transversally to both the current and the applied field. Although Lorentz force is proportional to the electrical conductivity of the fluid, it has been demonstrated that MHD pumps are effective even for weakly conductive liquids, such as many solutions used in microfluidic applications (for instance, PBS (phosphate buffered saline) solution^[48]). In fact, feasibility of MHD micropumps has been demonstrated by using both alternating and direct current with varying success^[28,43]. But applications do not restrict to electrolytic fluids. Liquid metal cooling devices driven by MHD pumps have been recently proposed as a heat dissipation mechanism in high performance CPUs^[49,50].

Several theoretical models have been reported in the literature to predict the behavior of MHD micropumps^[41,51–54]. The basic approach considers the flow in the micropump as laminar, incompressible and fully developed, which are suitable assumptions for low-Reynolds number flows. In principle, the motion of a conducting liquid in a magnetic field induces currents that circulate in the fluid and interact with the applied field, generating forces that oppose to the main flow. This phenomenon, known as the Hartmann breaking, is important in MHD duct flows when a relevant dimensionless parameter, namely the Hartmann number, is large^[55]. The Hartmann number is defined as $Ha = B_o \ell \sqrt{\sigma / \rho \nu}$, where B_o is the characteristic magnetic field strength, ℓ the characteristic length of the flow, and σ , ρ and ν are the electrical conductivity, mass density, and kinematic viscosity of the fluid, respectively. The square of the Hartmann number can be interpreted as the ratio of electromagnetic and viscous forces. In fact, the Hartmann breaking is responsible of the flattening of the velocity profile in MHD duct flows. In macroscopic liquid metal flows the Hartmann number can take very large values, however, in microfluidic applications Ha is usually very small ($Ha \lesssim 1$), particularly when dealing with low conductivity electrolytic solutions. Therefore, in low-Hartmann-number flows typical of MHD micropumps, Hartmann breaking is usually negligible and, consequently, velocity profiles tend to be parabolic^[17]. Nevertheless, it has been noted that some disagreements of numerical simulations with experimental data could be attributed to neglecting induced effects^[17]. MHD flows in micropumps can be described by one-dimensional (1D) models based on the classical Hartmann

flow^[55], that only consider the walls perpendicular to the magnetic field, usually known as the Hartmann walls. However, neglecting frictional effects of the walls parallel to the magnetic field, usually known as the side walls, may lead to misleading predictions^[51,56]. A better description can be achieved with two-dimensional (2D) models that take into account the four walls of the rectangular MHD micro duct^[44,51,52,54]. An interesting attempt to model MHD micropumps within a more general framework has been recently proposed^[56].

So far, it appears that all attempts to model flows in MHD micropumps have been based on the assumption that the no slip condition for the fluid velocity holds in all walls of the duct. This condition implies a perfect wettability at the liquid-wall interface so that, if the wall is at rest, the fluid velocity at the wall vanishes. Although the no slip condition successfully represents a wide range of fluid flow problems, it has been observed that it is not valid for all situations. In particular, the slip condition, in which the fluid velocity at the stationary solid wall does not vanish, is common in many microfluidic and nanofluidic applications^[15,25].

Fluid slippage is usually characterized by the slip (or Navier) length, L_s , defined as the distance at which velocity would be zero if extrapolated linearly towards the wall. The velocity difference between the boundary surface and the adjacent fluid particles is known as the slip velocity, V_s , and in the case of a unidirectional flow, is related to the tangential stress at the solid boundary in the form

$$V_s = L_s \frac{\partial V}{\partial n}, \quad (2.1)$$

where n is the coordinate normal to the wall. If $L_s = 0$, condition (2.1) reduces to the no slip condition, while perfect slip condition, for which there is no influence of the boundary surface on the velocity profile, is obtained when $L_s \rightarrow \infty$. Experiments have shown that the slip length can take values that go from nanometers to microns^[57,58]

Different physical explanations have been proposed in the literature to account for the origin of slippage in liquids. *Molecular slippage*, *viscous*, and *no-shear/no-slip* models are theoretical attempts to explain liquid slip in different conditions^[15,59]. Another interesting explanation is that the slip phenomenon may result from the spontaneous formation of a gaseous underlayer that lubricates the flow^[15,57,60]. This layer of bubbles, formed at the interface between the solid surface and the liquid, is stretched into the form of a film by the action of the flow. The origin of this film may be related to external dissolved gases up to metastable concentration. Incidentally, it is well-known that in MHD micropumps, bubbles are created by electrolysis at the electrode walls^[26,45] but in this case they do not necessarily form a thin film. In fact, bubbles usually affect the performance of the micropump and special designs have been proposed to minimize their interference^[27,28]. Another important mechanism that may lead to slippage occurs in electrokinetic phenomena, basically in electro-osmotic flows (EOF)^[25,61–63]. When a solid is brought into contact with a polar liquid, its surface acquires an electric charge. In order to neutralize this charge, counter-ions of the solution migrate to-

wards the surface forming the electric double layer (EDL), composed by the Stern layer and the Gouy-Chapman or diffusion layer. In the Stern layer counter-ions are strongly attached to the surface and its thickness is of the order of some nanometers. Beyond this layer, the diffusion layer is constituted of counter-ions attracted to the wall. This attraction is not strong enough to maintain both layers together, so the diffusion layer may slip over the fluid attached to the surface (Stern layer). The plane that divides this two layers is named *slipping plane*. If an electric field parallel to the EDL is applied, a force is exerted in the ions of the diffuse layer which in turn will drag the liquid. The motion in the layer is transported to the rest of the fluid by the viscosity, resulting the EOF.

Recently, the existence of slip in MHD duct flows at rather high Hartmann numbers has been considered in different classic flows such as the Hartmann flow, fully developed flow in a rectangular duct, and a quasi-2D-turbulent flow^[64]. The main interest of the study is to analyze the consequences that slip conditions may have in MHD fusion related liquid metal flows, as those in fusion blankets. Since the Hartmann number is not small in these flows, induced effects are not negligible and, in addition to velocity profiles, the induced magnetic field is also determined. Very interesting consequences were extracted from this work, particularly, that the thickness of the Hartmann layers (attached to the walls perpendicular to the magnetic field) scales in the same form as in the absence of slip, while the thickness of the side layers (attached to walls parallel to the magnetic field) is affected by slippage.

Although conditions for the appearance of slippage in MHD micropumps have not been fully investigated, it is interesting to explore the effects that the slip condition may have in the performance of these devices. If the fluid slips, the charge losses will be reduced for a given flow rate with respect to the no slip case, affecting evidently the efficiency of the MHD micropump. In the present study, one- and two-dimensional models previously addressed in the literature for describing the flow in an MHD micropump, are revisited analytically and numerically considering mixed slip and no slip boundary conditions. Also, a comparison with available experimental data was carried out. The objective is to explore the consequences of the existence of slip for low-Hartmann-number flows in MHD micropumps and determine how slippage affects different approximations used in the modeling of such devices.

2.1.1 A simple hydraulic resistance model

The simplest model to estimate the flow rate in microchannels is by means of Poiseuille's Law^[57],

$$\Delta p = QR_h, \quad (2.2)$$

where Δp is the pressure difference along the channel, Q is the volumetric flow rate, and R_h is the hydraulic resistance of the channel. This law can be established from the fully developed solution of the flow through a narrow channel and has been used for the estimation of the flow rate in MHD micropumps^[27,41,43]. Let

us consider a fully developed flow of an electrically conducting fluid in a duct of constant rectangular cross-section of height b and width a under a transverse uniform magnetic field of strength B_0 , where the origin of coordinates is placed at the lower left corner, as shown in Figure 2.1.

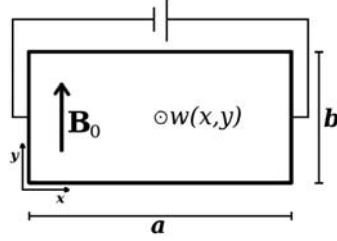


Fig. 2.1. Duct's cross-section of the analyzed MHD micropump.

The aspect ratio of the duct is assumed to be small ($b/a \ll 1$) and the lateral walls (parallel to the magnetic field) are electrodes connected to a power source. In this way, an electric current flows through the fluid perpendicularly to the applied field. The interaction of the current and the magnetic field creates a Lorentz force in the axial z -direction that is able to push the fluid. If we assume that the pressure gradient produced by the Lorentz force along the channel is constant and that slip conditions exist at the walls perpendicular to the magnetic field, the governing equation and boundary conditions are

$$\frac{d^2 w}{dy^2} = \frac{1}{\mu} \frac{\partial p}{\partial z}, \quad (2.3)$$

$$\begin{aligned} w(b) + L_s \frac{dw(b)}{dy} &= 0, \\ w(0) - L_s \frac{dw(0)}{dy} &= 0, \end{aligned} \quad (2.4)$$

where w is the velocity component in the axial z -direction and $\mu = \rho\nu$ is the dynamic viscosity of the fluid. The velocity profile that satisfies equations (2.3) and (2.4) takes the form

$$w(y) = \frac{\Delta p}{L} \frac{b}{2\mu} \left[y \left(1 - \frac{y}{b} \right) + L_s \right], \quad (2.5)$$

where the pressure gradient has been expressed as $-\partial p/\partial z = \Delta p/L$, Δp being the pressure drop along a length L of the channel in the direction of flow. Since Δp is only produced by the Lorentz force acting on the fluid, we can approximate it as

$$\Delta p = \frac{IB_0}{b}, \quad (2.6)$$

where I is the total electric current across the channel (in the x -direction) and b is the height of the electrode (see Figure 2.1). By integration of the velocity profile (2.5) in the cross-section of the duct, we get the volumetric flow rate:

$$Q = \frac{ab^3 \Delta p}{12\mu} \left(1 + \frac{6L_s}{b} \right). \quad (2.7)$$

Comparing equations (2.7) and (2.2), the hydraulic resistance is found to be

$$R_{hs} = \frac{12\mu L}{ab^3 \left(1 + \frac{6L_s}{b} \right)}, \quad (2.8)$$

where the subindex $_s$ has been added to denote the resistance with slip. Clearly, the effect of the slippage is to reduce the hydraulic resistance and, consequently, to increase the flow rate for a given pressure drop. Note that when the slip length is negligible ($L_s \ll b$), the velocity, flow rate, and hydraulic resistance become the solutions of the classical Poiseuille flow with no slip condition. If Eq. (2.6) is substituted into Eq. (2.7), an expression for the flow rate is obtained in terms of the electric current and the applied magnetic field:

$$Q_s = \frac{ab^2 I B_0}{12\mu} \left(1 + \frac{6L_s}{b} \right). \quad (2.9)$$

Although simple hydraulic resistance models are useful in practical applications, a more complete flow analysis is necessary to improve the accuracy of the flow rate estimation. In the following sections, we use analytical and numerical solutions to analyze the effect of the slip condition on the flow in a rectangular MHD micropump.

2.1.2 Formulation of the problem

Let us now address the flow problem in a more complete form. In general, the electric current density, \mathbf{j} , that circulates through the fluid is given by Ohm's law, that is,

$$\mathbf{j} = \sigma (-\nabla\phi + \mathbf{u} \times \mathbf{B}_0), \quad (2.10)$$

where ϕ is the electric potential established through the electrodes and \mathbf{u} is the velocity field. If we use Ohm's law (2.10) to express the electric current density in the case of a fully developed flow in the MHD micropump shown in Figure 2.1, the equation of motion takes the form

$$\mu \left(\frac{\partial^2 w}{\partial x^2} + \frac{\partial^2 w}{\partial y^2} \right) - \sigma B_0^2 w = \frac{\partial p}{\partial z} - \sigma B_0 \frac{\partial \phi}{\partial x}, \quad (2.11)$$

where, for the sake of generality, we have considered that in addition to the driving Lorentz force, a constant pressure gradient in the z -direction may also be present, for instance, due to hydrostatic pressure. Therefore, depending on the direction in which the electric current is applied, the resulting Lorentz force may act in

favour or against the additional pressure gradient. In principle, the solution of the MHD flow problem requires to determine not only the flow velocity but also the magnetic field induced by the fluid motion. However, in MHD micropumps induced magnetic fields, created from induced electric currents, are extremely weak and can be completely disregarded. The equation of motion will be solved using mixed slip and no slip boundary conditions. The effect of slip on both fluid velocity and induced magnetic field in macroscopic liquid metal MHD flows is presented in^[64].

In dimensionless form Eq. (2.11) reads

$$\epsilon^2 \frac{\partial^2 w}{\partial x^2} + \frac{\partial^2 w}{\partial y^2} - \text{Ha}^2 w = G - \beta, \quad (2.12)$$

where the velocity, w , and coordinates x and y (denoted with the same symbols as their dimensional counterparts), are normalized by ν/b , a , and b , respectively. In addition, coordinate z is normalized by the electrode length, L , while the magnetic field, the additional pressure drop and the electric potential are scaled by the characteristic values B_0 , Δp , and ϕ_c , respectively. In Eq. (2.12), four dimensionless parameters appear. First, ϵ is the aspect ratio of the rectangular cross-section, $\epsilon = b/a$, while Ha is the previously defined Hartmann number based on the separation between the walls perpendicular to the magnetic field, b , that is, $\text{Ha} = B_0 b \sqrt{\sigma/\rho\nu}$. The parameter $G = b^3 \Delta p / (\rho\nu^2 L)$ is the ratio of any additional pressure drop (hydrostatic or produced by another pump) and the viscous pressure drop. Finally, the parameter $\beta = b^3 J_0 B_0 / (\rho\nu^2)$, where $J_0 = \sigma \phi_c / a$ is the electric current density applied externally, is the ratio of the pressure drop due to the Lorentz force and the viscous pressure drop. The third term on the left-hand side of Eq. (2.12) is responsible for the Hartmann braking and can be neglected when the liquid is a poor conductor of electricity ($\text{Ha} \ll 1$). In contrast, when liquid metals are used in microchannels (see for instance^[44] and^[49]), the Hartmann number may be of order 10 and the Hartmann braking term cannot be neglected.

Table 2.1 shows the values of dimensionless parameters computed using data reported in the literature. Most of the experiments were carried out in horizontal channels, so the additional pressure difference Δp is zero ($G = 0$). In the majority of cases, ducts with rectangular cross-section were considered, with an aspect ratio close to 0.5. In addition, electrolytes were the most used working fluids, leading to very low values of the Hartmann number. The wide range of values for β (approximately between 1 and 15500) indicates the extensive combination of diverse experimental conditions involving applied voltages in the range of 1 – 60V, magnetic fields from 40 mT to 0.4 T, and characteristics lengths that vary from some μm to mm. The exception is the work by Zhong *et al.*^[44] where experiments considered not only water and saline solution, but also a liquid metal (mercury) was used; therefore, Ha and β values exceed by orders of magnitude the other cases. We now turn to solve Eq. 2.12 with different approximations and slip and no slip boundary conditions.

Author	ϵ	Ha	β
Jang & Lee ^[41]	0.40	0.010	5830.62
Bau <i>et al.</i> ^[47]	1.55	0.035	9705.41
Zhong ^R <i>et al.</i> ^[44]	0.58	0.0004	0.52
Zhong ^T <i>et al.</i> ^[44]	0.50	0.0004	1.10
Zhong ^T <i>et al.</i> ^[44]	0.32	8.854	4.22×10^8
Homsy <i>et al.</i> ^[27]	0.50	0.0045	1452.94
Nguyen & Kassegne ^[28]	1.00	0.0006	88.56
Ho ^[52]	1.00	0.0066	11070
Lemoff & Lee ^[43]	0.48	0.0003	13.80
Kabbani <i>et al.</i> ^[53]	2.03	0.0007	4.68
Huang <i>et al.</i> ^[42]	1.60	0.0713	15482.9

Table 2.1. Table of dimensionless parameters computed with data reported in the literature.

2.1.3 Hartmann flow between infinite plates with slip

The simplest case of study corresponds to ducts with small aspect ratio, $\epsilon \ll 1$. Under this approximation, the first term on the left-hand side of Eq. (2.12) can be neglected and the velocity becomes independent of the x -coordinate, so that the effect of the side walls is disregarded. The equation of motion becomes

$$\frac{d^2 w}{dy^2} - \text{Ha}^2 w = G - \beta. \quad (2.13)$$

In dimensionless terms, the slip boundary conditions at the walls transverse to the magnetic field read

$$\begin{aligned} w(1) + \alpha \frac{dw(1)}{dy} &= 0, \\ w(0) - \alpha \frac{dw(0)}{dy} &= 0, \end{aligned} \quad (2.14)$$

where $\alpha = L_s/b$ is the dimensionless slip length. Equation (2.13) with boundary conditions (2.14) corresponds to the Hartmann flow configuration with slip at both walls and the solution is

$$w(y) = \frac{G - \beta}{\text{Ha}^2} \left(-1 + \frac{\cosh\left(\frac{\text{Ha}}{2}(1 - 2y)\right)}{\cosh\left(\frac{\text{Ha}}{2}\right) + \alpha \text{Ha} \sinh\left(\frac{\text{Ha}}{2}\right)} \right). \quad (2.15)$$

When $\alpha = 0$, the velocity profile (2.15) becomes the classical Hartmann solution. If we integrate the profile (2.15) in the duct cross-section, we get the flow rate in the form

$$Q = \frac{G - \beta}{\text{Ha}^2} \left(-1 + \frac{2}{\alpha \text{Ha}^2 + \text{Ha} \coth\left(\frac{\text{Ha}}{2}\right)} \right). \quad (2.16)$$

First note that as the Hartmann number increases, independently of the value of α , the flow rate tends to zero since the braking force overcomes the applied force. In turn, in the limit of perfect slip ($\alpha \rightarrow \infty$) the flow rate tends to $-(G - \beta)Ha^{-2}$. Provided that G and/or β are not zero, the flow rate is not bounded as the Hartmann number decreases. In the hydrodynamic limit when both $\beta \rightarrow 0$ and $Ha \rightarrow 0$, Eqs. (2.15) and (2.16) reduce to

$$w(y) = \frac{G}{2} (y^2 - y - \alpha), \quad (2.17)$$

$$Q = -\frac{G}{12}(1 + 6\alpha), \quad (2.18)$$

which are the Poiseuille-like solutions with slippage.

2.1.4 Flow in a rectangular duct with slip at the Hartmann walls

If we now relax the condition $\epsilon \ll 1$ and consider side-wall effects, the problem becomes 2D. Under this assumption, it is possible to find an analytical solution to Eq. (2.12) if the slip conditions are applied only to a pair of walls, either the Hartmann or the side walls^[64]. In the present section, the flow with slip at the Hartmann walls and no slip at the side walls is analyzed, while the solution to the flow with slip at the side walls and no slip at the Hartmann walls is found in Sec. 2.1.5. Finally, in Sec. 2.1.6 numerical results are shown in the case where slip condition exist in all walls and a comparison among these configurations is made.

The corresponding boundary conditions with no slip at the side walls and slip at the Hartmann walls are expressed in the form

$$\begin{aligned} w(0, y) &= w(1, y) = 0, \\ w(x, 0) - \alpha \frac{\partial w(x, 0)}{\partial y} &= w(x, 1) + \alpha \frac{\partial w(x, 1)}{\partial y} = 0. \end{aligned} \quad (2.19)$$

The analytical solution of Eq. (2.12) with boundary conditions (2.19) is obtained by Fourier expansion along the direction in which the no slip condition exist. The solution is found to be

$$\begin{aligned} w(x, y) = -\frac{4(G - \beta)}{\pi} \sum_{n=\text{odd}}^{\infty} \left[\frac{\sin(n\pi x)}{n\lambda_n^2} \times \right. \\ \left. \frac{\cosh\left(\frac{\lambda_n}{2}\right) - \cosh\left(\frac{(2y-1)\lambda_n}{2}\right) + \alpha\lambda_n \sinh\left(\frac{\lambda_n}{2}\right)}{\cosh\left(\frac{\lambda_n}{2}\right) + \alpha\lambda_n \sinh\left(\frac{\lambda_n}{2}\right)} \right], \end{aligned} \quad (2.20)$$

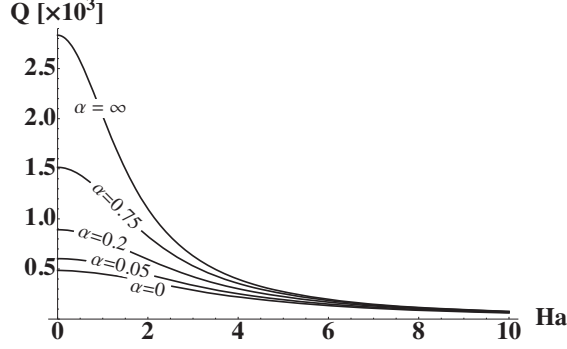


Fig. 2.2. Dimensionless flow rate as a function of the Hartmann number for different slip lengths in an MHD micropump with slip at the Hartmann walls and no slip at the side walls. $\epsilon = 0.5$, $G = 0$ and $\beta = 8500$.

where λ_n is defined as

$$\lambda_n^2 = \epsilon^2 n^2 \pi^2 + \text{Ha}^2. \quad (2.21)$$

For the low Hartmann numbers found in MHD micropump applications, the velocity profile (2.20) presents a parabolic shape. By integration, the flow rate is found in the form

$$Q = -\frac{8(G - \beta)}{\pi^2} \sum_{n=\text{odd}}^{\infty} \frac{\lambda_n - (2 - \alpha\lambda_n^2) \tanh\left(\frac{\lambda_n}{2}\right)}{n^2 \lambda_n^3 (1 + \alpha\lambda_n \tanh\left(\frac{\lambda_n}{2}\right))}. \quad (2.22)$$

In Figure 2.2, the flow rate as a function of the Hartmann number for different slip lengths is shown. We choose the typical values $\epsilon = 0.5$ and $G = 0$; in addition, we take $\beta = 8500$ which is within the range of values reported in the literature (see table 2.1). Similarly to the Hartmann flow case (Sec. 2.1.3), the flow rate decreases as Ha grows since electromagnetic induced effects increase and the resulting braking force can overcome the applied one. However, in contrast to the 1D case, in the limit $\alpha \rightarrow \infty$ the flow rate is bounded even when the Hartmann number tends to zero (for $\beta \neq 0$). This behavior reflects the fact that the velocity field must satisfy no slip conditions at the side walls. Explicitly, we find that in the limit $\alpha \rightarrow \infty$, Eq. (2.22) becomes

$$\lim_{\alpha \rightarrow \infty} Q = -\frac{8(G - \beta)}{\pi^2} \sum_{n=\text{odd}}^{\infty} \frac{1}{n^2 (\epsilon^2 n^2 \pi^2 + \text{Ha}^2)}. \quad (2.23)$$

In order to assess the effect of the slip condition on the flow rate, the percentage of increase in the flow rate produced by applying conditions (2.19) compared with the case where no slip condition is applied in all walls, is shown in Figures 2.3a and 2.3b as a function of the Hartmann number and the dimensionless slip length, respectively. Notice that for $\text{Ha} < 1$, which incidentally is usually the condition of operation of MHD micropumps, the flow rate increases up to 24% for a slip length of one twentieth of the characteristic length and around 5% with one hundredth of

this length. In this low Hartmann number range (see shaded area in Figure 2.3b), the increase of the flow rate as a function of the slip length is approximately linear.

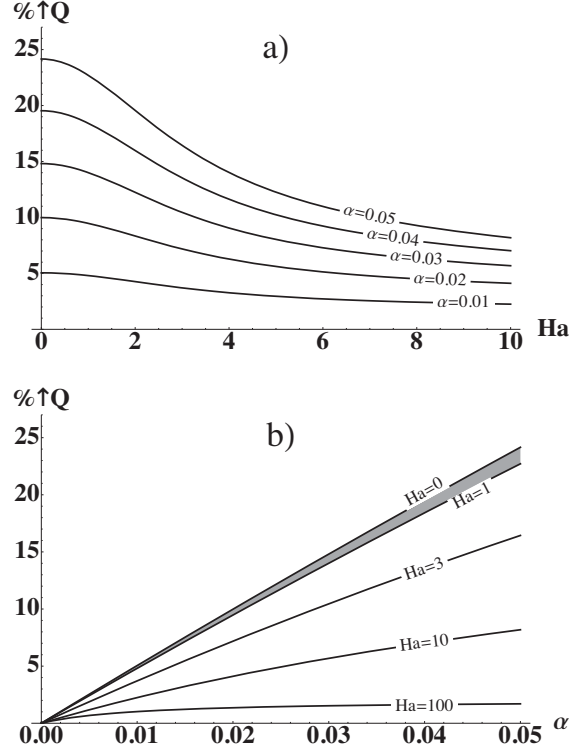


Fig. 2.3. Percentage of flow rate increase produced by applying the slip condition at the Hartmann walls compared with the case where no slip conditions exist in all walls, a) as a function of the Hartmann number and, b) as a function of the slip length. Shaded area represents the range of low Ha values common in MHD micropump applications. $\epsilon = 0.5$, $G = 0$ and $\beta = 8500$.

Let us now consider the effect of geometry in the flow rate with and without the slip condition at the Hartmann walls. In Figure 2.4 the flow rate as a function of the Hartmann number is shown for three different aspect ratios in the two limiting cases, $\alpha = 0$ and $\alpha \rightarrow \infty$ (indicated as subscripts in the aspect ratio). When no slip conditions exist in all walls ($\alpha = 0$), given the scale of the figure, no significant change in the flow rate can be observed when the aspect ratio is varied (this case is shown in a proper scale in Figure 2.7 in Sec. 2.1.5). In contrast, in the limit $\alpha \rightarrow \infty$ the flow rate is largely influenced by the aspect ratio, observing an increase as the aspect ratio decreases, that is, as the Hartmann walls become wider. Therefore, the higher the slippage surface the higher the flow rate. Note that the maximum flow rate value for $\epsilon = 1/4$, is one order of magnitude larger than no slip cases.

Finally, in the hydrodynamic limit ($\beta \rightarrow 0$ and $Ha \rightarrow 0$) the Poiseuille-like form of velocity profile and flow rate expressions are recovered:

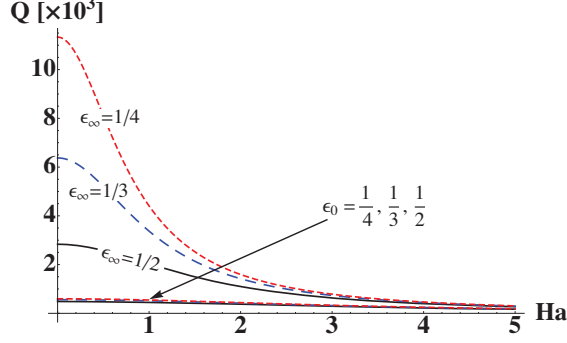


Fig. 2.4. Dimensionless flow rate as a function of the Hartmann number for three aspect ratios ($\epsilon = 1/2$ (solid black), $1/3$ (long dashed blue), and $1/4$ (short dashed red)) in the limit cases $\alpha = 0$ and $\alpha = \infty$. Subindexes $_0$ and $_\infty$ in ϵ denote the corresponding limit cases for α . $G = 0$ and $\beta = 8500$.

$$w(x, y) = \frac{4G}{\pi^3 \epsilon^2} \sum_{n=\text{odd}}^{\infty} \left[\frac{\sin(n\pi x)}{n^3} \times \left(1 - \frac{\cosh\left(\frac{2y-1}{2}n\pi\epsilon\right)}{\cosh\left(\frac{n\pi\epsilon}{2}\right) + n\pi\alpha\epsilon \sinh\left(\frac{n\pi\epsilon}{2}\right)} \right) \right], \quad (2.24)$$

$$Q = -\frac{8G}{\pi^5 \epsilon^3} \sum_{n=\text{odd}}^{\infty} \frac{1}{n^5} \left(n\pi\epsilon - \frac{2}{n\pi\alpha\epsilon + \coth\left(\frac{n\pi\epsilon}{2}\right)} \right). \quad (2.25)$$

2.1.5 Flow in a rectangular duct with slip at the side walls

Let us now consider the flow in a rectangular duct with no slip condition at the Hartmann walls and slip condition at the side walls. Incidentally, this flow corresponds to the case where the slip condition occurs at the electrodes of the MHD micropump where electrolysis and the formation of bubbles take place. The boundary conditions are expressed in the following form:

$$\begin{aligned} w(0, y) - \alpha \frac{\partial w(0, y)}{\partial x} &= w(1, y) + \alpha \frac{\partial w(1, y)}{\partial x} = 0, \\ w(x, 0) &= w(x, 1) = 0. \end{aligned} \quad (2.26)$$

As in the Sec. 2.1.4, we look for a Fourier series solution of Eq. (2.12) with conditions (2.26). The solution for the velocity profile takes the form

$$w(x, y) = -\frac{4(G - \beta)}{\pi \epsilon^2} \sum_{n=\text{odd}}^{\infty} \left[\frac{\sin(n\pi y)}{n\lambda_n^2} \times \frac{\cosh\left(\frac{\lambda_n}{2}\right) - \cosh\left(\frac{(2x-1)\lambda_n}{2}\right) + \alpha\lambda_n \sinh\left(\frac{\lambda_n}{2}\right)}{\cosh\left(\frac{\lambda_n}{2}\right) + \alpha\lambda_n \sinh\left(\frac{\lambda_n}{2}\right)} \right], \quad (2.27)$$

where λ_n is now defined as

$$\lambda_n^2 = \frac{\text{Ha}^2 + n^2\pi^2}{\epsilon^2}. \quad (2.28)$$

Once integrated in the cross-section, the flow rate becomes

$$Q = -\frac{8(G - \beta)}{\pi^2\epsilon^2} \sum_{n=\text{odd}}^{\infty} \frac{\lambda_n - (2 - \alpha\lambda_n^2) \tanh\left(\frac{\lambda_n}{2}\right)}{n^2\lambda_n^3 (1 + \alpha\lambda_n \tanh\left(\frac{\lambda_n}{2}\right))}. \quad (2.29)$$

Figure 2.5 shows the flow rate as a function of the Hartmann number for different slip lengths and for the same values of the parameters ϵ , G , and β used in Figure 2.2. As occurs in the previous case, in the limit of perfect slip ($\alpha \rightarrow \infty$) the flow is bounded even when $\text{Ha} \rightarrow 0$, for $\beta \neq 0$. Comparing with the results shown in Figure 2.2, the maximum flow rate for perfect slip at the side walls drops approximately 75% with respect to the case of perfect slip at the Hartmann walls.

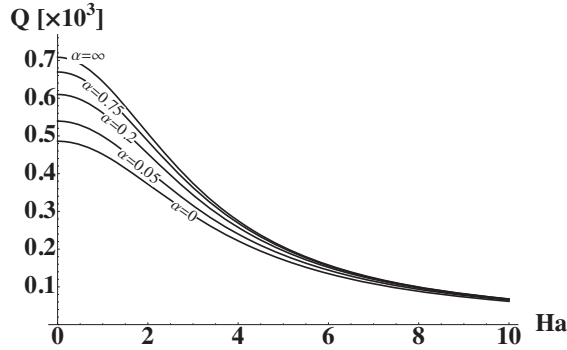


Fig. 2.5. Dimensionless flow rate as a function of the Hartmann number for different slip lengths in an MHD micropump with slip at the side walls and no slip at the Hartmann walls. $\epsilon = 0.5$, $G = 0$ and $\beta = 8500$.

Incidentally, by taking the limit $\alpha \rightarrow \infty$ in Eq. (2.29), we get

$$\lim_{\alpha \rightarrow \infty} Q = -\frac{8(G - \beta)}{\pi^2} \sum_{n=\text{odd}}^{\infty} \frac{1}{n^2 (n^2\pi^2 - \text{Ha}^2)}. \quad (2.30)$$

which coincides with the 1D solution (2.16) when no slippage exists at the Hartmann walls.

The percentage of increase in the flow rate produced by applying slip conditions at the side walls compared with the case where no slip condition is applied at all walls, is shown in Figures 2.6a and 2.6b as functions of the Hartmann number and the dimensionless slip length, respectively. It is observed that for $\text{Ha} < 1$, increments of 11% are found for a slip length of one twentieth of the characteristic length and around 3% with one hundredth of this length. In Figure 2.6b, the flow rate shows an asymptotic increase as a function of the slip length for the low Hartmann number cases.

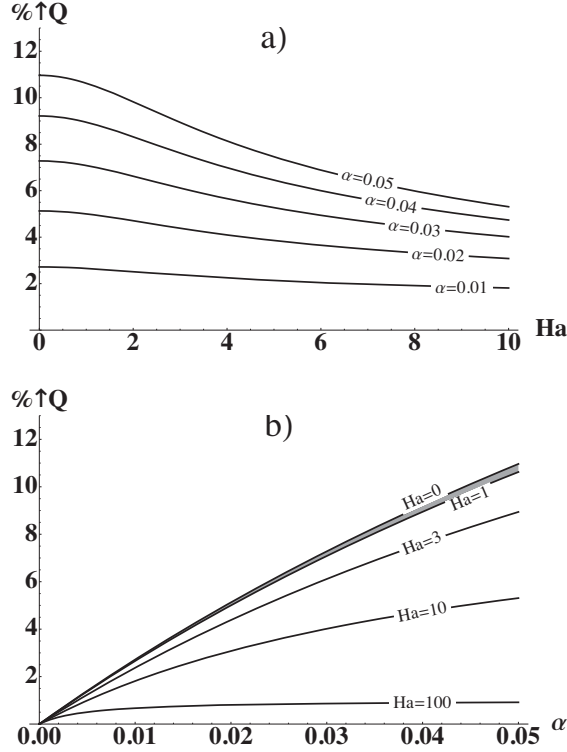


Fig. 2.6. Percentage of flow rate increase produced by applying the slip condition in side walls compared with the case where no slip conditions exist in all walls, a) as a function of Hartmann number and, b) as a function of slip length. Shaded area represents the MHD micropump application zone. $\epsilon = 0.5$, $G = 0$ and $\beta = 8500$.

In Figure 2.7 the flow rate as a function of the Hartmann number is shown for three different aspect ratios in the limiting cases of no slip ($\alpha = 0$) and perfect slip ($\alpha \rightarrow \infty$). Evidently, the no slip case coincides with the one shown in Figure 2.4 but in the present scale the effect of the aspect ratio in the flow rate is clearly observed. In contrast, the behavior of the flow rate in the limit of perfect slip is remarkably different from that found in the case of slip at the Hartmann walls. In fact, when $\alpha \rightarrow \infty$ at the side walls, the flow rate takes the same value for all aspect ratios. This is clearly observed in Eq. (2.30) since the flow rate becomes independent of the aspect ratio once the limit $\alpha \rightarrow \infty$ is taken.

In the hydrodynamic limit ($Ha \rightarrow 0$, $\beta \rightarrow 0$), the velocity and flow rate expressions recover the Poiseuille-like behavior, that is,

$$w(x, y) = -\frac{4G}{\pi^3} \sum_{n=odd}^{\infty} \left[\frac{\sin(n\pi y)}{n^3} \times \left(1 - \frac{\epsilon \cosh\left(\frac{n\pi(2x-1)}{2\epsilon}\right)}{\epsilon \cosh\left(\frac{n\pi}{2\epsilon}\right) + n\pi\alpha \sinh\left(\frac{n\pi}{2\epsilon}\right)} \right) \right], \quad (2.31)$$

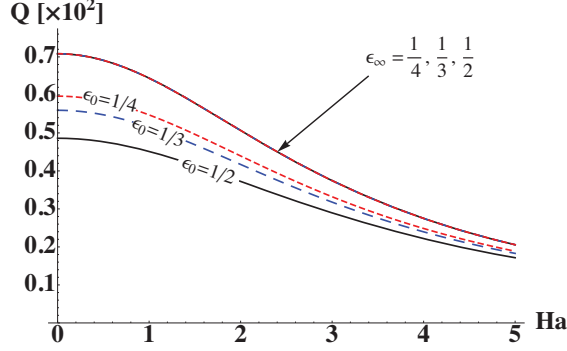


Fig. 2.7. Dimensionless flow rate as a function of Ha number for three aspect ratios ($\epsilon = 1/2$ (solid black), $1/3$ (long dashed blue), and $1/4$ (short dashed red)) in the limit cases $\alpha = 0$ and $\alpha = \infty$. Subindexes $_0$ and $_\infty$ in ϵ denote the corresponding limit cases for α . $G = 0$ and $\beta = 8500$.

and

$$Q = -\frac{8G}{\pi^5} \sum_{n=odd}^{\infty} \frac{1}{n^5} \left(n\pi - \frac{2\epsilon^2}{n\pi\alpha + \epsilon \coth\left(\frac{n\pi}{2\epsilon}\right)} \right). \quad (2.32)$$

2.1.6 Flow in a rectangular duct with slip at Hartmann and side walls

We now look for a solution of Eq. (2.12) with slip conditions at the four walls, namely,

$$\begin{aligned} w(0, y) - \alpha \frac{\partial w(0, y)}{\partial x} &= w(1, y) + \alpha \frac{\partial w(1, y)}{\partial x} = 0, \\ w(x, 0) - \alpha \frac{\partial w(x, 0)}{\partial y} &= w(x, 1) + \alpha \frac{\partial w(x, 1)}{\partial y} = 0. \end{aligned} \quad (2.33)$$

In fact, it is not possible to find an analytical solution of Eq. (2.12) for the velocity profile when slip conditions exist at all boundaries, even though the same slip length is used in all walls. In order to obtain a solution we use the Collocation-Tau-Chebyshev method^[65].

The percentage of increase in the flow rate produced by applying slip conditions at the Hartmann and the side walls compared with the case where no slip condition is applied at all walls, is shown in Figure 2.8 as a function of the Hartmann number. It can be observed that for $Ha < 1$, an increment of 39% is found for a slip length of one twentieth of the characteristic length and around 8% with one hundredth of this length. It should be noted that the percentage of the flow rate increase in this case is not always the addition of the corresponding increases of the cases with slip at the Hartmann walls (see Figure 2.3a) and that with slip at the side walls (see Figure 2.6a).

Figure 2.9 shows the flow rate as a function of Hartmann number for different aspect ratios ($\epsilon = 1, 1/2, 1/3$ and $1/4$) and a slip length in all walls corresponding

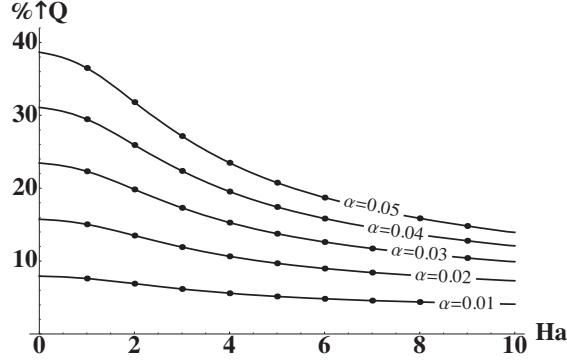


Fig. 2.8. Percentage of flow rate increase produced by applying slip conditions at both the Hartmann and side walls compared with the case where no slip conditions exist in all walls, as a function of the Hartmann number for different α values. $\epsilon = 0.5$, $G = 0$ and $\beta = 8500$.

to one hundredth the characteristic length. We notice that the flow rate has an asymptotic increase as ϵ get smaller. In fact, in the limit $\epsilon \rightarrow 0$, the flow rate approaches the 1D solution, Eq. (2.16). For $\alpha = 0.01$ and $Ha = 0$, in the limit $\epsilon \rightarrow 0$ the numerical solution leads to a maximum flow rate of $Q \sim 754$.

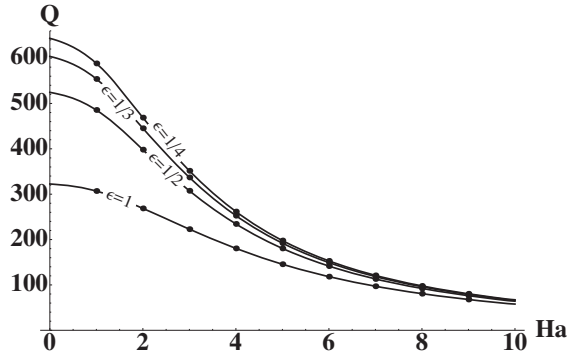


Fig. 2.9. Dimensionless flow rate as a function of Hartmann number with slip conditions at both the Hartmann and the side walls for different aspect ratios. $\alpha = 0.01$, $G = 0$ and $\beta = 8500$.

The percentage of increase in the flow rate produced with aspect ratios less than one compared with the case of a square duct ($\epsilon = 1$), is shown in Figure 2.10 as a function of the Hartmann number for $\alpha = 0.01$. Note that in the low Hartmann number range, for $\epsilon = 1/2$ the maximum increase is around 63% while for $\epsilon = 1/4$ the increase can reach 100%.

Finally, Figure 2.11 shows the flow rate for $Ha = 0.01$ as a function of the slip length for the three analyzed cases, namely, slip at the Hartmann walls, slip at the side walls, and slip at both the Hartmann and the side walls. For $\alpha = 0$, the dimensionless flow rate is $Q = 485.8$. It can be observed that in this low Hartmann number case, the flow rate increases linearly with α when slip exist in all walls.

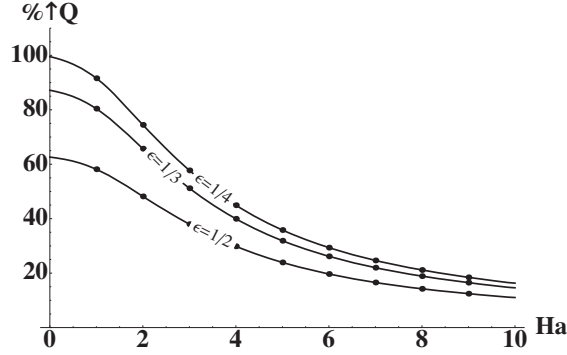


Fig. 2.10. Percentage of increase in the flow rate produced with aspect ratios less than one compared with the case $\epsilon = 1$, as a function of Ha number. $\alpha = 0.01$, $G = 0$ and $\beta = 8500$.

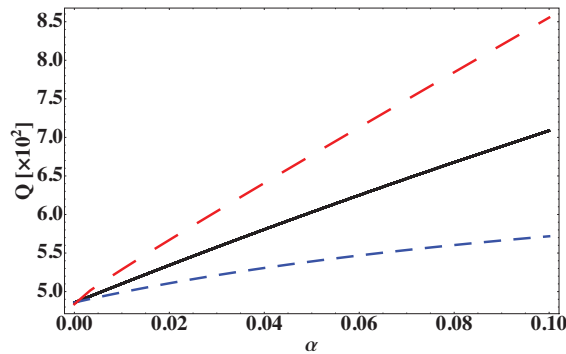


Fig. 2.11. Dimensionless flow rate as a function of the slip length for the three analyzed cases: slip at the side walls (short dashed blue line), slip at the Hartmann walls (solid black line), and slip at both the Hartmann and the side walls (long dashed red line). $Ha = 0.01$, $\epsilon = 0.5$, $G = 0$ and $\beta = 8500$.

2.1.7 Comparison of model results with experimental data

In order to validate the theoretical results of the models presented in the previous sections, a comparison of the model results against experimental data available in the literature is presented in this section. We compare the experimental data with theoretical results obtained without slip. Notice that the solutions presented in sections 2.1.4, 2.1.5, and 2.1.6 coincide when slip is absent.

Let us first consider the experimental results of Arumugan et al.^[46]. These authors analyzed a DC micropump with dimensions $L = 20$ mm, $a = 270$ μm , $b = 640$ μm , and a constant magnetic field intensity $B_0 = 0.41$ T. A RedOx solution of nitrobenzene (NB) at two concentrations C_o , 0.1 M and 0.25 M, in 0.1 M TBAPF₆ in acetonitrile was used. In Figure 2.12, the experimental mean velocities for both concentrations obtained by applying three different voltages (0.9, 1.1 and 1.3 V) are shown as a function of the electric current. Achieved electric current ranges from 0 to 6 mA. Use of redox species allows to work below or near

bubble formation water threshold (~ 1.23 V) and then electrolysis is avoided. In addition to the experimental data, the results obtained by Kabbani et al.^[53] with a closed form model are also shown and compared with the present 2D model. Different dynamic viscosity of both solutions lead to distinct model predictions slopes.

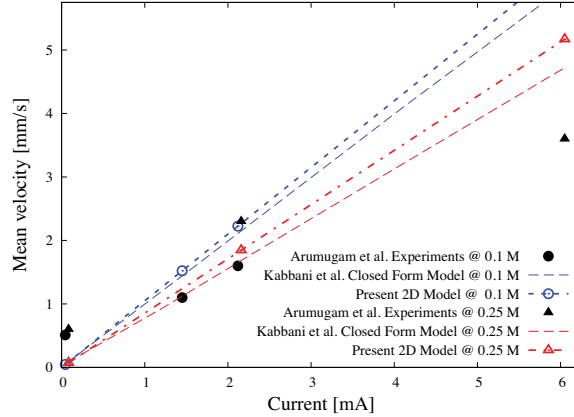


Fig. 2.12. Mean velocity as a function of the electric current for a DC micropump analyzed by Arumugam et al.^[46] with a RedOx nitrobenzene solution with concentrations of $C_o = 0.1$ M and $C_o = 0.25$ M.. Experimental data are compared against the present 2D model and results obtained by Kabbani et al.^[53] with a closed form model.

Jang & Lee^[41] analyzed a DC pump with microchannel dimensions $L = 40$ mm, $a = 1$ mm, $b = 0.4$ mm, an applied magnetic field of 0.44 T and sea water as conducting fluid. Figure 2.13 shows the experimental data of the flow rate as a function of the electric current in a range of 0 to 2 mA corresponding to a working voltage from 10 to 60 V. The figure also shows three lines corresponding, respectively, to a linear fit of the experimental data, the theoretical prediction of Jang & Lee using a 1D model, and the results obtained with the present 2D model. Notice that the latter is a much better prediction than the 1D model. Jang & Lee mentioned that in the experiments the generation of bubbles due to electrolysis was considerable and leads to higher flow rates than the model results. For the sake of comparison, we note that in order to our model coincide with the linear fit of the experimental data, the dimensionless slip length at the electrodes should be $\alpha = 0.015$.

Lemoff & Lee^[43] considered an AC micropump in which a sinusoidal electric current is used with a perpendicular, synchronous AC magnetic field from an electromagnet to produce a continuous flow. In order to avoid electrolysis at higher electric currents, the operation frequency of the micropump was 1 kHz. The microchannel has a trapezoidal cross-section with a top channel width of $800 \mu\text{m}$ and an electrode area of $4 \text{ mm} \times 380 \mu\text{m}$. In Figure 2.14, the experimental data for the flow velocity of a 1 M NaCl solution is shown as a function of the applied

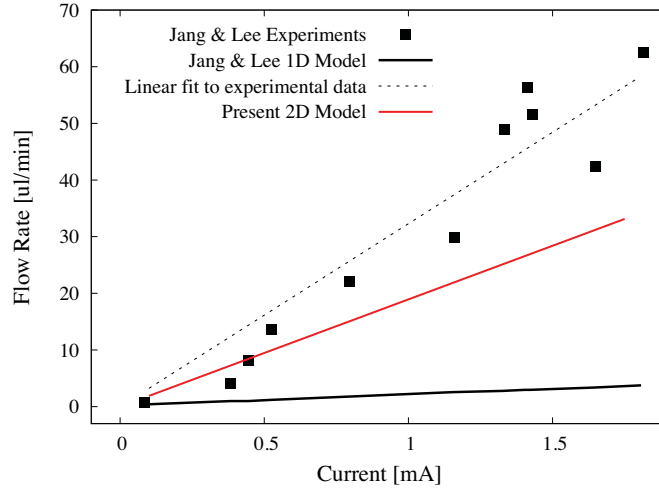


Fig. 2.13. Flow rate as a function of the electric current for a DC micropump analyzed by Jang & Lee^[41] using sea water as conducting fluid. Experimental data are compared against a linear fit of these data, the theoretical prediction of Jang & Lee using a 1D model, and the results obtained with the present 2D model.

magnetic field. Both the linear fit to the experimental data and the results obtained with our 2D model are shown. Although our theoretical model considers a DC pump with a rectangular cross-section, we approximated the experimental conditions by using the RMS value of the electric current and the same area of the electrodes. Incidentally, the model results coincide with the fitted curve when the dimensionless slip length at the electrodes is $\alpha = 0.056$.

2.1.8 Conclusions

A systematic study of the effect of the slip condition in MHD micropumps has been presented. Attention was focused on fully developed laminar flows in a parallel plate channel as well as in ducts of constant rectangular cross-section at low Hartmann numbers which is usually the condition of operation of these devices. The analyzed solutions capture fundamental aspects of the effect of slippage in MHD micropumps. Three different cases were explored, namely, flows with slip at the Hartmann walls (perpendicular to the magnetic field), flows with slip at the side walls (parallel to the magnetic field), and flows with slip at both the Hartmann and the side walls. In the limit of no slip ($\alpha \rightarrow 0$), the solutions presented here synthesize most of the solutions available in the literature to analyze MHD micropumps. A substantial increase in the flow rate created by the slip condition was found in the different cases. For instance, when the slip condition exists only at the Hartmann walls, for $Ha < 1$ and $\epsilon = 0.5$ the flow rate increases up to 23% for a slip length of one twentieth of the characteristic length and around 5% with one hundredth of this length. In addition, in the perfect slip case, the flow rate is largely influenced by the aspect ratio, observing an increase as the aspect ratio

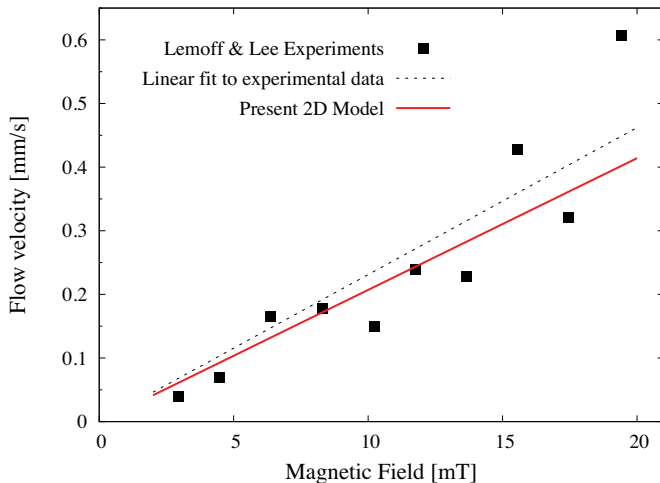


Fig. 2.14. Flow velocity of an electrolytic solution (1 M NaCl) as a function of the applied magnetic field for the AC micropump analyzed by Lemoff & Lee^[43]. The experimental data as well as the linear fit to these data and the results obtained with the present 2D model are shown.

decreases. In contrast, when the slip condition is applied at the side walls (where electrodes are located), for the same values of Ha and ϵ , increments of 10% are found for a slip length of one twentieth of the characteristic length and around 3% with one hundredth of this length. In turn, in the perfect slip case at the side walls, the flow rate becomes independent of the aspect ratio. Evidently, the largest increase in the flow rate corresponds to the case where the slip condition exists at the four walls in which case a linear increase of the flow rate with the dimensionless slip length is found. In order to validate our theoretical model, a comparison with available experimental data was carried out and, in general, a satisfactory agreement was found. The solutions presented here with and without slip can be used to design MHD micropumps and characterize the flow behavior in these microfluidic devices.

2.2 Experimental study of a MHD pump in an open channel

Although there are several experimental reports in the literature on the performance of MHD micropumps under different conditions, most of the studies are focused on the overall flow characteristics, for instance the flow rate, and how it is affected by geometry and operation conditions. However, the detailed flow patterns that occur in such devices are less explored and therefore, the possibilities to compare theoretical velocity profiles with experimental results are rather scarce. In this section, we present the Particle Image Velocimetry measurements of a flow driven by a MHD pump in an open channel forming a closed circuit. The ex-

periment is not carried out in a microdevice but in a conduit with length scale of the order of millimeters although laminar flow regime always prevails. Under these conditions the non-slip condition applies at rigid walls. The use of an open channel to explore the electromagnetically driven flow makes easier the visualization of velocity fields and allows a detailed analysis of the flow, particularly in the electrode zone which greatly influences the performance of these devices. Incidentally, some experimental characterizations of MHD micropumps have been carried out using open channels^[44,66]. There is an additional motivation for the study of open channel driven flows. In fact, Wu et al.^[67] have used rectified ac electro-osmotic flows in open microchannels in order to transport particles, cells, and other microorganisms. These authors argue that the use of open microchannels instead of closed microchannels is advantageous since the physiological conditions for normal cell growth can be maintained while accurate amounts of chemical and biological materials can be introduced. On the other hand, embedded open microchannels have also been proposed to reduce loss of available energy in convective heat transfer problems of viscous gas flow over a flat surface^[68]. As a matter of fact, the proposal of using MHD micropumps in open microchannels for fluid transport has also deserved attention^[69]. We now proceed to present the experimental characterization of the flow driven by a MHD pump in an open channel.

2.2.1 Experimental Setup

The experimental setup consists in an open channel forming a closed loop where a conduction MHD pump drives an electrolytic fluid. The channel with a constant rectangular cross-section 3 mm height and 16 mm width, and a total length of 920 mm measured along the centerline of the channel, is embedded in an acrylic plate of 5 mm thickness. The loop has two long sections (259 mm) joined with a short section (172 mm) at right angles and a semicircular section in the other extreme that prevents the formation of vortices due to the presence of sharp corners when the flow is driven in counter-clockwise direction (see Figure 2.15). The MHD conduction pump consists of two parallel graphite electrodes located in chambers along the channel side walls that keep them away from the main channel so that the bubbles generated by electrolysis do not interfere with the flow in the channel^[27,28]. A small and flat piece of acrylic is used to separate the electrode chamber from the main channel (bubble trap) leaving a 1 mm slit between the piece and the bottom of the channel, as show in detail of Figure 2.15. This slit was covered with filter paper in such a way that electric currents can flow from one electrode to the other but the fluid flow from the main channel to the chamber is avoided. A permanent Neodymium magnet with a square cross-section of 2 inches and 1 inch height was located beneath the acrylic plate so that the electrode region was under a mostly uniform vertical magnetic field which has a maximum intensity of 0.4 Tesla at the surface of the magnet. Once a voltage difference is applied to the electrodes, the resulting Lorentz force drives a flow along the loop. The polarity of the electrodes define the direction of the electric current and consequently the direction of the Lorentz force. In order to characterize the velocity fields in the open

channel, Particle Image Velocimetry (PIV) measurements were carried out. For this purpose, the channel has three glass windows that allow optical access to two zones of the flow (see Figure 2.15). The first zone, denoted as the pumping zone, is located where the electrodes and the magnetic field are present and is accessed from the short straight section. Referring to a Cartesian coordinate system as the one shown in Figure 2.15, PIV measurements in this zone correspond to $x - y$ flow planes (parallel to the bottom wall) at two different heights, $z = 1.5 \text{ mm}$ and $z = 2.9 \text{ mm}$ [§]. The second zone, namely the hydrodynamic zone, is located in the opposite long section of the loop, far away from the pumping zone so that the flow in this zone behaves as a hydrodynamic flow driven by an imposed pressure gradient. This zone can be accessed from the short straight section and/or from a lateral window in the long section. Therefore, in this zone PIV measurements were obtained not only in $x - y$ flow planes but also in the mid $x - z$ flow plane by introducing a laser sheet perpendicular to the bottom wall.

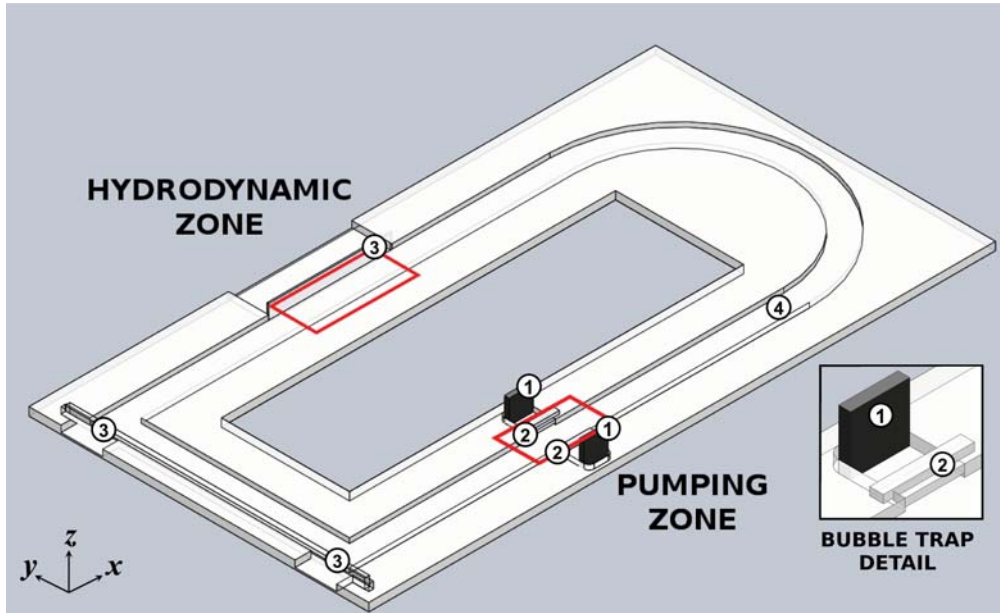


Fig. 2.15. Scheme of the MHD pump constructed on a $216 \times 404 \text{ mm}^2$ flat sheet of acrylic. ① Graphite electrode ② Bubble trap ③ Glass window ④ Main channel.

Two electrolytic working fluids were used, aqueous solutions of $\text{NaHCO}_3^{7.4\%wt}$ and $\text{KOH}^{20\%wt}$ whose physical properties are listed in Table 2.2. Electric current, I , varied from 10 to 140 mA. When the NaHCO_3 solution is used, a maximum current intensity of 60 mA was reached while for the KOH solution, the maximum current intensity was 140 mA.

[§]These heights correspond to the mid plane and the free surface. The laser sheet that has a width of approximately 0.7 mm.

Salt	Wt %	ρ [$kg\ m^{-3}$]	ν [$m^2\ s^{-1}$]	σ [$S\ m^{-1}$]
NaHCO ₃	7.4	1050 ^[70,71]	1.20×10^{-6} ^[72]	4.98 ¹
KOH	20	1199 ^[73]	1.288×10^{-6} ^[73]	54 ¹

Table 2.2. Physical properties of used electrolytes at 25° C. ¹Measured at CIE-UNAM laboratories.

Taking into consideration the values shown in Table 2.2 and the velocity magnitudes measured in the experiments (see Figure 2.17) the Reynolds numbers at which the experiments were performed are in the ranges $2.5 < Re_{NaHCO_3} < 15$ and $19 < Re_{KOH} < 51$, while the parameter β defined in Section 2.1.2 (just after Equation (2.12)) varies in the range $0.42 < \beta < 4.56$, considering a magnetic field intensity of 0.3 Tesla which is approximately the value in the flow region. In addition, the value of the Hartmann number when using sodium bicarbonate was $Ha=0.056$, while for the potassium hydroxide was $Ha=0.168$.

2.2.2 Results

Let us now present the PIV flow analysis carried out in the two sections of the open channel. We first present the experimental results obtained in the hydrodynamic zone.

2.2.3 Hydrodynamic zone

A convenient parameter to determine whether a flow can be considered as fully developed or not is the *entrance length* L_e . This length defines a boundary between the fully developed flow and the non-developed flow, characterized by a dependence on the coordinate in the main flow direction. Taking the hydraulic diameter ($D_h = 8.72$ mm) as characteristic length scale, for the highest Reynolds number in the experiment, namely $Re = 51$, the entrance length is 22 mm. This length was computed with the formula for laminar flows, $L_e = 0.05 D_h Re$ ^[74]. Therefore, in all analysed cases, the entrance length is smaller than the distance from the output of the semicircular section to the testing section which is approximately 100 mm. Hence, the flow can be considered fully developed in all cases.

Velocity field in the $x - y$ plane

The first column of Figure 2.16 shows the vector velocity field in the $x - y$ plane at a height $z = 2.9$ mm and the magnitude of the velocity ($U = \sqrt{u^2 + v^2}$) in colors in the hydrodynamic zone for two different applied electric currents. The second column shows in colors the magnitude of the axial velocity component u . These plots correspond to velocity fields averaged over the duration of the entire experiment. Comparing magnitudes of u and v , we may conclude that the transversal component v is much smaller than the axial component u , namely, the fully developed flow assumption is correct. It can be observed that the maximum velocities are located in the center of the channel, and increase as the applied electric cur-

rent grows. The “spots” that appear in the lower part of figures correspond to reflections of the glass window that introduce noise in those areas.

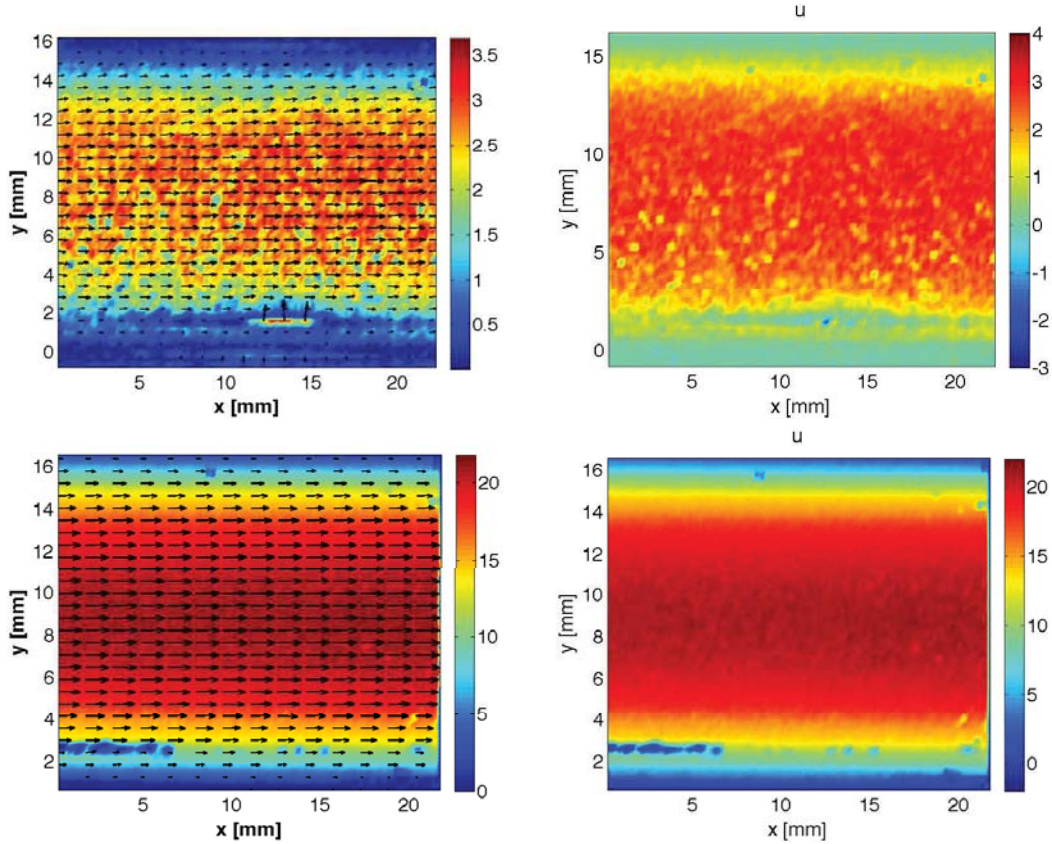


Fig. 2.16. Left column: Velocity field with its magnitude U in colors. Right column: magnitude of the axial component of the velocity u . Measurements correspond to the $x - y$ plane at the free surface ($z = 2.9$ mm). Velocity in mm/s. $I = 20$ mA (first row) and 140 mA (second row).

We now proceed to present the axial velocity profiles as a function of the transversal coordinate y for different Reynolds numbers, that is, different electric current intensities. The profiles, $u(y)$, were obtained by averaging the vertical component all along in the main flow direction x . Figures 2.17 and 2.18 show the velocity profiles as a function of the y -coordinate at the free surface ($z=2.9$ mm) and at the midplane ($z=1.5$ mm), respectively. The explored Reynolds numbers varied from 2.5 to 51 corresponding to current intensities of 10 mA and 140 mA, respectively.

We observe that the profiles are not perfectly parabolic. This could be attributed to the fact that the free surface is not completely flat, namely, a meniscus is formed in the upper corners of the cross-section of the channel. This meniscus, in addition to modify in some way the velocity profile, reflects the light of the laser sheet causing the “spots” mentioned previously. It is important to note that at

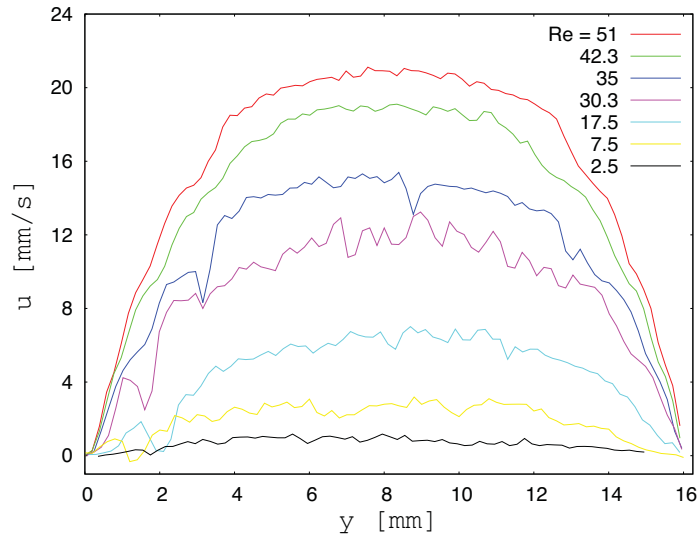


Fig. 2.17. Axial velocity profile, in the free surface of the channel in the hydrodynamic zone, as function of transversal y -coordinate for the different Reynolds numbers explored.

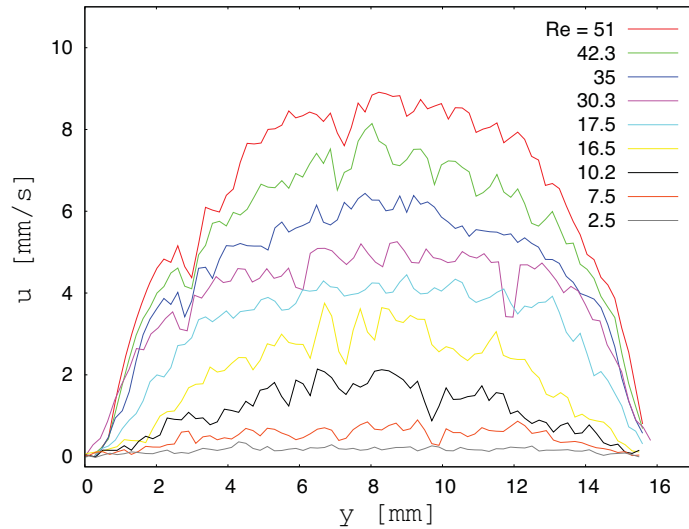


Fig. 2.18. Axial velocity profile, at the mid $x-y$ plane ($z=1.5$ mm) in the hydrodynamic zone, as function of transversal y -coordinate for the different Reynolds numbers explored.

small velocities (low electric current densities) fluctuations are higher and diminish as the electric current increase.

Velocity field in the $x-z$ plane

The velocity field in the $x-z$ vertical plane limited by the bottom wall and the free surface was also explored. The plane is located at the mid distance between

the lateral walls. In this case the applied electric current varied from 60 to 140 mA using the solution of KOH as working fluid, corresponding to a Reynolds number range $19 < Re < 51$. The left panel of figure 2.19 shows the vector velocity field and its magnitude U in color scale. In the right panel, the magnitude of the axial velocity component u is shown in color scale. We may infer from the magnitudes of the velocities that the vertical component w is much smaller (at least one order of magnitude) than the axial component u . This again corroborates that the flow is fully developed.

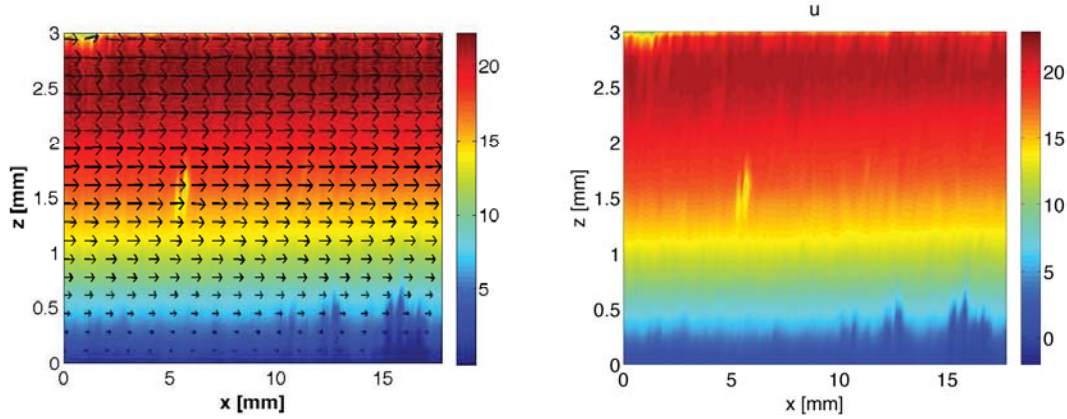


Fig. 2.19. PIV measurements in the mid $x - z$ plane. Left panel: Vector velocity field and its magnitude in color scale. Right panel: Magnitude of the axial velocity component u . Velocity in mm/s. $I = 140$ mA.

Figure 2.20 shows the axial velocity profile as a function of the vertical z -coordinate for different Reynolds numbers. We observe that the velocity increases as the injected current (Reynolds number) grows. As expected, semi-parabolic profiles are obtained with a non-slip condition at the bottom wall and the maximum velocity very close to the free surface. Note however that at the top of the profile the velocity presents a small decrease. This is probably due to the presence of the meniscus at the free surface. Additionally if we compare results obtained in both analysed planes we find that velocities shown in Figures 2.19 and 2.20 coincide with the corresponding velocities shown in Figures 2.17 and 2.18.

2.2.4 Pumping zone

In this zone the flow has a more complex structure in part due to the inhomogeneity of the magnetic field but mainly due to the electric current paths that give rise to an inhomogeneous distribution of the Lorentz force. In this zone asymmetric flow recirculations exist. It seems that recirculations are produced by short circuit of the electric current paths at the edges of the electrodes. For this reason, the maximum velocity is found in the center of the channel in the streamwise direction, while near the electrodes the fluid moves in opposite direction, as shown in Figure 2.21. This figure shows the PIV measurements in the $x - y$ plane at the free surface ($z=2.9$

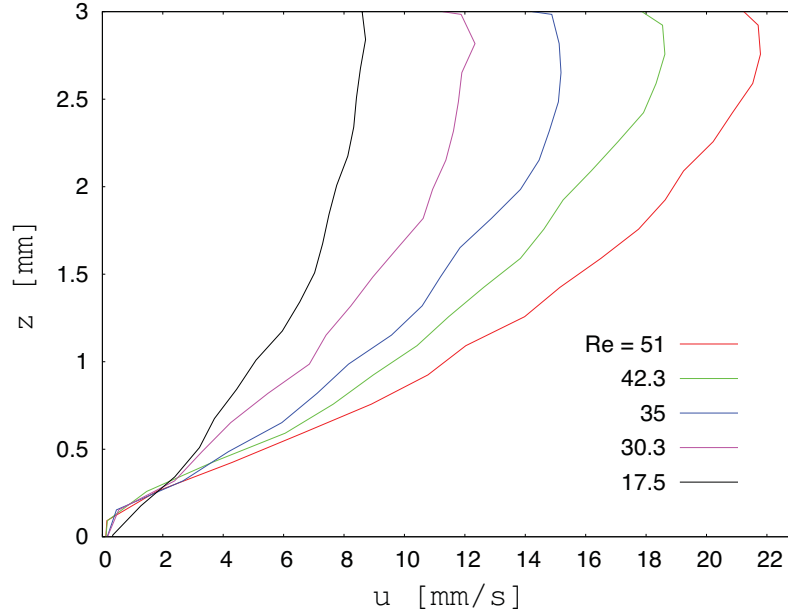


Fig. 2.20. Axial velocity profile in the $x - z$ middle plane of the channel in the hydrodynamic zone, as function of z for different Reynolds numbers.

mm) for three different electric current intensities. The left column shows vector velocity fields where the colors represent the magnitude of the velocity vector. The right column shows in colors the magnitude of the axial velocity component u . In all cases the global flow of the electrolyte is from left to right and the electrodes are located from $x=5$ mm to $x=20$ mm.

In the first row of Figure 2.21 corresponding to the lowest current intensity explored ($I=20$ mA), we observe that two recirculation zones are clearly formed in the electrode zone. In the center of the channel the liquid flows in the direction of the global motion (from left to right) while near the side walls (electrode region) the liquid flows in the opposite direction. The flow field is approximately symmetric with respect to the axial midline. Note that the recirculation loops extend downstream beyond the location where the electrode region begins ($x=5$ mm) and, upstream, reaches approximately the end of this region ($x=20$ mm). Also, note that in the center of the recirculation loops a stagnation zone is formed. We can also observe the maximum axial velocity is reached in the center of the channel and, in the opposite direction, in small zones close to the side walls at the entrance of the electrode region. As the electric current increases, the Lorentz force is intensified, the fluid velocity increases and inertial effects become important (see second and third rows in Figure 2.21). For the current intensity of $I=60$ mA (second row in Figure 2.21), the recirculation loops persist but they are elongated downstream while the symmetry of the flow with respect to the axial midline is slightly altered. Finally, for the higher applied electric current ($I=140$ mA, third row in Figure 2.21), the flow becomes disrupted. We notice that the maximum axial velocity is

almost twice its value with respect to the case with 60 mA. Note that the flow symmetry is lost and although recirculation loops persist, the one close to the side wall at $y=15$ mm is larger than the one at $y=0$ mm. In fact, we observe that the recirculation loops obstruct the flow near the side walls so that the fluid is accelerated through the center of the channel where it reaches the maximum velocity. However, as shown in Figure 2.22, the maximum transversal velocity v in these loops (approximately 15 mm/s) does not change significantly with the variation in the current intensity, from $I=60$ mA (left) to 140 mA (right). We notice that the main difference is its distribution. For the smaller current intensity ($I=60$ mA), the maximum velocities are located in the front part of recirculation zones and have a “waxing crescent moon” form, while behind them the velocity is uniform and smaller. On the other hand, when an electric current $I=140$ mA is applied, the maximums are dragged downstream by inertial effects and their form is not maintained. In this case, more regions of high velocity appear. This shows that at high electric current intensities a very complicate flow structure appears in the pumping zone, where three dimensional effects seems to be very important despite the shallowness of the flow.

2.2.5 Conclusions

The flow in an open channel forming a closed loop and driven by a conduction MHD pump at millimetric scale was studied using the PIV technique. Two different electrolyte solutions were used as working fluids allowing electric current densities up to 140 mA. The flow in the constant cross-section channel was analysed in two zones: the pumping zone, where the electrodes and magnet are placed, and the so-called hydrodynamic zone, where the driving Lorentz force is manifested only as constant pressure gradient along the channel. It is precisely for this reason that in the hydrodynamic zone, Poiseuille-like flows were observed. Results obtained in this zone in both analysed planes are in complete agreement and confirms the validity of fully developed flow assumption. On the other hand, the flow in the pumping zone is more complex, showing recirculation regions close to the side walls in the electrode zone. For the lowest analysed current intensity ($I=40$ mA) the magnitude of velocity in recirculation zones is comparable to the velocity at the center of the channel. As the current is increased the magnitude of velocity in recirculation zones becomes just a small fraction of that in the central channel region. Several experimental arrays were performed in order to ensure that the recirculation regions were not produced by flow between the main channel and the electrode chambers. Although a more extensive analysis should be carried out, so far experimental results point to the conclusion that recirculation regions are due to paths of electric current. Apparently, at the edges of the electrodes the path of electric current is not transversal to the side walls but is bent so that electric current density has components in the axial and vertical directions. This leads to a non-uniform distribution of the Lorentz force and the appearance of recirculations. In order to confirm this hypothesis, a full numerical simulation of the flow is required. The understanding of this phenomenon is important since the

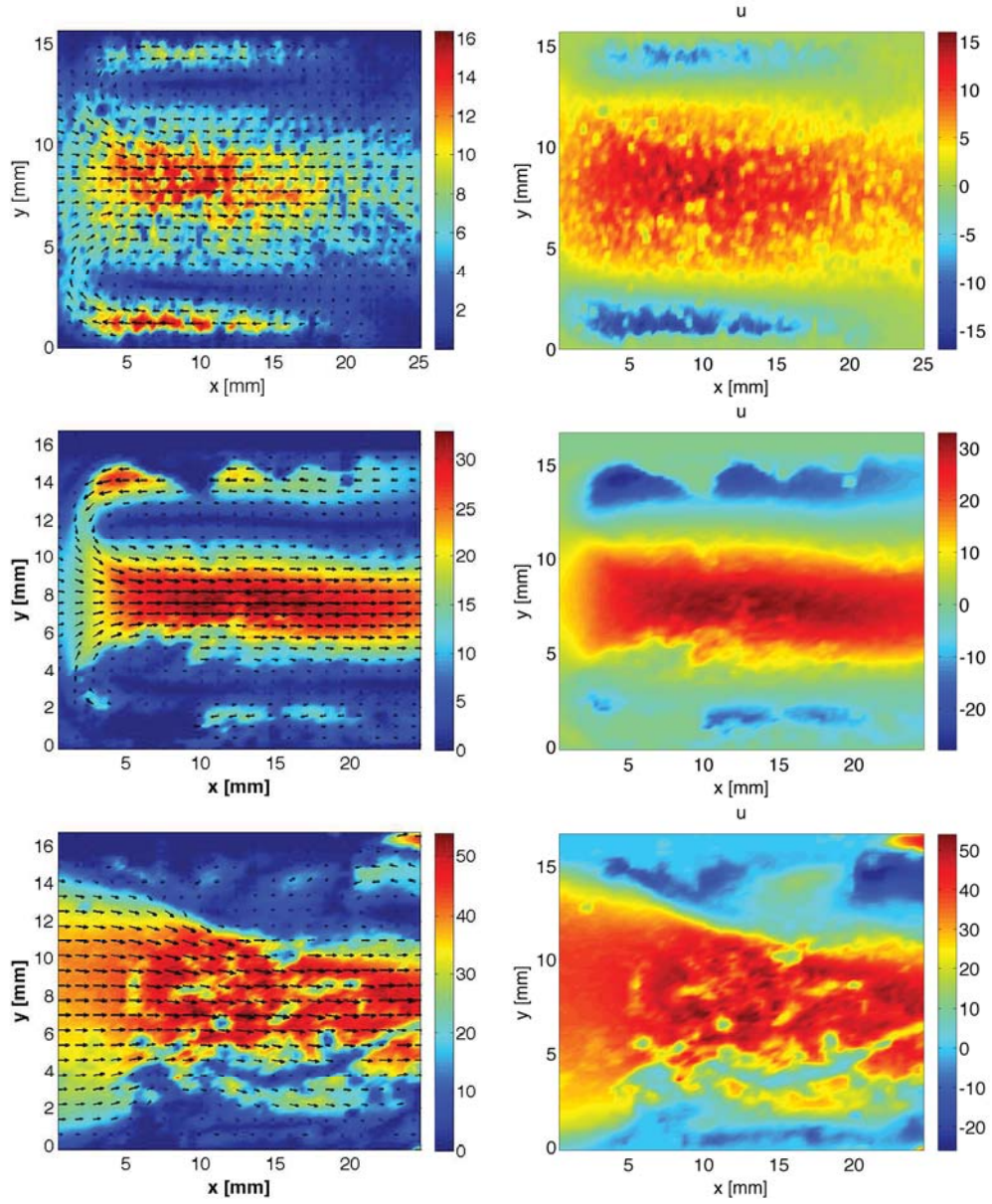


Fig. 2.21. Left column: vector velocity field with its magnitude U in colors. Right column: magnitude of the axial component of the velocity u in the $x - y$ plane at the free surface ($z=2.9$ mm) in the pumping zone. Velocity in mm/s. First row: $I = 20$ mA. Second row: $I=60$ mA. Third row: $I=140$ mA.

existence of recirculation regions in the pumping zone affects the performance of MHD pumps.

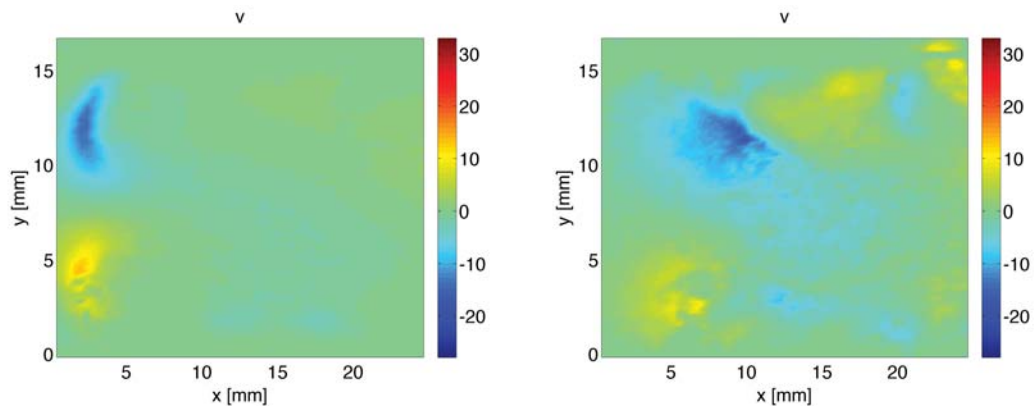


Fig. 2.22. Magnitude of the transversal component of the velocity v in the $x - y$ plane at the free surface ($z=2.9$ mm) in the pumping zone. Velocity in mm/s. Left: $I=60$ mA. Right: $I=140$ mA.

Chapter 3

Duct flows in localized and non-uniform magnetic fields[§]

In this chapter, experimental results of liquid metal flows past localized magnetic fields, also known as magnetic obstacles, are presented in two configurations. First, a pump driven flow through the gap of two permanent rectangular magnets smaller than the duct's width in a duct of constant rectangular cross-section is analysed. Secondly, the flow produced by a rectangular magnet dragged upon the free surface of a quiescent liquid metal layer is explored. Different flow regimes were analyzed by varying the Reynolds number, paying particular attention to vortical flow patterns. Experimental measurements were obtained through Ultrasound Doppler Velocimetry (UDV). In addition, UDV results of the pump driven liquid metal MHD flow in a closed loop called Electromagnetic Flow Control Channel (EFCO) are presented. Clockwise (CW) and counter-clockwise (CCW) flow directions, that produce M-shape and parabolic profiles, respectively, were studied. From the experimental data, the mass flow rate was computed.

3.1 Liquid metal flow past a magnetic obstacle

The study of flows past solid obstacles has been the source of many fundamental advances in hydrodynamics. Topics such as stability, intermittency and transition to turbulence find their classical examples on this problem. In fact, the behaviour of flows past bluff bodies (v.e. cylinders), and particularly the structure of the wake behind them, is probably one of the best studied problems in fluid mechanics^[75]. In turn, wakes in magnetohydrodynamic (MHD) flows present also interesting challenges and so far have been very poorly explored. In recent years, several studies (mainly theoretical) have called the attention to liquid metal MHD flows in strongly localized magnetic fields where induced Lorentz forces generate steady or time-dependent flow patterns that, in some aspects, resemble flows past solid

[§]Part of this chapter was published in: M. Rivero, O. Andreev, A. Thess and S. Cuevas *Experimental study of flows past a magnetic obstacle* Proceedings of the 8th PAMIR International Conference on Fundamental and Applied MHD, (2011) Vol 1, pp. 347-351

obstacles^[30,32–34,76]. In fact, the abrupt transition between regions of none or very small magnetic field and a localized region with intense field may develop vortical structures and eventually instabilities that remind those observed in flows interacting with bluff bodies^[30–32]. Incidentally, the term magnetic obstacle was coined^[30] to emphasize that breaking Lorentz forces act as an obstacle for the flow.

Although pioneering studies by Ge'ftgat et al.^[77] called the attention on the possibility of realizing complex velocity structures in flows under non-uniform magnetic fields, experimental results failed to confirm this fact^[78]. The confirmation that steady and time-dependent vortical patterns may appear in liquid metal flows past localized magnetic fields came many years later from quasi-two-dimensional numerical simulations which showed the appearance of two elongated streamwise steady vortices in the wake which may give rise to a vortex shedding flow when a critical Hartmann number is reached for a given Reynolds number^[30]. In the case of creeping flow conditions, steady vortices were found inside the localized magnetic field region^[76]. Interesting studies have exploited the analogy between flows past solid and magnetic obstacles^[33,79] but, as it has been recognized, quite remarkable differences exist between these two physical situations.

As a matter of fact, only a few experimental studies have been performed in order to discern the behaviour of these flows^[34]. For instance, some properties of the steady wake of a magnetic obstacle have been explored but a detailed analysis of the topological behaviour of the streamline patterns in the time-dependent regime is not completed.

The flow past a magnetic obstacle is governed by two physical parameters, namely, the Reynolds number, $Re = \frac{U_0 H}{\nu}$, and the Hartmann number $Ha = B_0 H \sqrt{\frac{\sigma}{\nu \rho}}$ (or alternatively the magnetic interaction parameter $N = \frac{Ha^2}{Re} = \frac{\sigma B_0 H}{\rho U_0}$), where U_0 , H , and B_0 , are the characteristic scales of velocity, length and magnetic field, while ρ , ν , and σ , are the mass density, kinematic viscosity, and electrical conductivity of the fluid. In addition, a geometric parameter, the constraintment factor^[32], $\kappa = \frac{M_y}{L_y}$, where M_y and L_y are the half-widths of the external magnet and the duct in the spanwise direction (see Figure 3.1 below), is also important to determine the flow topology. The variation of these parameters leads to a very rich dynamic behaviour. This section offers new experimental results of the flow past a magnetic obstacle in two configurations. In section 3.1.1, a pump driven fully developed flow in a rectangular duct is considered, where two permanent rectangular magnets placed at the top and bottom walls form the magnetic obstacle (see Figure 3.1). In section 3.1.2, a developing free surface flow in a liquid metal layer created by dragging a permanent rectangular magnet close to the liquid surface is discussed. In both cases κ and Ha were fixed, while Re was varied. The eutectic alloy Ga^{68%}In^{20%}Sn^{12%} was used as working liquid. The material properties of GaInSn are given in the Table 3.1. Measurements were carried out using the Ultrasonic Velocity Profile method (UVP)^[34]. In this technique velocities are derived from shifts in position between pulses, and Doppler effect plays a minor role because the measured velocity is much smaller than the speed of sound in the

Density [$kg\ m^{-3}$]	6360
Dynamic viscosity [$kg\ m^{-1}\ s^{-1}$]	2.2×10^{-3}
Kinematic viscosity [$m^2\ s^{-1}$]	3.3×10^{-7}
Surface tension [$N\ m^{-1}$]	0.533
Electrical conductivity [$\Omega^{-1}\ m^{-1}$]	3.46×10^6
Sound velocity [$m\ s^{-1}$]	2725
Heat conductivity [$W\ K^{-1}\ m^{-1}$]	39
Specific heat [$J\ kg^{-1}\ K^{-1}$]	39
Magnetic permeability [$N\ A^{-2}$]	$4\pi \times 10^{-7}$
Melting temperature [$^{\circ}C$]	10.5

Table 3.1. Physical properties of Ga^{68%}In^{20%}Sn^{12%} at 20 °C.

medium^[80]. The UVP method is based on pulsed echography and has been widely described in the literature (see for instance^[81]).

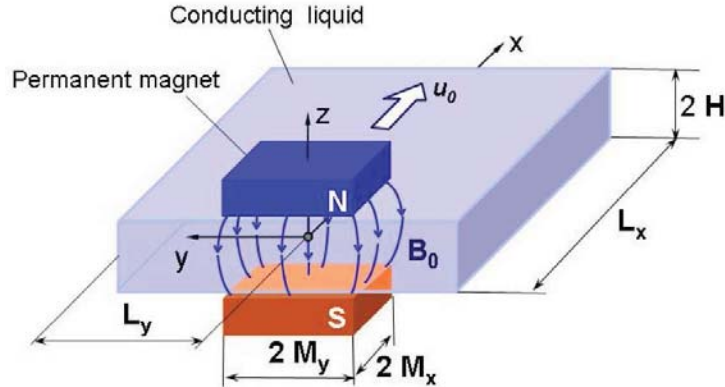


Fig. 3.1. Scheme of the magnetic obstacle (taken from Ref.^[31]).

3.1.1 Magnetic obstacle in a rectangular duct

The experimental setup used in this case was described in detail in a previous study^[34] where liquid metal flow measurements were carried out through the UVP method. The flow took place in a Plexiglas rectangular duct of 20 mm height (H), 100 mm width (L) and 500 mm length (see Fig. 3.2). An electromagnetic pump based on rotating permanent magnets drives the liquid metal in a horizontal loop, with a flow rate up to $2\ lt\ s^{-1}$. At the inlet of the test section a honeycomb was placed to reduce velocity disturbances of the entrance flow. Two rectangular NdFeB permanent magnets (30 mm in streamwise direction and 40 mm in spanwise

direction) with a maximum intensity of 0.4 Tesla, coupled by a steel yoke, were placed at a distance of 120 mm from the honeycomb. With the dimensions of the duct and magnets the constraint factor was fixed to $\kappa = 0.4$. Under these conditions, the Reynolds number based on the mean velocity U_0 varied within the range of $500 < Re < 16000$, while the Hartmann number based on the maximum magnetic field strength, B_0 , was equal to $Ha=320$. In order to characterize the flow, an 8 mm diameter 8 MHz long case transducer^[80] was placed on the axis of the channel at half of its height, as show in Fig. 3.2. In this way, using the UVP the velocity component in direction of sound beam propagation, which corresponds to the flow symmetry line, was measured. These measurements were used to determine the flow structure in the explored range of Reynolds numbers.

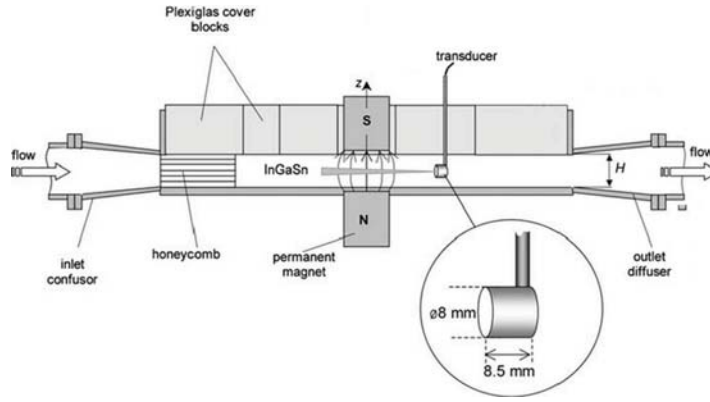


Fig. 3.2. Sketch of experimental test section (taken from Ref.^[34]).

Since the opposing Lorentz force breaks the flow in the localized region where the magnetic field is strong, a stagnant or recirculation zone is created so that the oncoming liquid flows around it, as occurs in the flow past a bluff body. The resulting pattern in the flow past a magnetic obstacle depends on the relative strength of inertial, viscous, and Lorentz forces^[30,33] although geometrical considerations are also important^[32]. Flow regimes with no vortices, steady vortices, or vortex shedding have been reported in recent numerical and experimental studies^[30–34]. Although attempts have been made to describe the scenario for the flow past a magnetic obstacle as the governing parameters are varied^[30,32,33], due to the enlarged parameter space (compared with the hydrodynamic flow past a solid obstacle) only a restricted scenario has been explored so far. For the configuration treated here, a stationary flow pattern that greatly differs from the one of the classical wake behind a solid cylinder has been found for restricted values of the Reynolds number^[31,34,82]. The steady pattern involves the existence up to six vortices that appear as a consequence of two flow bifurcations^[31]. This pattern is shown in Fig. 3.3 where streamlines for time averaged flow past a magnetic obstacle are plotted for $Re=4000$, $Ha=320$, and $\kappa = 0.4$.

Dashed lines denote the borders of the permanent magnets. Inside this zone, a pair of vortices, the so-called magnetic vortices, are located. Just behind it, a pair

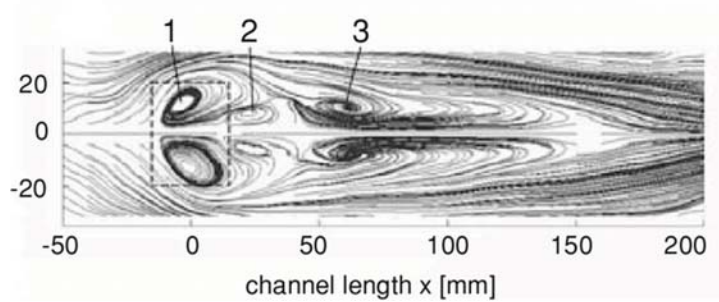


Fig. 3.3. Streamlines for the time averaged flow over a magnetic obstacle at $Re=4000$, $Ha=320$, $\kappa = 0.4$. **1)** magnetic vortices; **2)** connecting vortices; **3)** attached vortices^[34].

of connecting vortices are found that connect the magnetic vortices with the last pair of vortices, the attached vortices, which show the same direction of rotation as the magnetic ones. The existence of these vortices can be discerned by plotting the streamwise component of velocity u/U_0 , measured along the ducts axis, as function of the duct length. This is shown in Fig. 3.4 for different Re , where the dashed lines mark the location of the magnets. In fact, the main objective of the present work was to explore the transition between different flow patterns as the Reynolds number varies. Note that negative values of u/U_0 indicate the appearance of reverse flow. As the Re grows, a non-monotonic behaviour is observed: the pattern displays no vortices ($Re = 250$), two vortices ($Re = 500$), six vortices ($Re = 915$), and again two vortices ($Re = 2045$). From $Re = 2200$ up to $Re = 8000$, that corresponds to $15 < N < 41$, six vortices are found. The most notorious fact is that the length of vortices, as well as their local maximum velocity, reach a peak at different Re and then decrease with the growth of this parameter (see Fig. 3.4). Although not shown in Fig. 3.4, in the range $8000 < Re < 9660$ two vortices were observed between 40-120 mm (attached vortices zone), while for $9660 < Re < 14025$ no vortices were found. In fact, in this large Reynolds number range, inertial forces overcome completely magnetic forces so that the magnetic obstacle becomes “transparent” for the flow. The presence of vortices can be observed in Fig. 3.5 as non-zero values of velocity or length for a given Reynolds number.

Figures 3.5 show the length of vortices and local maximum dimensionless velocity, respectively, as function of Reynolds number for all vortex duplets. It can be observed that the length of magnetic vortices remains approximately constant up to $Re \sim 3000$ where the length of connecting and attached vortices reaches its maximum. It has to be noticed that maximum values of velocity and length for a given pair of vortices are not reached at the same Reynolds number. The observed transitions in the flow patterns as Re grows confirms the rich behaviour and complexity of the flow past a magnetic obstacle.

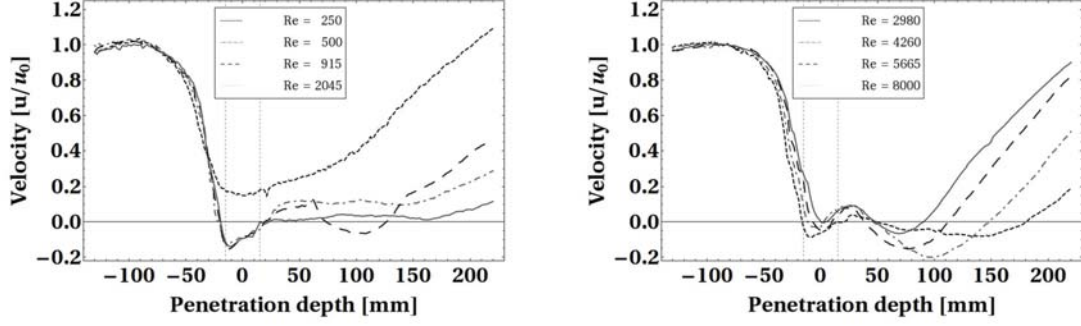


Fig. 3.4. Streamwise velocity component u/U_0 measured by UVP on the axis of the liquid metal channel for different Re . Dashed lines represent the position of the magnet.

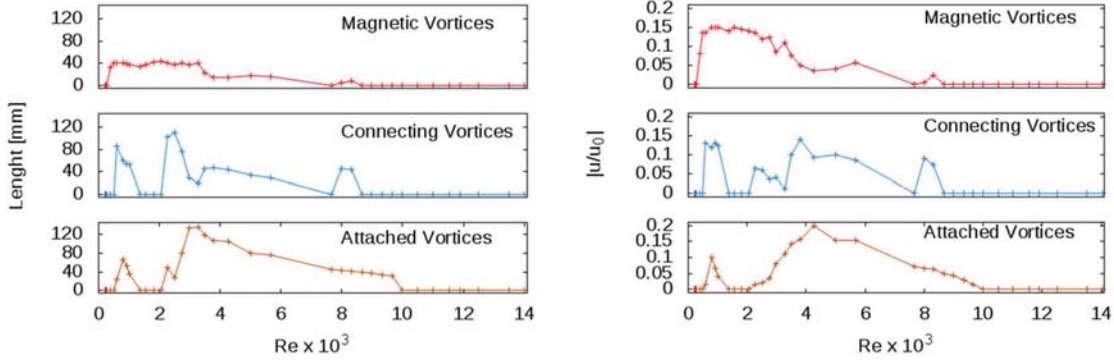


Fig. 3.5. **a)** Length of vortices, and **b)** local maximum dimensionless velocity as function of Reynolds number for the three pair of vortices.

3.1.2 Magnetic obstacle in free surface flow

In this section, experimental results of a magnetic obstacle flow in a free liquid metal surface are presented. The experimental setup consists of an open rectangular container 104 mm width and 640 mm long filled with a 43 mm layer of liquid metal (GaInSn). The flow was produced by dragging a permanent rectangular magnet at constant velocity above the free surface (see Figure 3.6). The minimum allowable separation between magnet and fluid was 1 mm due to instabilities in its surface produced by the dragging effect. The maximum displacement and velocity of the magnet was 370 mm and 35 mm/s, respectively. Taking the half height of fluid layer as characteristic length, $Ha = 344$, while Re ranged from 632 to 2213 (correspondingly N varied from 54 to 187). With the same magnet dimensions as in the previous experiment, $\kappa = 0.4$. An 8 mm diameter 8 MHz short case transducer was immersed directly into the fluid (at 4 mm from free surface) to characterize the flow. The transducer was coupled to the dragging system so that both the magnet and the transducer, separated by a distance of 115 mm, moved at the same velocity (see Figure 3.6). The signal was recorded as soon as the mag-

net started to move, therefore, the developing flow in a time interval that varied according to the Reynolds number was analyzed. Figure 3.7 shows the evolution of the normalized streamwise component of velocity u/U_0 measured by UVP on the axis of the liquid metal channel for $Re = 1897$. In this case, the fully developed flow was reached after approximately 13 s. This time interval increases as Re decreases and reached 37 s for the lowest value explored ($Re = 632$).

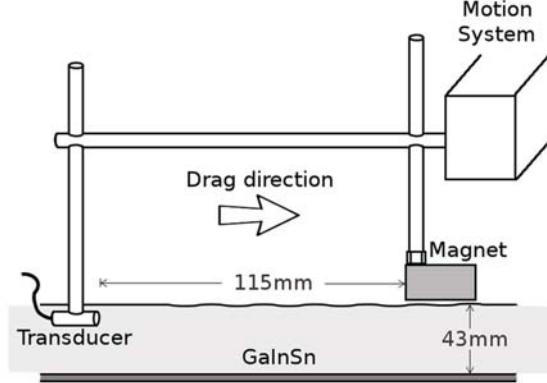


Fig. 3.6. Sketch of experimental test section.

In the velocity profiles of Figure 3.7, corresponding to $Re = 1897$, the origin coincides with the position of the center of the magnet and the dashed lines indicate its length. Upstream the magnet the velocity reaches its maximum value and then decreases in the region affected by the magnetic obstacle due to the opposing Lorentz force. Note however that no negative velocities were measured indicating that recirculation flows were absent. Due to limitations of the experimental setup, in particular the length of the container, it was not possible to reach the range of interaction parameters where vortex flows appear. Nevertheless, some interesting results about the developing wake can be observed. Early times, when the wake begins to grow, are characterized by a constant minimum velocity zone that reaches its maximum length at ~ 3 s (see Figure 3.7 left). Afterwards, the fully developed profile begins to form, reaching its final state at ~ 12 s (see Figure 3.7 right). In this state, in the far wake (at 120 mm from magnets center) the velocity is $\sim 45\%$ of the maximum velocity, but far enough it should reach the maximum velocity. In fact, in all analyzed cases the wake formation mechanism is analog. In Figure 3.8 the fully developed profiles as function of the channel length are shown for all Reynolds numbers explored. As can be observed, all the profiles within this range of Re are very similar. It is also important to notice that in this flow regime the minimum velocity is obtained just behind the magnet zone.

3.2 Electromagnetic flow control channel

Control of molten metal flow using magnetic fields is highly important in industrial applications^[29,83]. The Electromagnetic Flow Control (EFCO) channel^[84] is

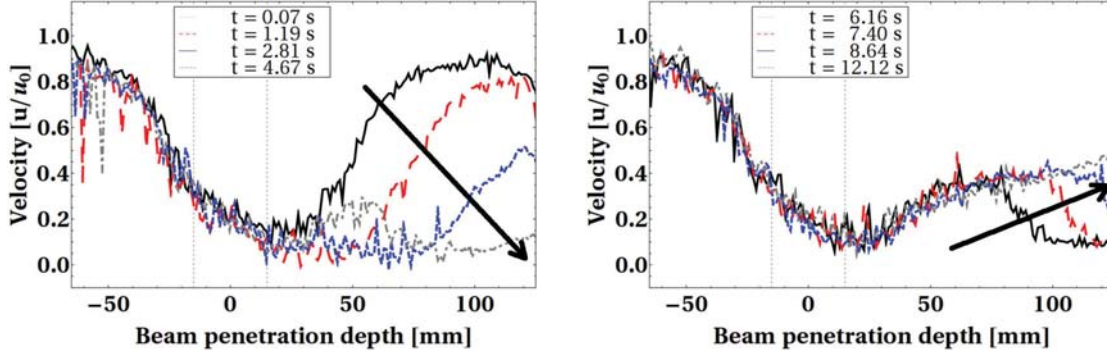


Fig. 3.7. Evolution of the streamwise component of velocity u/U_0 measured by UVP on the axis of the liquid metal channel for $Re = 1897$. Arrows show the time direction of the evolving profiles. Total time of experiment: 12.39 s.

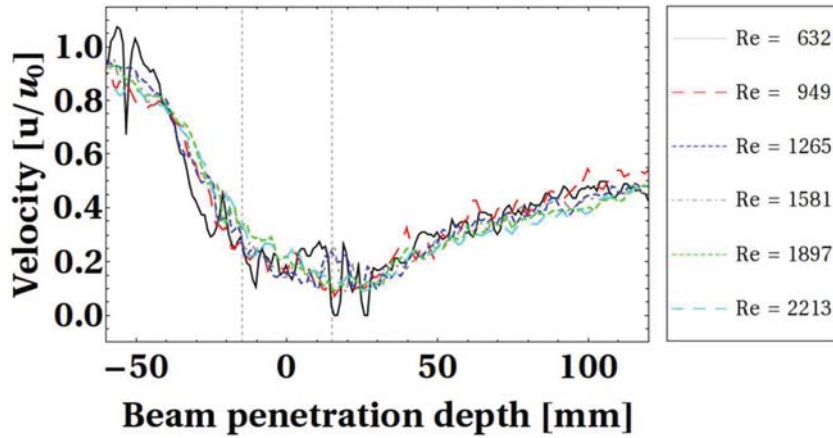


Fig. 3.8. Fully developed streamwise component of velocity u/U_0 measured by UVP on the axis of the liquid metal container for all experiments.

an experimental test facility, located at Ilmenau University of Technology, Germany, for the development of such kind of control systems. The working fluid is the low-melting liquid metal alloy GaInSn in eutectic composition. In this channel, flow control is realized by combining and coupling the non-contact flow driving technology of electromagnetic pumps based on rotating permanent magnets and the non-contact flow rate measurement technology called Lorentz Force Velocimetry (LFV)^[35–38,85]. The flow rate is adjusted by controlling the rotation frequency of the permanent magnet system. Physically, LFV is based on measuring the force acting on a localized magnet system placed as close as possible to a conduit that carries a liquid metal flow. This force is induced by the melt flow passing through the static magnetic field generated by the magnets. The magnitude of the force is proportional to the flow rate. To calibrate such flow meters, we apply UDV technique to measure and analyse both turbulent hydrodynamic and magnetohydrodynamic liquid metal flow profiles in EFCO at various Reynolds

numbers. In particular, in the present work hydrodynamic parabolic velocity profiles as well as M-shaped velocity profiles^[86], characteristic of MHD duct flows in non-homogeneous magnetic fields, were measured using the UDV technique and the mass flow rate was determined.

3.2.1 Experimental facility

The experimental setup consist in a rectangular loop 2.3 m long and a cross-section of 1 cm width and 8 cm height, filled with GaInSn, as shown in Figure 3.9^[84]§. The channel walls are made of an electrically insulating material (acrylic). The liquid metal is driven by an electromagnetic pump based on permanent magnet bars disposed radially in circular plates rotating^[87] at frequencies from 1 to 25 Hz which allow to reach Reynolds numbers in the range $7000 < Re < 65000$. A detailed explanation of the electromagnetic pump can be found elsewhere^[88–91]. In short, the working principle behind this pump is that the movement of a magnetic field in an electrically conducting media induces electric currents in it which interact with the rotating magnetic field and give rise to a tangential Lorentz force that “drags” the fluid in the direction in which the magnetic field moves inside the channel. This force is proportional to the rotation frequency, the magnetic field intensity and the electrical conductivity of the fluid. Thus by varying the rotation frequency of the magnets array, the velocity of the flow is controlled. It is important to point out that by reversing the rotating direction of the magnets array the flow direction is also reversed. The channel is equipped with a Lorentz force velocimeter (LFV) consisting of two permanent parallel magnets (10 cm in vertical direction and 3 cm in streamwise direction with a field intensity of 0.4 T) that generate a localized spanwise magnetic field. To analyse the channel liquid metal flow through this non-uniform magnetic field is one of the objectives of this work. This magnet system is supported by a strain gauge. When the melt flows through the static magnetic field produced in the gap of the parallel magnets, Lorentz forces are induced within the melt. These forces have a braking effect on the flow and are proportional to the flow rate. By Newton’s third law the fluid also drags the magnet system (LFV) producing a deformation sensed by the strain gauge. With the proper calibration, the voltage signal obtained from the gauge can be related to the flow velocity or flow rate. In addition to the LFV, the channel has different measuring devices, namely, a Vivés probe^[92], an orifice plate which allows measurements through electric potential probes (EPP), an orifice to measure the pressure drop, and an orifice to measure the velocity profile using the UDV. Figures 3.9 - 3.11 show the localization and position of the ultrasound (US) transducer.

In order to avoid oxidation of the GaInSn alloy, the channel is covered by an epoxical resin, as shown in Figs. 3.10 and 3.11. This enclosure ensures a perfect sealed system. UDV measurements were performed using a 5 mm diameter 8 MHz transducer. The US transducer is placed at the top of the cross section and points downwards with an inclination of 60° respect to the main flow direction (see Figure

§EFCO diagram proportionated by Dandan Jian from the Ilmenau University of Technology, Germany.

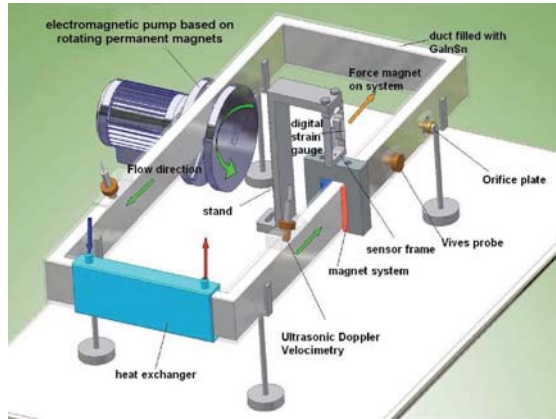


Fig. 3.9. EFCO scheme.

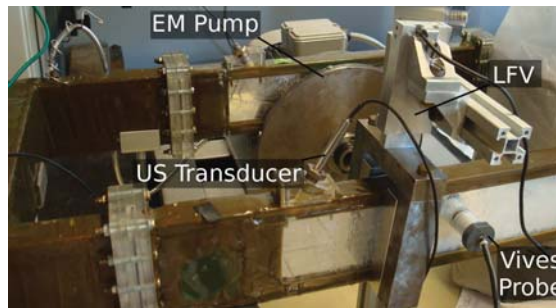


Fig. 3.10. Photography of the EFCO system.

3.11). The transducer was in direct contact with the GaInSn in order to obtain a good acoustic coupling between the transducer and the ternary alloy, the surface of the transducer was wetted with alcohol prior to its placement in the channel[§].

Six experiments for pump rotation frequencies in the range of 1-25 Hz were performed in both directions of rotation, clockwise (CW) and counter-clockwise (CCW). These give us a total of 27 pump rotation frequencies analysed. When liquid metal flows in CCW direction the US transducer is located upstream the steady magnets and therefore, a pure hydrodynamic flow with a parabolic profile is detected. On the other hand, when the flow direction is CW, the US transducer is located downstream the magnet system and therefore, the measured flow presents the M-shape velocity profile characteristic of MHD duct flows in fringing magnetic fields^[86,93–95].

3.2.2 Duct flow in a non-uniform magnetic field

Channel flows in non-uniform magnetic fields are very complex since they present a three-dimensional structure. In these flows induced electric current loops are formed in both planes parallel and transversal to the main direction of the magnetic

[§]Suggestion personally given by Dr. Oleg Andreev.

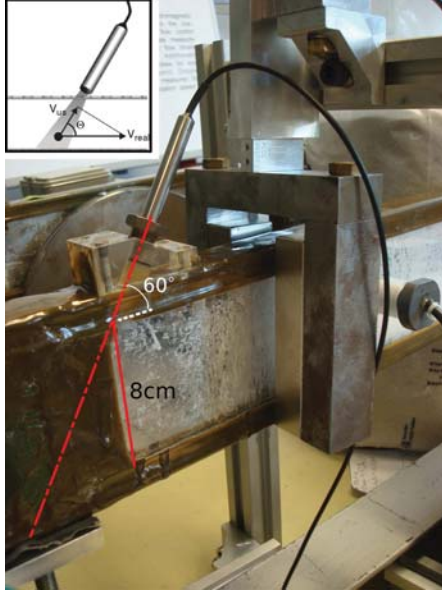


Fig. 3.11. Ultrasound transducer localization in EFCO channel.

field. In principle, distinct electric current loops can be interconnected forming very complex three-dimensional paths which interact with the applied field and originate Lorentz forces that modify the velocity field^[96,97].

In fact, most of the experimental and industrial flows of electrically conducting fluids take place in inhomogeneous magnetic. This is due to the finite size of magnets (v.e. electromagnets), that originate regions near to the magnetic poles (fringing regions) where the magnetic induction is not uniformly distributed. On the other hand, as occurs with the LFV, there are situations where the applied magnetic field region is smaller than the duct size. In addition, magnets or electromagnets have usually some imperfections on their surface as scratches, slots or projections that produce an inhomogeneous distribution. Whatever the cause, the inhomogeneity of the field will influence the flow phenomena.

Description of the flow

A brief description of the flow in a rectangular channel of constant cross-section past an inhomogeneous magnetic field, schematically shown in Figure 3.12, will be given here. We assume that the main fluid motion is in the x -direction and the main component of the non-uniform magnetic field points in z -direction. The flow in the channel passes from a negligible magnetic field region upstream the magnets to a region of maximum intensity (shaded area) and then again to a fringing region where the field drops to a negligible value in a short distance. The electromotive force $\vec{u} \times \vec{B}_0$ induces a lower voltage in the regions where the magnetic field intensity is weak and a higher voltage in the high intensity region. This voltage difference produces an electric current flowing from higher to lower intensity regions. If the channel walls are electrically insulated, electric currents

must close their paths through the fluid, as shown in figure. In the zone where the flow exits the intense magnetic field region both, the voltage difference and current circulation, are inverted. The electric currents upstream the magnet, circulate in clockwise (CW) direction and induce a magnetic field normal to the plane that points downwards while downstream the magnet currents circulate in counter-clockwise (CCW) direction and the induced magnetic field point upwards.

The duct walls confine the current paths in such a way that electric current loops are elongated in the streamwise direction, intensifying the axial components of the current density close to the lateral walls. This effect is intensified when the channel walls are electrically insulated. The axial current density components produce a y -component of the Lorentz force, $j_x B_z^0$, that points to the center of the channel at the entrance to the magnetic field region and to the walls at the exit of this region, due to the opposite current circulation described before. Additionally, the transversal y -component of the electric current density produces a Lorentz force component in the x -direction that opposes the flow with a higher strength in the central region than close to the lateral walls. These effects cause that part of the fluid is expelled towards the walls and therefore high velocities are found in these regions. As a result, M-shaped profiles are obtained due to the presence of the inhomogeneous magnetic field. The characteristics of these flows depend on the dimensionless parameters Re y Ha . Depending on the magnet's size in streamwise direction, dimensions and geometry of the duct as well as the physical properties of the fluid, M-shape profiles may change. An additional effect is that in the fringing magnetic field zones, the transversal component of the electric current density produces forces that upstream the magnet point in the same direction as the fluid flow but downstream the magnet this force opposes the flow. As a consequence, in addition to pressure drop due to viscous effects, the pressure increases at the entrance of the magnetic field region and decreases at the exit of this region.

3.2.2.1 Hydrodynamic flow upstream the magnet system

The flow upstream the magnet is characterized by a parabolic velocity profile. In this case, since the distance from the corner of the liquid metal loop to the measurement zone is small (approximately 30 cm), the flow can not be considered as fully developed. As a result, a “flattened” profile is obtained. It is important to mention that MHD effects are not responsible of such phenomenon.

Figure 3.13 shows the averaged axial velocity profiles versus the transversal y -coordinate corresponding to all the analysed pump rotation frequencies. Since the US beam direction presents an angle with respect to the axial flow direction (see Figure 3.11), the plotted velocities correspond to the projection of the measured velocities in the mean flow direction. Every profile was obtained by averaging six profiles, each one corresponding to one experiment (see for instance Figure 3.14). Although Figure 3.14 shows only the profiles for one pump rotation frequency, for all analysed frequencies the flow behaviour is similar and no significant differences exist. It is observed that the velocity increase monotonically as pump rotation frequency does. Negative values of the velocity magnitude mean that the flow is

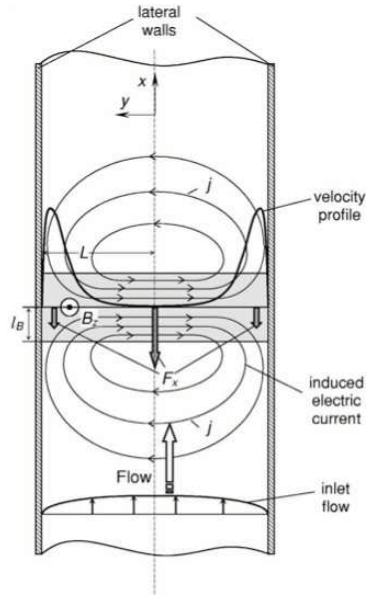
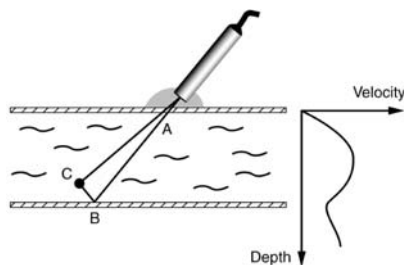


Fig. 3.12. Flow of an electrically conducting fluid through an inhomogeneous magnetic field (taken from Ref.^[86]).

towards the transducer. Figure 3.13 also shows two coloured sections close to the walls where an accurate measurement is difficult or even impossible to do. Close to the upper wall where the transducer is located (corresponding to $y = 0$), the ringing effect^{[98]§} makes impossible the measurement, while at the lower wall ($y = 80$ mm) the interface induces modifications in the velocity profiles that avoid to measure the no-slip velocity at the wall[†]. Since the flow is symmetric with respect to the central axis of the channel, the profiles in the complete flow region can be obtained by projecting the results of the upper part of the duct. It remains,

[§]Ringing effect refers to the vibration of the transducer following the emission. The depths affected by this phenomena depend on the frequency and length of the emitted burst as well as on the transducer. The saturation appearing at depths located just after the surface of the transducer is normal and can not be removed. At these depths correct measurements are not possible.

[†]The ultrasonic beam BC reflected by the far interface of the figure transforms this interface in a transmitter. The same particles contained in the liquid will backscatter a second time energy in the direction to the transducer CA.



The depth associated to the path ABC is located outside the flowing liquid. Imaginary velocity components are added to the real velocity profile. The measurement of velocities near the far interface is affected by this phenomenon. The size of the ultrasonic beam determines mainly the level of this artifact. The effect mentioned above explains why it is impossible to obtain a zero velocity value at the far wall. Taken from the UDOP Manual^[98].

however, the lack of measurements close to the walls.

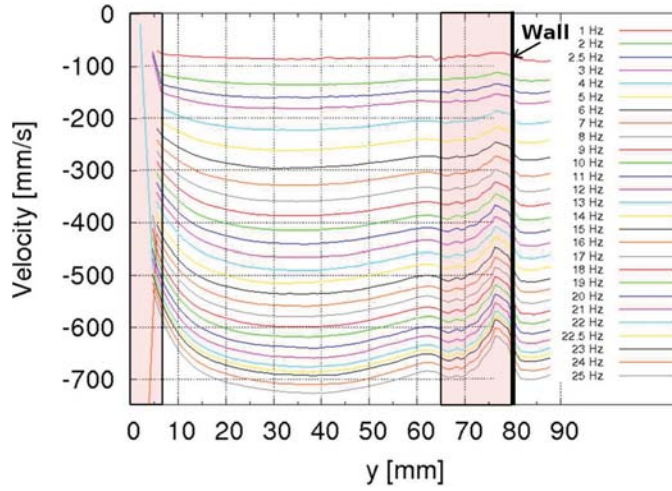


Fig. 3.13. Averaged velocity profiles for all pump rotation frequencies.

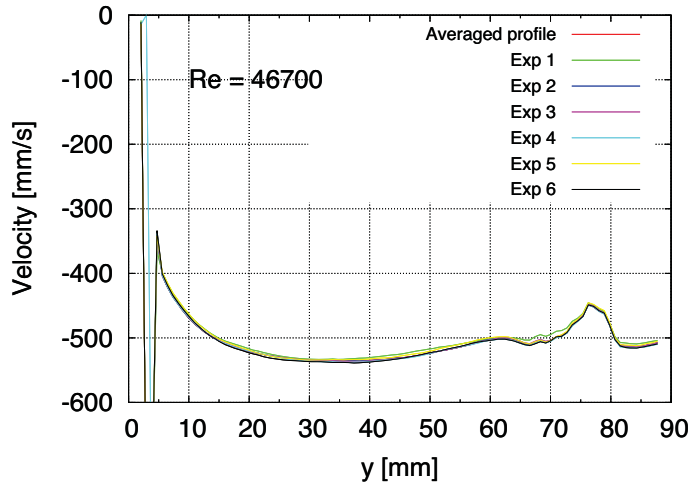


Fig. 3.14. Comparison of the averaged velocity profiles for a pump rotation frequency of 15 Hz.

Figure 3.15 shows the maximum velocity magnitude, obtained at the center of the channel, as function of the pump rotation frequency. It is observed that the increment of the velocity is not linear and apparently it tends to a saturation value for high frequencies although this is not shown in the figure.

Since these measurements can also serve as a reference for the development of the Lorentz Force Velocimeter (LFV), it is important to look for periodic patterns in the velocity profiles that can be related to the pump rotation frequency. In order to verify the existence of such patterns the Fast Fourier Transform (FFT)

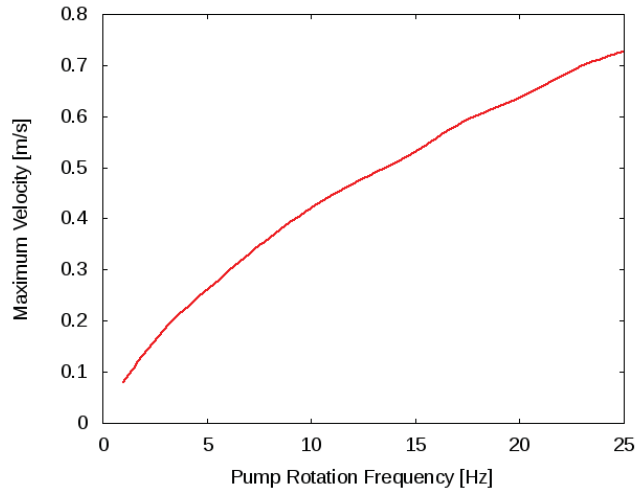


Fig. 3.15. Maximum velocity magnitude as function of the pump rotation frequency. Corresponding Reynolds number range is $7000 < Re < 65000$.

was applied to the velocity measurements taken at several penetration depths, that is, at different y -locations. Figure 3.16 shows in the first row the velocity as a function of time at two different time intervals, one at the onset of the experiment (left) and the other at the final steps of the experiment (right). In the second row, the FFT of the velocity signal is presented. This analysis shows that no periodic structure exist at any pump rotation frequency. This could be attributed to the changes in the flow direction within the loop which damp any possible periodicity in the flow.

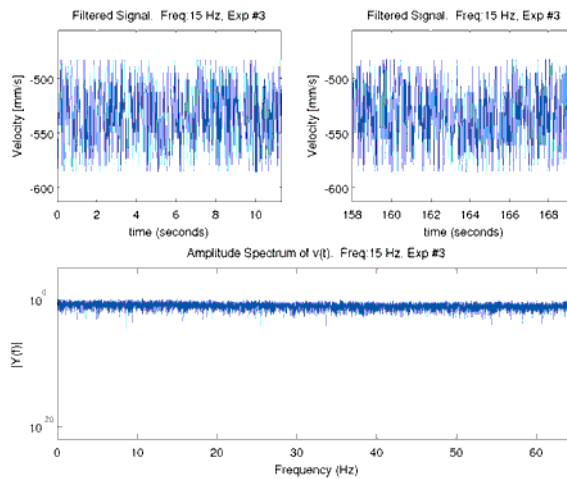


Fig. 3.16. First row: Velocity signal as function of time at the onset of the experiment (left) and at the final steps of the experiment (right). Second row: Power spectrum of the analysed velocity signal. Penetration Depth: $y = 40$ mm.

3.2.2.2 MHD flow downstream the magnet system

When the flow circulation in the loop is in the clockwise direction, the US transducer is downstream the magnets and the measured profile reflects the MHD effects. In this case the distance from the magnets to the measurement zone is around 6 cm. The averaged axial velocity profiles as a function of the y -coordinate (penetration depth) for all pump rotation frequencies are shown in Figure 3.17. The Hartmann number remained fixed in all the experiments and has the value $Ha = 160$, based on channel's width. This value is high enough for the MHD effects to be clearly manifested. In fact, the M-shape velocity profile characteristic of MHD flows in non-uniform magnetic field regions, as previously described, is clearly observed. It is also noticed that the velocity increases monotonically as the pump rotation frequency grows, just as in the CCW case. As occurs in the measurements reported in the previous section, the coloured regions marked in the figure show the penetration depths at which measurements are not reliable. This inconvenience prevents from measuring the whole profile but as in the CCW flow case, the assumption of symmetry with respect to the channel axis allows to reproduce the complete profile. It is interesting to note the large difference between the flow velocity in the center of the channel and that close to the side walls. For instance, for the highest rotation frequency (25 Hz) the allowable measured velocity in the side layers is approximately 2.6 times the velocity in the central axis.

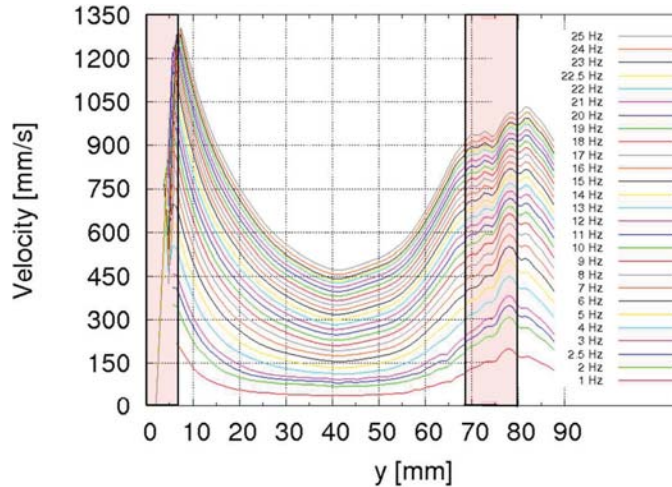


Fig. 3.17. Averaged axial velocity profiles as a function of the y -coordinate (penetration depth) for all pump rotation frequencies in the flow downstream the localized magnetic field. $Ha = 160$.

There is an additional detail that should be noted in the velocity profiles of Figure 3.17. In fact, there is a slight asymmetry in the profiles with respect to the central axis of the channel in the zone where measurements are reliable. For instance, the velocity value at $y = 20$ mm is slightly different from the value at $y = 60$ mm. In part, this is due to the following reason. Since the US transducer is not placed normally to the side wall but with a given inclination angle (see

Figure 3.11), the points of measurement close to the transducer and those close to the bottom wall, differ in approximately 4.5 cm in the main flow direction. The velocity in the more downstream position close to the bottom wall is slightly smaller due to the fact that the diameter of control volume is bigger, because of the divergence of the US beam, and fluid particles near the walls are included in computation and thus the velocity magnitude decay. Therefore, when the data taken along the beam line are projected in the transversal y -direction the difference becomes evident.

The FFT analysis was also applied to these experimental data and the results showed that no periodic flows exist, as occurs in the flow upstream the magnets.

3.2.2.3 Calculation of flow rate

The Lorentz force velocimeter mounted in the EFCO channel was expected to give information about the bulk velocity of the fluid. Through the UDV it is possible to measure the velocity along a line (the beam line, see Figure 3.19). In order to match both results it was necessary to obtain the flow rate from UDV measurements. To do this, the results from the hydrodynamic flow upstream the magnets were used and the procedure is described below.

We considered the upper half of the experimental velocity profile (the part corresponding to the wall where the US transducer is located) and dismissed the region close to the transducer where measurements are not reliable. By assuming a no-slip condition at the wall (i.e. at the transducer surface) a polynomial fit of the experimental results was used to reproduce the complete (half) profile, $v_m(y)$, as is shown in Figure 3.18.

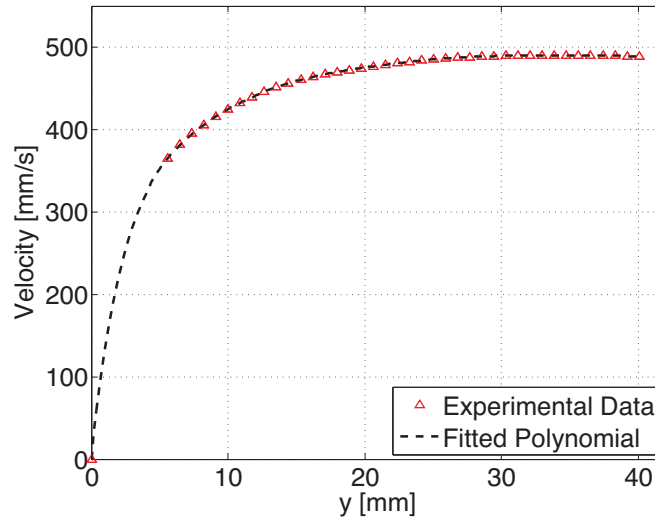


Fig. 3.18. Experimental velocity profile and polynomial fitting in half of the channel for the hydrodynamic flow upstream the magnets. Pump rotation frequency 13 Hz.

We assume that the velocity can be expressed as the product of two independent

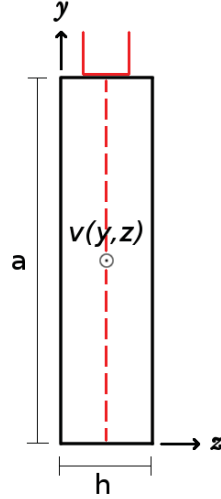


Fig. 3.19. Cross-section of the channel and characteristic dimensions. The location of the US transducer is shown in red in the upper wall and dotted line represents the US beam line.

functions, namely

$$v(y, z) = \gamma(y) f(z) \quad . \quad (3.1)$$

If we also assume that the flow has a parabolic form in y direction, we can write Eq. (3.1) as

$$v(y, z) = \gamma(y) (hz - z^2) \quad . \quad (3.2)$$

It is important to notice that Eq. (3.2) satisfy the no-slip condition at $z = 0$ and $z = h$. To determine the value of $\gamma(y)$ we have that $v(y, \frac{h}{2}) = \gamma(y)$ so

$$\gamma(y) = \frac{4v_m(y)}{h^2} \quad . \quad (3.3)$$

The volumetric flow rate can be obtained by integrating the velocity as follow

$$Q = 2 \int_0^{\frac{a}{2}} \int_0^h \frac{4}{h^2} v_m(y) (hz - z^2) dy dz \quad , \quad (3.4)$$

where the factor 2 is included in order to consider the whole channel cross-section. Finally the flow rate is

$$Q = \frac{4}{3} h \int_0^{\frac{a}{2}} v_m(y) dy \quad . \quad (3.5)$$

The mass flow rate ($\dot{m} = \rho Q$) is plotted in Figure 3.20 as function of the pump rotation frequency. The pump has a maximum mass flow rate of 2.2 kg/s at pump rotation frequency of 25 Hz. As in the case of the maximum velocity (Figure 3.15) the flow rate presents a saturation condition, although for the explored frequencies the system is far from reaching that condition. Even though these results were used

in the characterization of the EFCO channel flow, there are not reported data to compare with. LFV measurements are mainly focused on the output voltage from the strain sensor^[84,85].

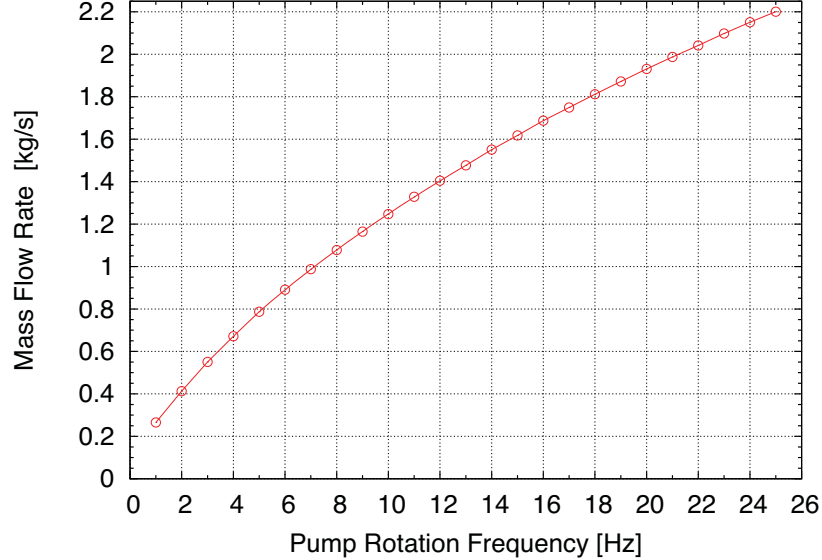


Fig. 3.20. Mass flow rate as function of pump rotation frequency.

3.3 Conclusions

In the first part of this chapter, experimental results of liquid metal flows past magnetic obstacles obtained with the UVP method were presented in two cases: a fully developed duct flow and a developing free surface flow. In the first case, different steady vortex patterns were identified as the Reynolds number (or the interaction parameter) was varied. In the second case, the evolution of the developing profiles in the wake was presented as Re varied. This study provides new experimental results about the rich dynamical behaviour of liquid metal flows past localized magnetic fields. In fact, it supplies valuable information for the development of future numerical simulations that attempt to model these complex and still not well understood flows.

In addition, characterization of liquid metal flows in the EFCO channel using the UDV technique was done. The velocity profiles were obtained for all pump rotation frequencies in both CW and CCW flow directions so that flows upstream and downstream of the magnet system were studied. The flow upstream the magnet system is a purely hydrodynamic flow with a parabolic velocity profile. In turn, the flow downstream the magnets presented the M-shape profile characteristic of MHD flows past non-uniform (fringing) magnetic fields. In both cases the velocity increases monotonically, but not linearly, as the pump rotation frequency grows. Using the hydrodynamic velocity profiles the mass flow rate was computed.

Results show that the pump can develop up to 2 kg/s at 25 Hz; and this mass flow rate can be increased if a motor of higher rpm's is used. Initially it was thought that periodic patterns related to the pump rotation frequency could exist which lead to perform a FFT analysis of the experimental data. Results showed that our assumption was incorrect and no periodic patterns were observed. The experimental analysis performed in the EFCO channel is relevant for the calibration and characterisation of the LFV system which at present is being developed at the Ilmenau University of Technology.

Chapter 4

Electromagnetic stirring with localized rotating magnetic field

This chapter addresses experimentally the electromagnetic stirring of a liquid metal. In order to put in perspective this application within the context of Electromagnetic Processing of Materials, an introductory section is offered. The analysed problem consists in the flow of a shallow liquid metal layer (GaInSn) driven by an array of small rotating permanent magnets (12.7 cm diameter) located at the bottom of a cylindrical plexiglas container with a diameter of 203.2 mm. The fluid layer is 13 mm thick and the maximum analysed rotation frequency is 7 Hz. The explored magnet arrays vary from one single magnet up to 5 magnets eccentrically located at a distance of 29.1 mm or 42.2 mm from the rotation axis. The radial velocity component was recorded using Ultrasound Doppler Velocimetry (UDV) and analysed through the Fast Fourier Transform. The flow is also characterized by visualizing the free surface oscillations. A three dimensional flow structure which is consistent with the observed features is proposed.

4.1 Introduction

As explained in chapter 1, Electromagnetic processing of materials (EMP) is the application of the electromagnetic forces to material processing^[99,100]. There are records that metals were first produced more than 6000 years ago! *The branch of engineering concerned with the chemical reactions involved in the processes by which metals are produced and the chemical, physical, and mechanical behavior of metallic materials*^[101] is metallurgy. It is known that electric energy has been used for many year in metallurgy for melt and refine metal or alloys, for example Sir William Siemens demonstrated the electric arc furnace in 1879^[102]. The application of electromagnetic forces to metallurgic processes occurs in 1920-1930^[29], but it was without the fundamental understanding of the involved phenomena. We can say that the development of MHD and metallurgy (using electric energy) followed separated ways. It was until 1978 that in Grenoble, France the “Mag-

netodynamique des Liquides-Applications à la Métallurgie” (MADYLAM[§]) Joint Research Program made efforts to bring these two big areas together, and that is accepted as the beginning of EPM as a science. The MHD theory was used to solve problems in processing conductive materials as molten metals or salts. For example, new non-intrusive measurement techniques^[104], as Ultrasound Doppler Velocimetry^[81,105–107] (UDV) or Lorentz Force Velocimetry^[35,36,84] (LFV), has been developed for the characterization of liquid metal flows. This is just an example among a wide variety applications^[108].

The actual requirements of high-grade materials lead to an increase in energy consumption. This creates the necessity of new efficient technologies. The most of these technologies use electric energy as the main source to achieve it because its high density, cleanliness and controllability. Electric energy can be applied directly to the materials in order to melt them by Joule heating. It can be done through an electric arc (by electrodes separated from the metal) which has the disadvantage of need higher energy as the separation increase, or by direct contact of the electrode with the metal. This latter requires materials with high melting point and electrical conductivity and resistivity to very corrosive environments. Such materials may result very expensive. The other way is using electric currents induced by moving magnetic fields, Ampère’s law. The main advantage of this method is its non intrusive nature. Induced currents can be used also for melt metals, by Joule heating, or to stir^[109], when the electric currents interact with the magnetic field that induce them giving rise to the Lorentz force that modifies the flow dynamics.

Due to the wide range of applications, different combinations of magnetic and electric fields can be done. Asai^[29] classified process by the imposition of magnetic fields, the imposition of electric currents, or the imposition of both simultaneously, considering AC, DC, static and alternating magnetic fields. It is important to say that in stirring and pumping applications, that concerns us, DC magnetic fields and AC magnetic fields at frequencies smaller than 60 Hz are used. Higher frequencies, up to several MHz, are mainly used to levitate, melt, among others.

In “electrode-free” applications in EPM, direct and alternating current can be used, but it is this latter the most suitable. An example of application of static magnetic field produced by a direct current is in the casting of molten metals^[110], where suppression of undesirable motion (liquid metal jets that feed casting molds) is needed. In this case, induced currents lead to ohmic heating. As the thermal energy increases, the kinetic energy decreases, namely, there is deceleration of the fluid. In the other hand, injecting an AC through specially located arrays of coils results in different magnetic fields. Depending on the position in which coils are arranged and/or the way in which current is injected we may obtain a Travelling Magnetic Field (TMF) or Rotating Magnetic Field (RMF) or a combination of

[§]The MADYLAM Laboratory was officially founded in 1986, and its name changed to EPM (Electromagnetic Processing of Materials) in 1994. In 2007, the EPM laboratory merged with other laboratories, becoming one of the six research groups of the new SIMAP (Science et Ingénierie des MATériaux et Procédés) research division^[103].

both. TMF^[111,112] refers to magnetic fields that move in a straight path and is produced by applying out-of-phase AC currents to coils arranged vertically^[113–116], one upon the other, or horizontally^[117,118], one next to the other. In the other hand, RMFs are those fields that, as its name suggest, follows circular paths. In this case the principal magnetic field component produced is the radial^[119–125], but the azimuthal (transversal) component has been also investigated^[126,127]. This latter is referred as transversal rotation magnetic field or TRMF. Wherever the case, they are widely used for study the heat/mass transfer during crystal growth^[114,119,128,129] and solidification of metals and alloys^[116,122,130–134] among others. In all these application the main aim is to homogenize the distribution of all alloy components in the melt, as well as its temperature. For the growth of single crystals, these techniques improve the growth process^[135]. Studies concerning two-phase flows has been also developed because its high importance in industry. In some cases gas is injected directly into the melt to promote mixing or act as a catalyst^[115]. It was found that the use of TMF promotes unsteady motions leading to an intensification of transport processes in the melt and enhanced mixing efficiencies. The influence of the magnetic field on the bubbles size, shape and distribution has been also studied experimentally. It shows that the application of TRMF to a conducting fluid leads to the decrease of bubble size with the increasing of the dimensionless Hartman number^[136].

For the experimental analysis of applications using TMF and/or RMF in EPM, several laboratory models, as the MULTIMAG built in Dresden, Germany, have been developed^[137,138]. The analysis of such models, as well as industry applications, has been made experimental^[121,133,139], numerical^[109,119,131,140,141] and analytically^[142,143]. Numerical and analytical results show that the steady state flow produced by a TMF has a mono-cellular form. Namely, in a cylindrical container if the TMF moves downwards, the fluid will go down near the walls and will rise in the center of the channel^[111] forming a vortex ring. In some sense, the effect of a TMF on the flow is analogue to the effect of moving a wall, in this case, the cylinder. In this cylindrical configuration, it was shown that the flow is quite sensitive to a shift between the axes of the magnetic field and the fluid column^[113]. A shift of 1% of the cylinder's diameter may eliminate the well know toroidal flow structure. In the other hand, the use of RMF may lead to the apparition of Taylor-Görtler vortices^[128,130,133,139,144]. These vortices that appear in concave surfaces are the manifestation of instabilities in the side boundary layer and promote the turbulence in the flow. The most of the experiments were carried out in cylindrical configurations where different aspect ratios has been analysed^[144], but rectangular geometries have been also investigated^[117,118,134,145]. Additionally, it was demonstrated numerically and experimentally the great influence of the boundary condition, specifically of the free surface, on the flow^[123,146].

As mentioned, magnetic fields are used during the solidification process. In these cases, the homogeneity in the distribution of elements in the melt plays an important role in the physical and chemical properties of the alloy. During solidification, segregation of elements occurs. Segregation is the conglomeration

of elements at the interfaces, namely free surface or the walls, and may occur for several reasons. A way to avoid it is using pulsed magnetic fields^[128,133] and the understanding of spin-up flows is very important. We refer to spin-up flow to the transient flow produced by an increment in the velocity of a fluid initially at rest or in steady state. In our case this increment in velocity is induced by a magnetic field. Experimental and numerical^[139,147–149] results show that the flow first forms the Taylor-Görtler vortices and then evolves to the shading of vortices. These structures avoid segregation at the boundary layers by throwing elements from the interfaces to the center of the container, enhancing the mixing process.

The main drawback of magnetic fields produced by injection of AC or DC in coils is its high consumption of electric energy. For example, for the United States, aluminum production consumes approximately 2% of the total industrial energy used^[150]. This can be avoided by using magnetic fields generated by compact and efficient magnet structures requiring no continuous expenditure of energy^[151]. The resulting magnetic field can be static or variable and uniform or non-uniform. Permanent magnets can be fully competitive with electromagnets for applications in which magnetic fields are up to 2 T, and fields as high as 5 T can be produced in a small volume^[152]. The main disadvantages are that permanent magnets can not give fields with a rapid spatial variation and their limited temperature operations. New technologies in material science have allowed the development of magnets that can work at rather high temperatures^[151,153,154] without loss of their properties. The improvement of rare-earth transition-metal permanent magnets, mainly based on Nd or Sm, is still in progress and their market is expanding. Magnets that can operate up to 500°C^[155,156] have been developed. The use of arrays of magnets in industry application has been barely investigated^[157–159] but their usage can be incremented by the development of new technologies.

4.2 Experimental setup

The importance of usage of permanent magnets in industrial applications lead us to develop an experimental device to investigate the influence of different magnet arrays on the flow in cylindrical configurations. The experimental setup consists in a 8 *in* outer diameter cylinder, made of a 6 mm thick acrylic, filled with the ternary alloy GaInSn up to a height $H = 13$ mm, as shown in Figure 4.1. In Table 3.1 (Section 3.1) are listed the physical properties of the GaInSn alloy. Below the cylinder an array of up to 5 Neodymium magnets (0.5" diameter) at three different distances from the rotation axis can be placed in a supporting base (see Figure 4.2). Unless another thing is specified, the magnets are located equidistantly from its neighbours. The rotation radii are 29.1, 42.2 and 55.3 mm, but in present work just the first two were analysed. The minimum distance between the axis of equidistant adjacent magnets is approximately three times its diameter, namely 35 mm, when 5 magnets are located at 29.1 mm for rotation axis. Considering the fast decay of the magnetic field with distance, see Figure 4.3, influence of magnets on its neighbours can be neglected and then we may

disregard the orientation of magnets. The supporting base is attached to a 4 *in* diameter synchronous pulley and mounted over a bearing. This subsystem is coupled by a timing belt to a 1 *in* synchronous pulley mounted in a motor whose maximum rotation frequency is 29.17 Hz. Usage of synchronous pulleys and timing belts ensures a linear rotation frequency relation between pulleys. Under this configuration, the rotation frequencies of the magnets ranges from 0.4[§] to 7.3 Hz, but different frequency ranges can be reached by a proper selection of pulley diameters. Even that in all cases presented here the rotation is in clockwise direction, rotation in counterclockwise direction can be easily obtained by changing polarity in the motor. The upper surface of the magnets is separated a distance of 7 mm from the bottom of the GaInSn layer so the vertical magnetic field is 0.065 T at this point (see Figure 4.3). In order to diminish the oxidation rate of the GaInSn, a 4 mm layer of HCl^{4%V} solution was poured above it[†].

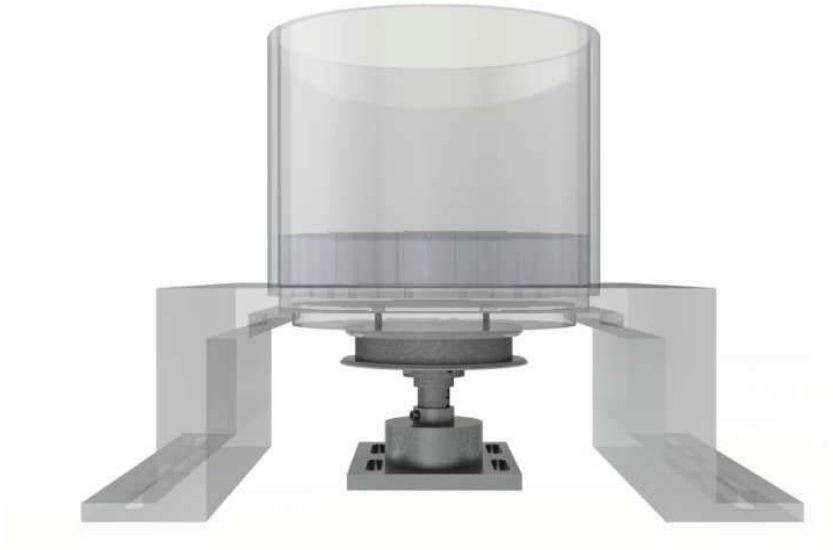


Fig. 4.1. Magnetic stirrer in cylindrical configuration.

Characterization of the flow was performed by the Ultrasound Doppler Velocimetry (UDV) technique. The ultrasound transducer (TR0805XX) was placed outside the cylinder and its axis points towards the center of the cylinder, that is to say, its surface is perpendicular to the container. The axis of the transducer is at a height of 5 mm from the bottom of the GaInSn layer. Due to the divergence of the acoustic beam, the control volumes can be considered as small cylindrical slices that increase in diameter as we move away from the transducer. The TR0805XX transducer has a divergence angle of 1.21° ^[80], so the diameter near the transducer

[§]The minimum frequency is not zero because the system must overcome the friction forces.

[†]Isopropilic alcohol was also tested, but it shows a higher evaporation rate than the HCl solution and after a long exposure of the the acrylic to the alcohol turns it brittle. Additionally, the produced microfractures in the wall propagates in vertical direction and affect the UDV.

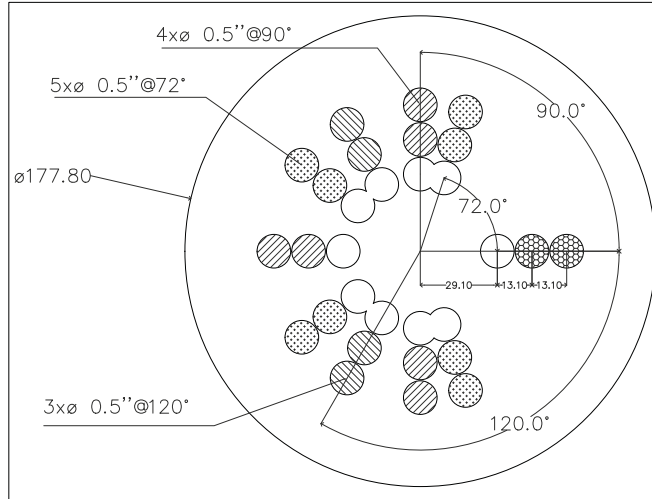


Fig. 4.2. Diagram of the support base for $\frac{1}{2}$ in diameter $\frac{1}{4}$ in height magnets. 1-5 magnets can be equidistant placed at three distances from the rotation axis (29.1, 42.2 and 55.3 mm). The base is 3 mm height and has a diameter of 7 in.

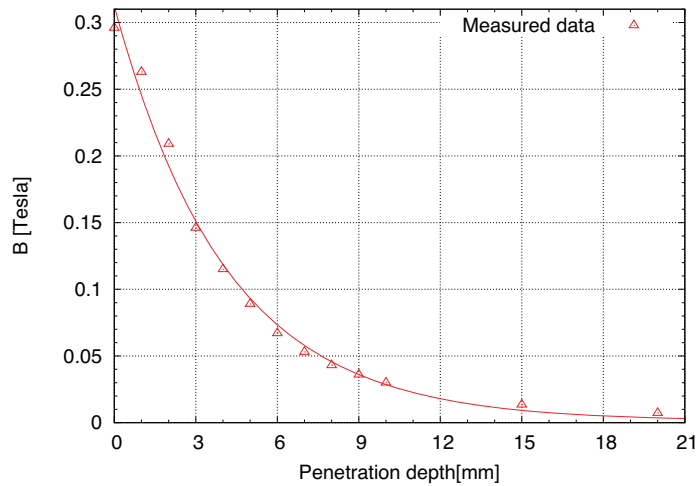


Fig. 4.3. Vertical magnetic field intensity as function of the penetration depth measured at the center of the $\frac{1}{2}$ in diameter magnet.

is less than 3 mm (in the so called *near field*) and at a distance of 200 mm the diameter of the control volume grows up to 7.5 mm. This means that at in the neighbourhood of the transducer the control volume is one fourth of the GaInSn layer while in the opposite side of the cylinder it is more than the half of the height.

We have to keep this in mind in the analysis of the results because far from the transducer the velocity profile will be “smoothed” due to the fact that regions close to interfaces will be included in these bigger control volumes.

4.3 Results

4.3.1 Methodology

The data analysis is as follows. From the ultrasound velocimeter we obtain the data (we are interested in velocity but other quantities can be easily taken) as function of time and at different positions, namely we get $v_{USBeam}(z, t)$. Here $USBeam$ refers to direction in which the velocity component is measured, namely the axis of the emitting transducer, and z to the penetration depth in the beam direction. This latter must not be confused with the coordinate z of the cylindrical coordinate system. Under the described experimental setup, the measured velocity corresponds to the radial component of velocity. The visualization of the velocity obtained shows the repetition of patterns. Additionally, it was observed that under certain conditions oscillation of the free surface appears. In order to know the characteristic frequencies of such phenomena the analysis by Fast Fourier Transform (FFT) was applied to all measured points. With these results we were able to find not only the characteristic frequencies, but also the position at which such patterns occurs.

On the other hand, due to the high reflecting properties of the free surface of the liquid metal it was possible to indirectly record it. It was done at magnet rotation frequencies at which free surface oscillation was observed. The video was then decomposed in a series of images in RGB[§] format and then all the images converted to grayscale intensity images (see Figure 4.16(a) and (b)). Transformation was done using the next relation $I = 0.2989 R + 0.5870 G + 0.1140 B$. Several points in the figure was picked and its grayscale intensity I (values ranges from 0 to 256) was obtained as function of time. Now we have $I_i(t)$, where i represents the point studied. FFT analysis is then applied to each selected points and the characteristic frequencies obtained.

Finally, the frequencies obtained by both analysis were compared.

4.3.2 UDV analysis

As mentioned in the methodology, the analysed variable was the velocity. A screenshot of the velocity profile obtained from the UDOP software is shown in Figure 4.4 (a proposed flow pattern will be given in Section 4.3.2.1). In this plot, the fluid velocity along the ultrasound beam u_{USBeam} is shown as function of penetration depth and time. The magnitude and direction of the velocity is given by the

[§]RGB is a color model in which the primary colors Red, Green, and Blue are added together to reproduce a broad array of colors. Mathematically is expressed as a $n \times m \times 3$ array, where n and m are the image size in pixels and the latter dimension corresponds to the color layers (red, green and blue). The dimensions of analysed RGB images were $1900 \times 901 \times 3$ and when converted to a grayscale image $1900 \times 901 \times 1$.

color, *blue* positive and *red* negative. By definition the fluid that moves towards the transducer is negative while when it moves away it is positive^[98]. With this in mind a pattern in the flow can be observed, namely, at one time the flow goes to the center of the cylinder (strips blue and red when seen from the transducer, always located at $z = 0$) and one time latter the fluid is driven to the cylinder wall (strips red and blue). In this figure we observe that close to the interfaces (before 20 mm and around 200 mm) measurements are not possible because difficulties described in Section 3.2.2.1.

In order to determine the characteristic frequency of such pattern, FFT analysis was applied to every measured point (commonly named gate). Figure 4.5 shows the maximum power spectra value of all the analysed depths for all magnet rotation frequencies for the five experiments performed with two magnets located at 42.2 mm from the rotation axis rotating at a frequency of 1.75 Hz. Comparison plots for other rotation frequencies and magnets arrays have the same behaviour, so we can say that reproducibility exist in our experiments. It is important to mention that experiments #4 and #5 from Figure 4.5 were performed without the HCl solution layer. We observe that this layer does not affect significantly the dynamics of the flow. Several experiments with different configurations were carried out with and without the HCl solution layer and its comparison shows the same result. It was decided that the HCl solution layer was held in the most of the experiments just to diminish as much as possible the oxidation ratio of the ternary alloy. We must remark that the maximum measurable frequency is given by the half of the sampling frequency, Nyquist sampling theorem, and depending on the experimental conditions it ranges from 6.5 - 11 Hz approximately .

All the experiments show patterns whose frequencies always are smaller than 0.6 Hz (see also Figures 4.7 and 4.8). In addition, it was observed that under certain parameters the system get into resonance and its surface becomes to oscillate. The frequency of such oscillation is higher that 1 Hz. In order to distinguish all the characteristic frequencies of the flow, the plots were divided in two sections: one from 0 to 0.65 Hz or less, where the flow structure frequency and its harmonics appear, and from 0.65 to 7-9, where free surface oscillation (FSO) frequency resides in. In Figure 4.5 the peak in the second section of the plot (frequencies $\gtrsim 0.5$, in this case) represents the free surface oscillation frequency, while the second peak in the first section corresponds to the harmonic of the flow structure frequency. As we are only showing the maximum of the power spectrum, it must be pointed out that the flow frequency is not observed in the center of the channel ($\sim 80 - 120$ mm) and close to the cylinder walls ($\sim 0-30$ mm and $170-200$ mm); while the FSO frequency is observed all along the measured line because a back and forward movement is produced.

Figure 4.6 shows the characteristic frequency of the flow and the free surface oscillation frequency (if exist) for all experiments performed with one magnet. We notice that the computed frequencies of all experiments have a good agreement and that the flow frequency increase monotonically, but not linearly, with the magnet rotation frequency (MRF). A more interesting analysis can be done to

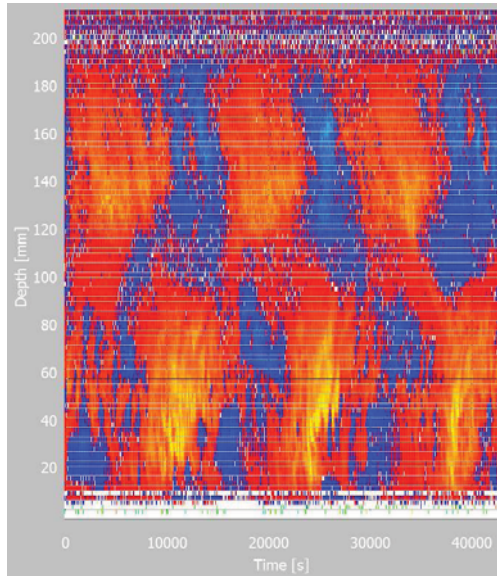


Fig. 4.4. Velocity as function of penetration depth and time for one magnet rotating at 2.9 Hz. Color scale represents the magnitude of the velocity, *blue* positive and *red* negative. Screenshot of the data obtained from UDOP software. Given time is in ms.

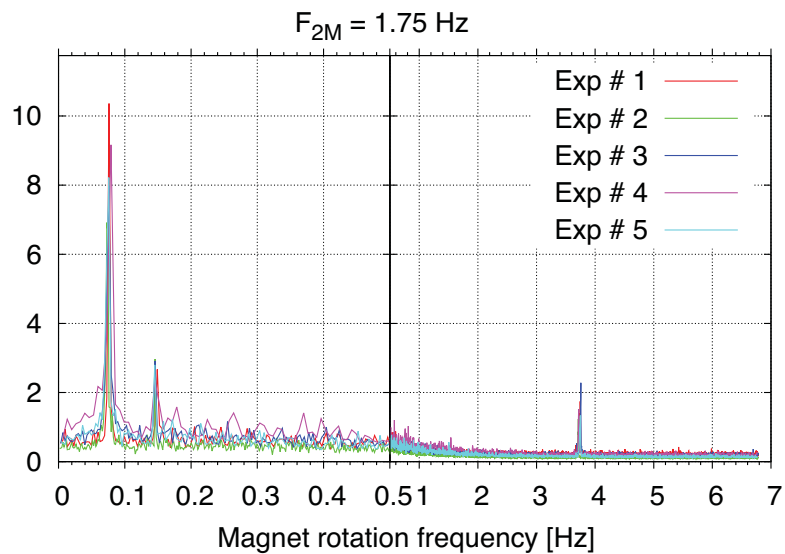


Fig. 4.5. Maximums of power spectra for the experiments realized with two magnets rotating at a frequency of 1.75 Hz.

the oscillation frequencies. FSO occurs only at well defined rotation frequency ranges, in this case, from 0.85-1 Hz, close to 1.75 Hz and from 2.7-2.9 Hz. In first and last ranges the surface oscillation occurs roughly to the same magnet rotation frequency. For a magnet rotation frequency of 1.75 Hz a FSO frequency of 3.7 Hz

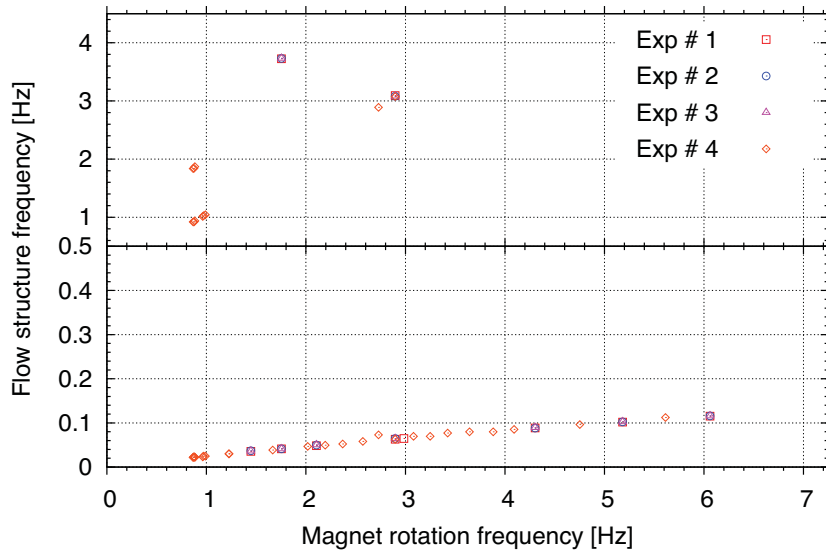


Fig. 4.6. Frequencies map for all experiments performed with an array of 1 Magnet rotating at 42.2 mm from the axis.

exist, which we can easily relates to the MRF as twice its value. In any case FSO frequency is closely related to the MRF.

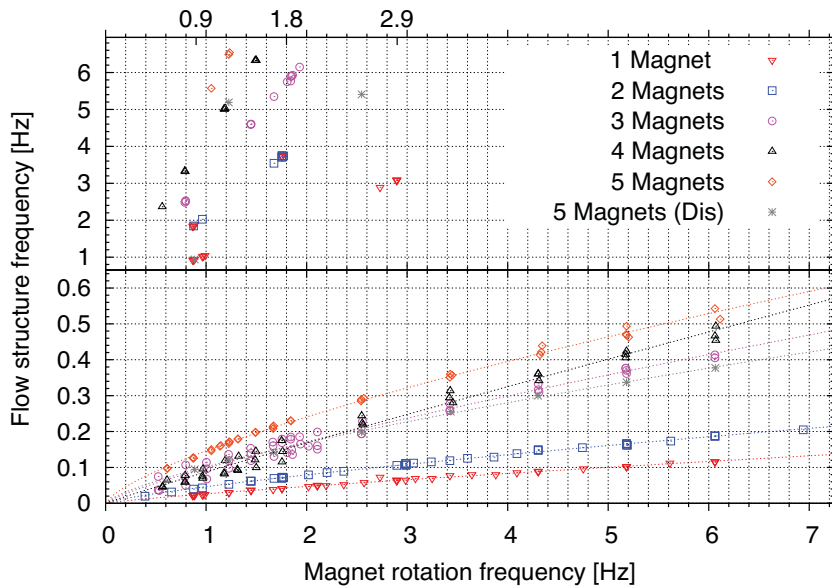


Fig. 4.7. Frequencies map comparison for all magnets arrays rotating at 42.2 mm from the axis.

Now we compare the obtained frequencies of all experiments with all magnets

arrays when magnets are placed at 42.2 mm from axis in Figure 4.7 and at 29.1 mm in Figure 4.8. In Figure 4.7 we observe an increase in the characteristic frequencies as the magnet rotation speed is increased. We notice that as we increase the number of magnets the flow frequency does not grow linearly. This can be seen by defining the *normalized frequency* as the flow frequency divided by the number of magnets. For a MRF of 6.06 Hz and one magnet the normalized frequency is 0.115 Hz and it decrease for two magnets to 0.093 Hz. This value increases to 0.136 Hz when three magnets are used and diminish up to 0.105 Hz for five magnets. Then for a two magnets array we have a local minimum and for three magnets a maximum. This latter can be considered as a global maximum due to the fact that if we increase the number of magnets and all of them have the same orientation, the distribution of the total magnetic field will tend to diminish the inhomogeneities in the direction of rotation of the array (the resulting magnetic field will tend to that produced by a ring shaped magnet) and eventually no movement will be produced. We should remember that the maximum number of magnets is determined by the shape and size of the magnet, the array and the rotation radius, so experimentally we will always induce movement in the liquid metal. Finally, if we use a disordered array of magnets the resulting flow frequencies will be smaller than the corresponding values when ordered, and as the magnets are close to others the resulting effect will be alike the produced by a smaller number of magnets, in the presented case it is equivalent to use three magnets. Taking in Figure 4.2 as reference holes the honeycomb hatched ones and enumerating it in counter-clock wise direction from 1 to 10, in used disordered array, magnets were placed at positions 2, 3, 4, 5 and 6 with unsorted pole orientation. When we look at the FSO frequencies produced this array we observe that depending on the MRF the free surface oscillates at frequencies that are in the tendency lines of other arrays, in this case arrays of 1, 2 or 4 magnets. A deeper analysis of the FSO frequencies will be given later.

As pointed before, Figure 4.8 compares the frequencies of all experiments with all magnets array rotating at 29.1 mm from axis. At first glance we note the change in behaviour of the flow as we increase the MRF. Now the flow pattern, that will be described in Section 4.3.2.1, change and decrease its frequency in one order of magnitude. We observe in the experiment (will be presented in Section 4.3.3) that the flow becomes unstable and a single vortex is formed. Moreover, this vortex follows a circular loop whose center corresponds to the rotation axis of the magnets array. The velocity of such translation increases with the MRF and the maximum frequency obtained was approximately 0.7 Hz for 5 magnets rotation at 6.06 Hz. If we look at the UDV given profile (equivalent to that shown in Figure 4.4) we now have alternate stripes of one color which means that at one instant all the fluid goes in one direction and some time after (a displacement of 180° of the vortex) the fluid goes in opposite direction. We observe that either the number of magnets or the MRF grow, the threshold of the vortex formation appears at smaller frequencies. For example with one magnet it appears at 4.3 Hz while for 5 magnets it does at 1.2 Hz. These values represent the frequency

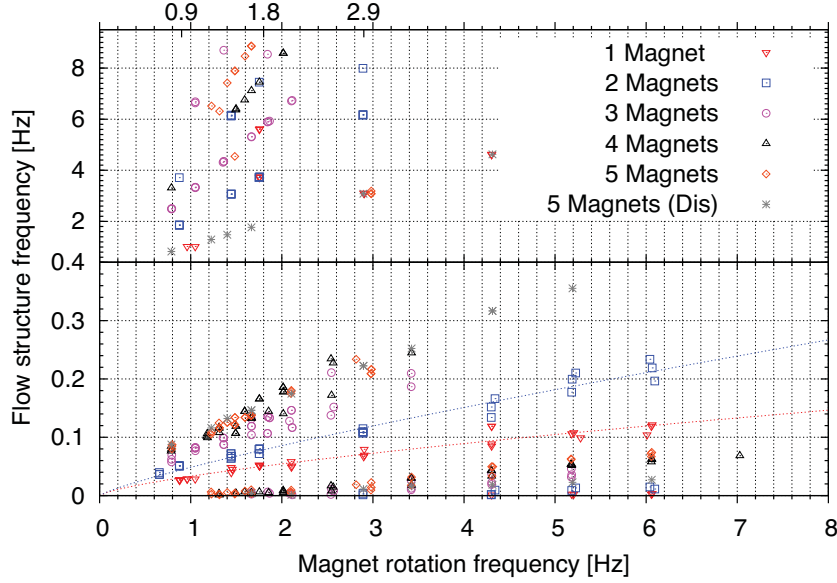


Fig. 4.8. Frequencies map comparison for all magnets arrays rotating at 29.1 mm from the axis.

at which the vortex formation appears and here both structures coexist. At the studied frequencies just for 3 to 5 magnets arrays it was possible to obtain just the vortex structure flow for MRF higher than 3.4 Hz for three magnets and 3 Hz for 5 Hz. We can see this in Figure 4.9 where \times represents the points at which single vortex appears and \odot represents the “Leaves-like” pattern points (Section 4.3.2.1). The zone between the dotted lines represents the threshold area. This is only valid for ordered arrays of magnets. Disordered arrays may have a completely different behaviour, as confirmed in Figures 4.7 and 4.8. Despite these interesting results, study of disordered arrays was out of the scope of this work and no further experiments were performed. In this case, magnets were placed at positions 3,5,6,7 and 9 with unsorted pole orientation. We just have to mention that the FSO frequencies obtained for the five magnets disordered array rotating at 29.1 mm from axis fit to a line with a slope of one fifth of the of m .

Figure 4.10 show the normalized FSO frequency as function of the magnet rotation frequency. We observe that the most of the normalized frequencies corresponding to ordered arrays in both cases, 29.1 and 42.2 mm, drop to a linear fitting with a slope $m = 1.06$. A further mention about this slope will be made in Section 4.3.3.1. Additionally, for 42.2 mm only one harmonic appears when one magnets is used, but in the other case appear two harmonics: with one magnets two harmonics and with up to three magnets one harmonic. It is important to notice that as the number of magnets is increased the maximum MRF at which FSO occurs decrease.

So, in general we can say that as MRF is increased, the characteristic flow frequencies grows too. In both analysed cases the flows frequencies (smaller than

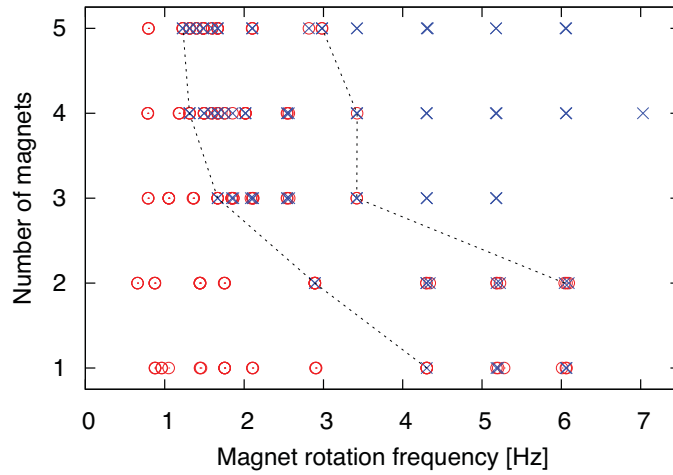


Fig. 4.9. Flow structure threshold for magnets located at 29.1 mm from the axis. \times represents the single vortex pattern and \odot Leaves-like pattern.

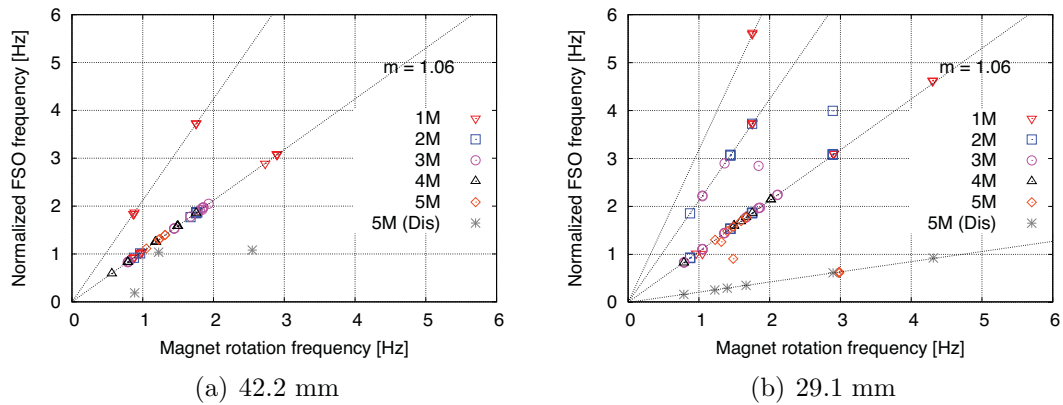


Fig. 4.10. Normalized free surface oscillation (FSO) as function of magnet rotation frequency. Linear fitting lines corresponding to $y = mx$, $y = 2mx$ and in (b) $y = 3mx$.

0.65 Hz) do not grows linearly as does the most of the FSO frequencies. In the case of 29.1 mm there is a threshold in which flow pattern change to a translating vortex flow. The frequency at which this threshold begins decrease as the number of magnets is increased. And from Figures 4.10, we may conclude that the most of experiments in which FSO occurs have a linear behaviour in the sense that when its normalized frequency is compared, they fit to the same curve.

4.3.2.1 Proposed flow patterns

Figure 4.4 shows the radial component of velocity as function of time and penetration depth, namely $u_r(z, t)$. This measurement was obtained by means of a fixed transducer located at the outer wall cylinder pointing towards its axis. Even that in figure is not shown the velocity for all the analysed time (all experiments were around 7-12 min long), the pattern repeats all time, after reaching its developed state. In other words, the flow is periodic in time and in space. With this in mind, we could imagine that we have a stationary flow and that now we move the transducer all along the outer circumference of the cylinder. In this case, the velocity depends on the radius r and on the angle θ , namely $u_r(r, \theta)$. The proposed flow in the measuring plane (normal to the cylinder axis) is obtained by passing the velocity from a spatio-temporal domain $u_r(z, t)$ to a 2D domain $u_r(r, \theta)$. The transformation of z to r is straightforward since the penetration depth corresponds to the cylinder diameter. In order to change the time t to angle units θ it is necessary to define the characteristic flow frequency which will give us the velocity of movement of the transducer along the cylinder wall. The characteristic frequencies have been already defined in Figures 4.7 and 4.8. Next we plotted several configurations that could give us the obtained velocity profile. In Figure 4.11(a) we show the configuration with four pairs of vortices. We obtain a “leaves-like” pattern. In the center of this pattern a saddle point exist. In the fully developed state the whole liquid metal rotates, and by rotation difference we expect that the Ekman pumping^[83,160] effect exists. This effect agree well with our proposed model because is this saddle point by which the fluid goes up or down forming a swirling column in Ekman pumping.

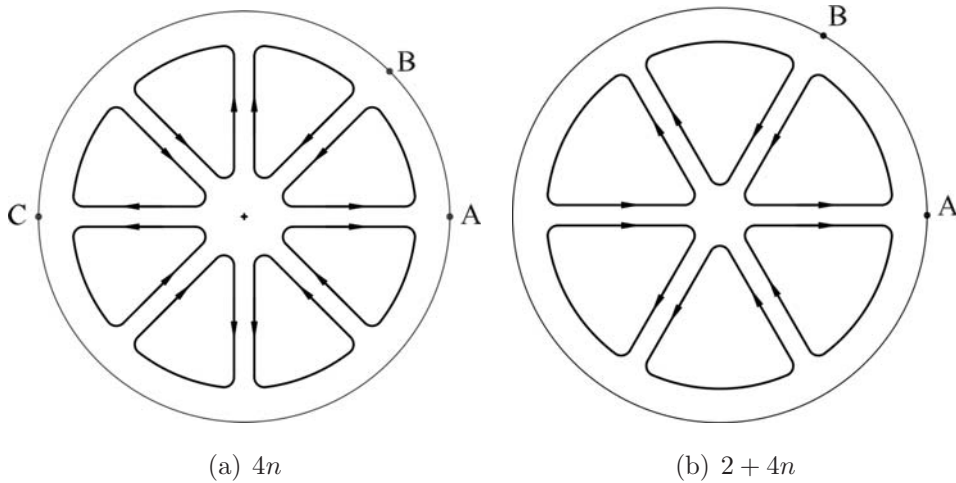


Fig. 4.11. Proposed flow structure patterns.

As mentioned before, several arrays were analysed but only those shown in Figure 4.11 agree with our measurements. In Figure 4.11(a) a pattern flow with eight vortices is shown. If we place the transducer in point A we observe that the flow goes towards the walls, equivalent to a strip red-blue in Figure 4.4. A half of

period after, at point B, the flow goes to the center of the cylinder that corresponds to a blue-red strip. If we continue with the analysis up to point C, we observe that the profile will be equal to that obtained at point A. In a more general way we can say that those flows with $4n$ vortices agree with in all experiments performed with magnets at 42.2 mm from axis and those before the threshold beginning in experiments with magnets at 29.1 mm.

Figure 4.11(b) shows a pattern flow with six vortices. If we place the transducer at point A we will observe that the fluid moves toward the transducer, that in the UDOP software will show as a red strip. In point B, the fluid moves away from the transducer, whose equivalent is a blue strip. This pattern could fit to the experimental measurements corresponding to a single translating vortex at the beginning of its formation. In fact what we purpose is that at the very beginning of the motion a $4n$ pattern is formed, it change to a $2+4n$ pattern in the threshold zone and finally all vortices collapse into one bigger that eventually becomes eccentric. It is important to mention that the described patterns may agree with experimental data, other patterns can agree also. In order to clarify this point, further analysis must be done.

4.3.2.2 Velocity fluctuations

In order to have a better understanding of the flow it is important to define the places at which the energy is been transferred. To achieve this we use the *energy fluctuations* equation

$$\delta E = \langle f^2 - \langle f \rangle^2 \rangle \quad (4.1)$$

where f is the variable which we want to analyse, in our case it is the velocity. Then Eq. (4.1) takes the form of

$$\delta E = \langle u_r^2 - \langle u_r \rangle^2 \rangle \quad (4.2)$$

The maximum or peak of δE give us the places where momentum transfer is mainly occurring. The higher the magnitude of such quantity the higher the intensity of momentum transfer. We have to remember that the rotation axis of the system is located at a penetration depth of approximately 105 mm. Thus in the 42.2 mm case, magnets will pass at 62 mm and 147 mm, while in the 29.1 mm case it will do at 75 mm and 134 mm. Other important thing to have in mind is the divergence of the ultrasound beam that will produce control volumes big enough, at penetration depth higher than 100 mm, to include near to interfaces zones, effect previously described. Therefore the resulting profile will be smoothed by this effect. In this section analysis is mainly based on the first half of the velocity fluctuations profile.

Figure 4.12 shows the obtained and normalized velocity fluctuations profiles for an array of one magnet. From the obtained velocity fluctuation profile, Figure 4.12(a), we observe that as we increase the rotation frequency of the magnets array there is a higher transfer of momentum. We see that the locations at which the center of the magnets pass correspond to a local minimum of the profile. Then

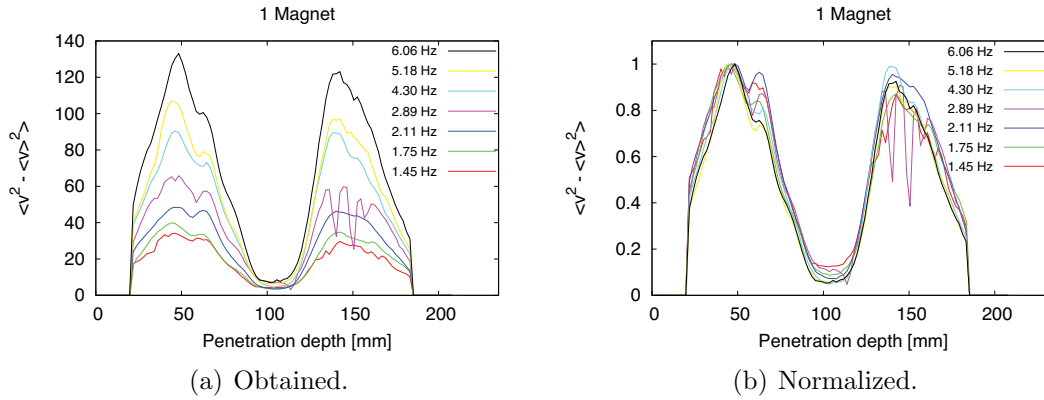


Fig. 4.12. Velocity fluctuation profiles for all magnet rotation frequencies when one magnet is used. $r = 42$ mm.

the locations at which the energy is transferred at a higher intensity is at the sides of the magnets and not at the center as could be assumed. The reason is that when a magnet pass, the fluid is thrown to it sides since the magnet acts as an obstacle^[30,31,33]. In the normalized profile, Figure 4.12(b), we observe that the distribution of momentum transfer does not change under the analysed conditions. This behaviour is modified if the number of magnets is increased. In Figure 4.13 the normalized fluctuations velocity profiles are shown for an array of four magnets for all MRFs studied. We observe that for a higher number of magnets if the rotation frequency is increased, the regions in which momentum transfer in mainly being transferred migrates from the magnet's sides towards the depth at which the center of the magnet passes.

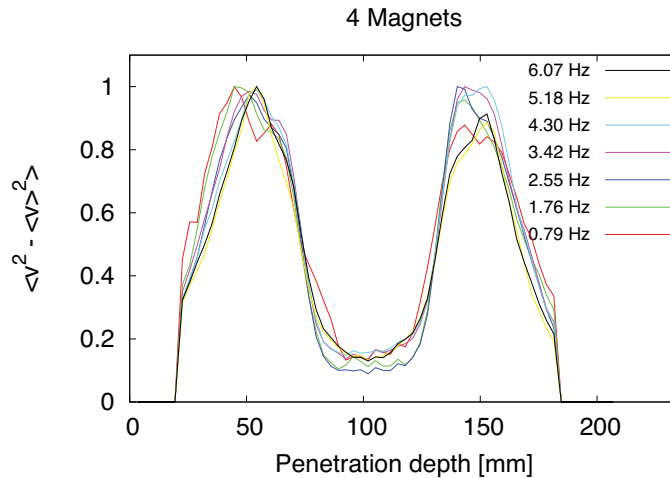


Fig. 4.13. Normalized velocity fluctuation profiles for all MRFs when four magnets are used. $r = 42$ mm.

Figure 4.14(a) and (b) show the comparison of the velocity fluctuations profiles

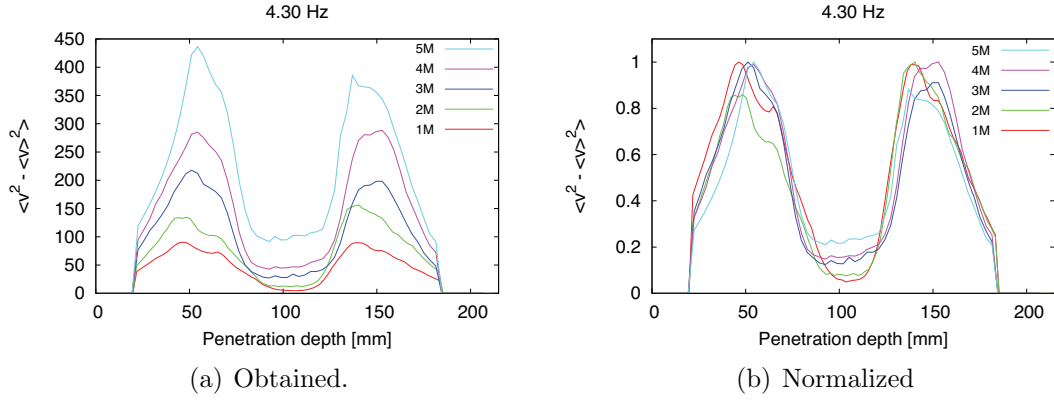


Fig. 4.14. Velocity fluctuations profiles for magnet rotation frequency of 4.30 Hz for all arrays of magnets used. $r = 42$ mm.

for the used ordered arrays when they rotate at 4.30 Hz. As in previous cases, we notice that if we increase the number of magnet, the intensity of fluctuations grows and the maximums also migrate towards the center of the magnets. This latter fact is more noticeable when we analyse arrays of magnets rotating at 29.1 mm from axis. In Figures 4.15(a) and (b) the velocity fluctuations profiles are shown for some analysed MRFs for an array of four magnets. In this case the intensity increase as the MRF does, but the distribution momentum transfer is very different from experiments presented before. Now the magnets are close enough in such a way that after certain rotation frequency a single vortex, defined by a "Gauss-like" profile, is produced. We observe that for low frequencies the main locations of momentum transfer are close to wall, not in the magnet zone as in the case of 42.2 mm. It is only done at frequencies close to 2 Hz for an array of four magnets.

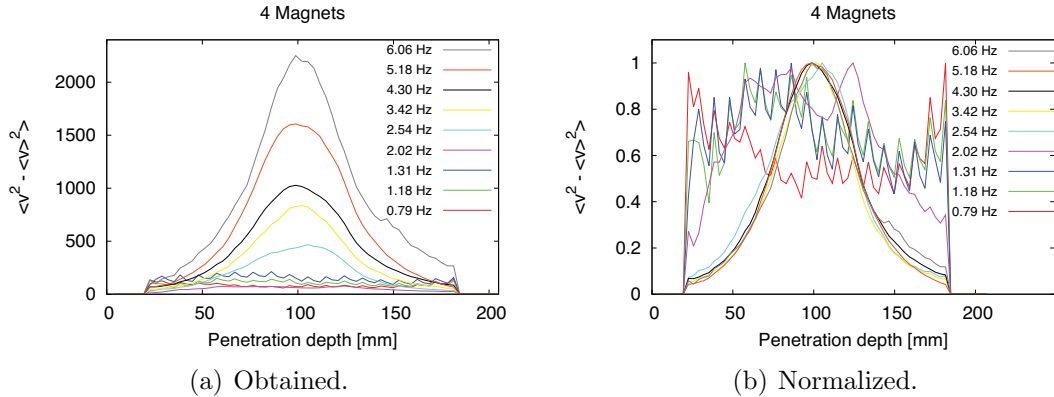


Fig. 4.15. Velocity fluctuations profiles for all analysed magnet rotation frequencies when four magnets are used. $r = 29$ mm.

Using the velocity fluctuation definition it was possible to distinguish the characteristic distribution of places where momentum is mainly being transferred. Results show that each pattern has a well defined profile: the "leaves-like" pattern is

characterized by a μ -shape profile, while the travelling single vortex by a Gaussian profile. In general, we can say that as we increase the number of magnets or their rotation frequency it is possible to modify the flow pattern from a “leaves-like” one to a travelling single vortex. In the 29.1 mm case this change occurs within the experimental parameters. In the other hand, when magnets are located at 42.2 mm from axis it is probably needed a higher magnet rotation frequency as suggested by Figure 4.13 or a higher number of magnets Figure 4.14(b).

4.3.3 Image processing

Experimental investigations are full of lucky events that lead to interesting things. This analysis was not the exception. While performing the experiment where UDV technique was used, we observed at the ceiling of the laboratory that under certain conditions well defined forms appear (see Figures 4.18 and 4.19). After a carefully observation of forms produced at different experiments we could conclude that those well defined forms only occur when free surface of the liquid metal oscillates. It was possible to observe thanks to the high reflecting properties of the free surface of the liquid metal. The analysis shown in this section corresponds image processing of the recordings of those reflections. These videos were taken just at magnet rotation frequencies were FSO exist.

Videos, 90-150 s long, were taken in color using a handycam Sony HDR-XR160 in HD format that allow us to obtain 60 fps. By the Nyquist theorem the maximum measurable frequency is 30 Hz. Videos, taken once the fully developed flow was reached, were then decomposed in a series of images in RGB format (Figure 4.16(a)) whose dimensions are 1900×901 . Then all images were converted into grayscale intensity images (Figure 4.16(b)). Just for the sake of clear forms visualization these latter images were converted into Black and White images (Figure 4.16(b)).

Six points were picked arbitrarily from grayscale images (see Figure 4.16(b)) and its grayscale intensity I , whose values range from 0 to 256, was obtained as function of time. Figure 4.17(a) show the grayscale intensity for five seconds of experiment. In legend the corresponding coordinates of the selected points are indicated, where the origin is located at the left upper corner of images. Analysis by FFT was made to the data obtained $I_i(t)$. Figure 4.17(b) shows the results for analysis cited before. We observe, as in previous FFT analysis, that in addition to the main frequency, its harmonics also appears. Additionally, from Section 4.3.2 we have that the maximum FSO frequency obtained was ~ 8.6 Hz, so we dismiss higher frequencies. Even that we can not distinguish from presented plot small frequencies characteristics of the flow studied (less than 0.5 Hz), in all analysed cases it exist.

Results of this analysis will be given in next subsection were they are compared with that obtained from the analysis to UDV data. Before, we will comment the well defined forms observed in the free surface when it oscillates. As shown in Figure 4.3 the magnetic field intensity is smaller at the free surface if compared with the bottom of the container. Then the moving magnet will not only produce

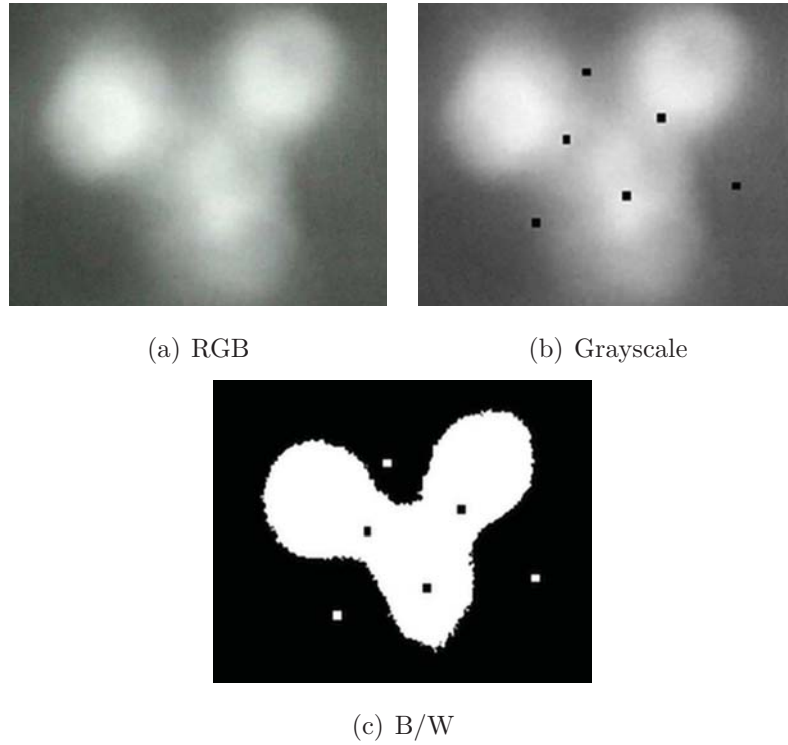


Fig. 4.16. Image is obtained from video in RGB format (a), then is converted to Grayscale format (b) where points are picked for analysis. B/W figure (c) is only for visualization. 3 magnets at 42.2 mm from axis rotating at 1.45 Hz.

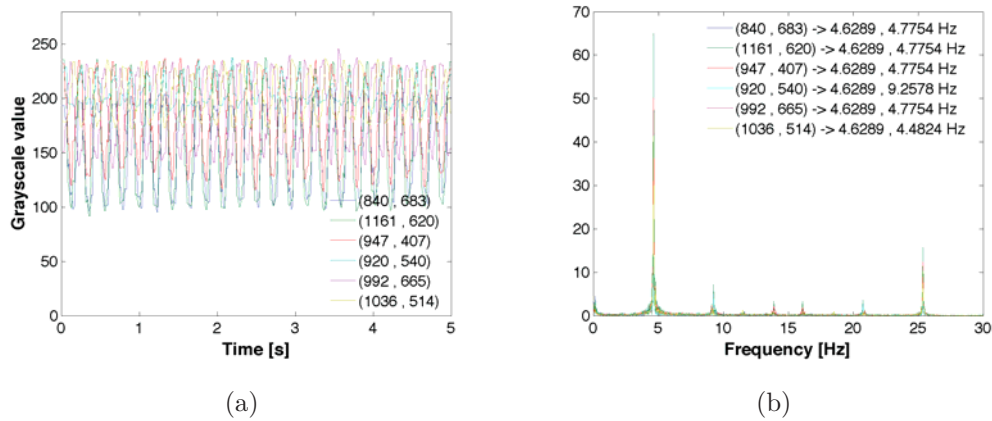


Fig. 4.17. (a) Grayscale intensity I_i as function of time for the six analysed. (b) FFT analysis. 3 magnets rotating at 1.46 Hz.

a flow around it but also it will impulse part of the fluid in the vertical direction. As a result, at a given time, a peak will be formed above the magnets while in the space between magnets a depression of the free surface will take place. In Figures 4.18 and 4.19 the high intensity spots (white) correspond to depressions on the surface. It is well know that the movement of an object (obstacle) in a fluid will

produce waves on its surface^[161]. We may think in the free surface produced by the rotation of a magnet roughly as a flat surface with a small elevation above the magnet. Now, we consider that this small elevation moves a little. This movement will produce waves that propagates all along the free surface. As we have that this small elevation moves permanently inside fluid, waves are generated all time. The final form of the free surface will be the addition of the elevations produced by the magnets and the waves produced by their movement. The characteristics of these waves will depend on the geometry of the container, the surface tension and density of the fluid, as well as in the number of magnets and their rotation frequency, and additionally on the electrical conductivity of the fluid and the strength and shape of the magnetic field as we have a high conducting fluid. As a result we have a complex flow in which well defined forms in the GaInSn free surface can only be seen just under certain condition.

Figure 4.18 shows snapshots of several experiments using magnets at 42.2 mm from axis. During all experiment the showed forms remain equal, but it rotates at frequencies given in next section. We notice that in general the number of spots is defined by the number of magnets used. If we increase rotation frequency maintaining the number of magnets constant, the unique set of spots observed (see for example Figure 4.18(e)) is modified to form a set of six spots that also can be seen as two sets of spots (see Figure 4.18(f)): one in the inner part of the circumference described by the magnets, and the second in the outer part. If the MRF is high enough, the inner spots merge to form a meniscus (Figure 4.18(j)). We must remark that oscillations are *only* present in regions close to the obtained FSO frequencies shown in Figures 4.7 and 4.8, namely they appear in an intermittent and irregular way. For example, if one magnet is placed at 42.2 mm from axis, FSO occurs only for MRFs of 0.9, 1.75 and 2.8 Hz. We observe that for 0.9 and 2.8 Hz the region in which oscillation appears is bigger compared with the region of 1.75 Hz. In general, it was observed that continuous regions where oscillations exist are smaller than 0.2 Hz, for example from 2.7 to 2.9 Hz in mentioned case.

Image analysis through correlations can give us information, for example about the shape and motion, of the depicted object or phenomenon. In our case, the grayscale intensity images can be used to estimate the depth of depressions^[162] of the free surface. In present work it was not made, but we can say roughly that a higher intensity of a pixel indicates a greater depth at that point and viceversa. From Figure 4.18 two cases must be highlighted. Firstly, (a), in which two depressions are observed but just one magnet used. The reason of this can be inferred from Figure 4.7, where we notice that the oscillation frequency is almost twice the corresponding MRF, so it fits to the tendency line corresponding to an array of two magnets. Second, (c) shows the FSO produced by two magnets rotating at 0.96 Hz and we observe six spots, fact that shows that proposed flow patterns are consistent with experimental observations. We notice that predominantly the evolution of free surface forms when it oscillates is as follows: at small FSO frequencies some forms may be distinguished (see 4.18(c)), as we increase the frequency

these forms becomes well defined (see (d) or (e)). For higher frequencies the well defined forms “split” into two sets as referred before (see (f) and (h)) and finally the inner set merge to form a single vortex whose rotation axis coincides with the cylinder axis (see (j)).

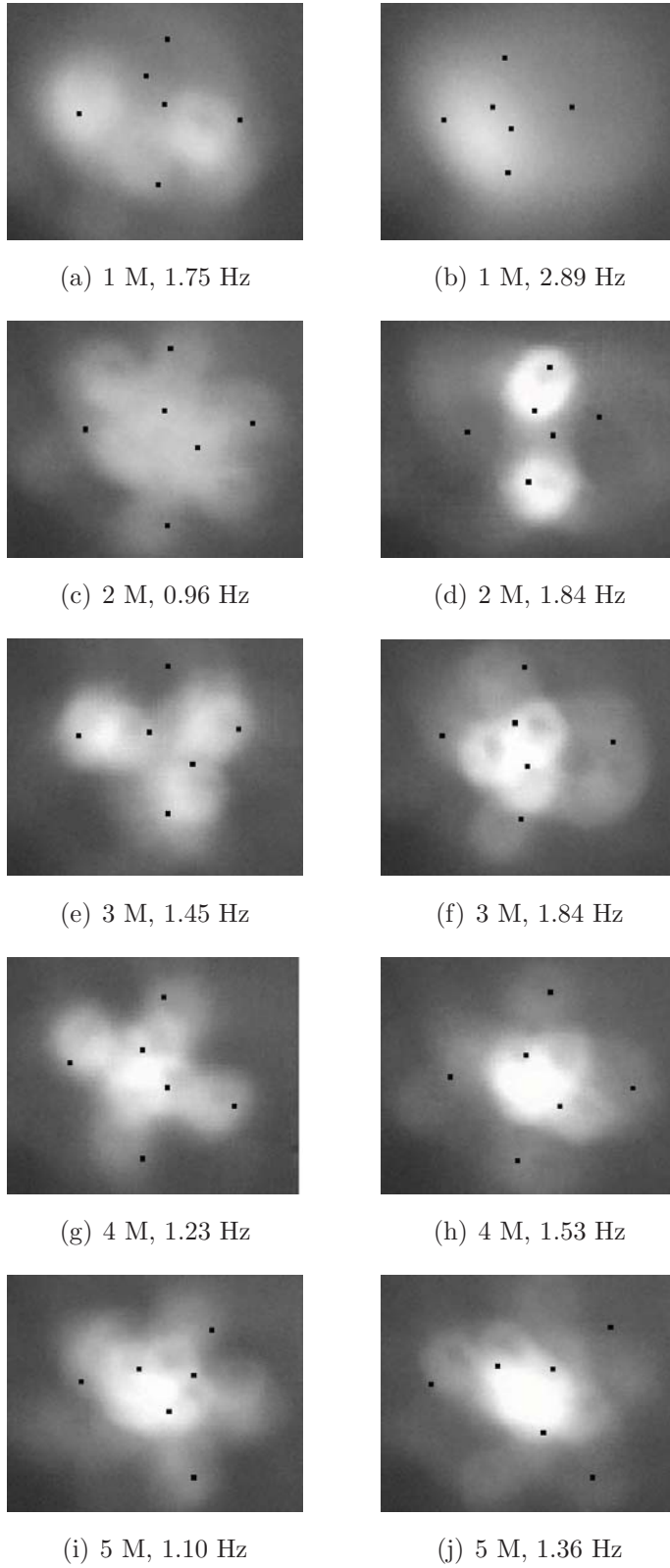
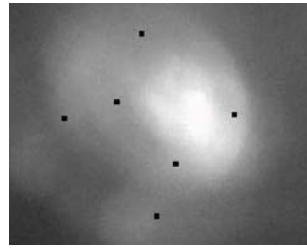
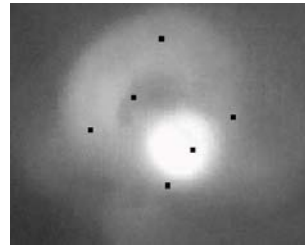


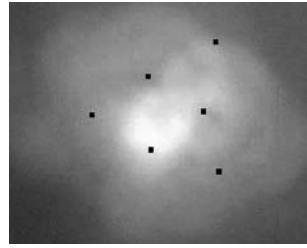
Fig. 4.18. Snapshots in grayscale of several experiments. Magnets rotate at 42.2 mm from axis.



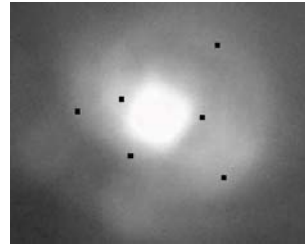
(a) 1 M, 2.89 Hz



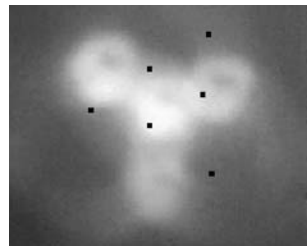
(b) 1 M, 4.31 Hz



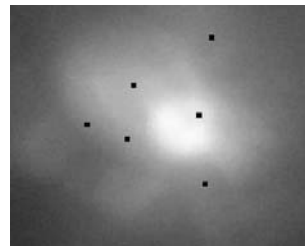
(c) 2 M, 1.76 Hz



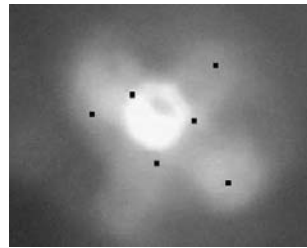
(d) 2 M, 2.89 Hz



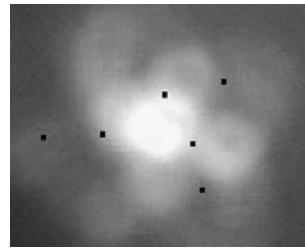
(e) 3 M, 1.41 Hz



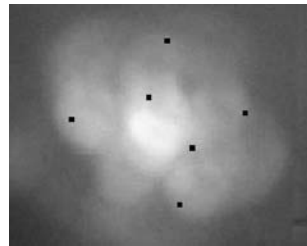
(f) 3 M, 5.18 Hz



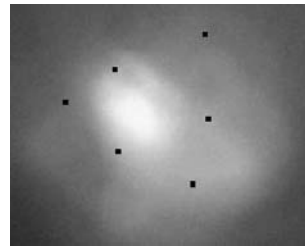
(g) 4 M, 1.19 Hz



(h) 4 M, 1.54 Hz



(i) 5 M, 1.32 Hz



(j) 5 M, 5.18 Hz

Fig. 4.19. Snapshots in grayscale of several experiments. Magnets rotate at 29.1 mm from axis.

Figure 4.19 shows snapshots of several experiments using magnets at 29.1 mm from axis. As in the case of magnets at 42.2 mm from axis, phenomena are described in general as mentioned above. The main difference is that now a new structure appears: a single vortex translating in a loop. This structure has been already defined in previous sections. We can observe the rotating vortex alone in subfigures (f) and (j), where the depression are located far from the magnets rotation axis (this can be inferred from pictures corresponding to the same number of magnets but at lower frequencies). The single vortex coexisting with other structure can be viewed in subfigures (g)-(i). These results are in complete concordance with the threshold plot shown in Figure 4.9.

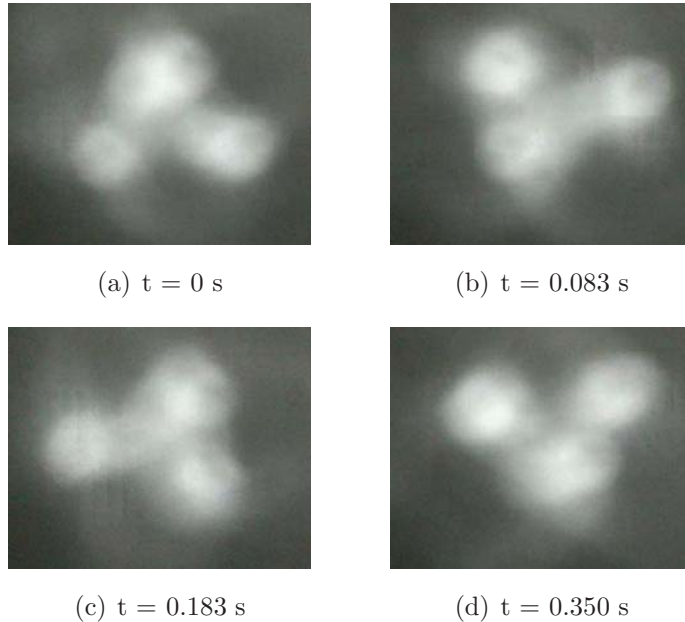


Fig. 4.20. Snapshots at four instants of an experiment with 3 magnets located at 42.2 mm from axis and rotating at 1.46 Hz.

In Section 4.3.2 was mentioned just that when the normalized FSO frequencies of all experiments are compared, they fit to a line whose slope is $m = 1.06$ (see Figure 4.10). This means that for a given MRF, if FSO exists, it does with a frequency slightly higher than the MRF. This effect was detected by UDV data analysis, but any effects on the flow are not possible to infer. In part, this was achieved by image processing. Figure 4.20 shows snapshots of the reflected free surface at four instants of an experiment with 3 magnets located at 42.2 mm from axis and rotating at 1.46 Hz. We observe that the depressions follow strange paths. Actually, it seems that due to the difference in rotation frequencies one of the spots is thrown away from the center, as we can see in the figure. Then, the higher frequency of the flow structure causes a phase shift such that the form observed is disordered but immediately after recover its initial state. This disorder depend on the flow conditions, in some cases it was very noticeable but in other do not. With the information obtained until now, these is what we can say about

the effects produced by a slope m different that unity.

4.3.3.1 UDV and Image Processing results comparison

In order to validate the results obtained by applying the FFT analysis to the videos, these latter where compared with that obtained by UDV analysis. Figures 4.21 and 4.22 shows the comparison of both results. Red squares correspond to UDV analysis results while blue circles and squares to image processing results.

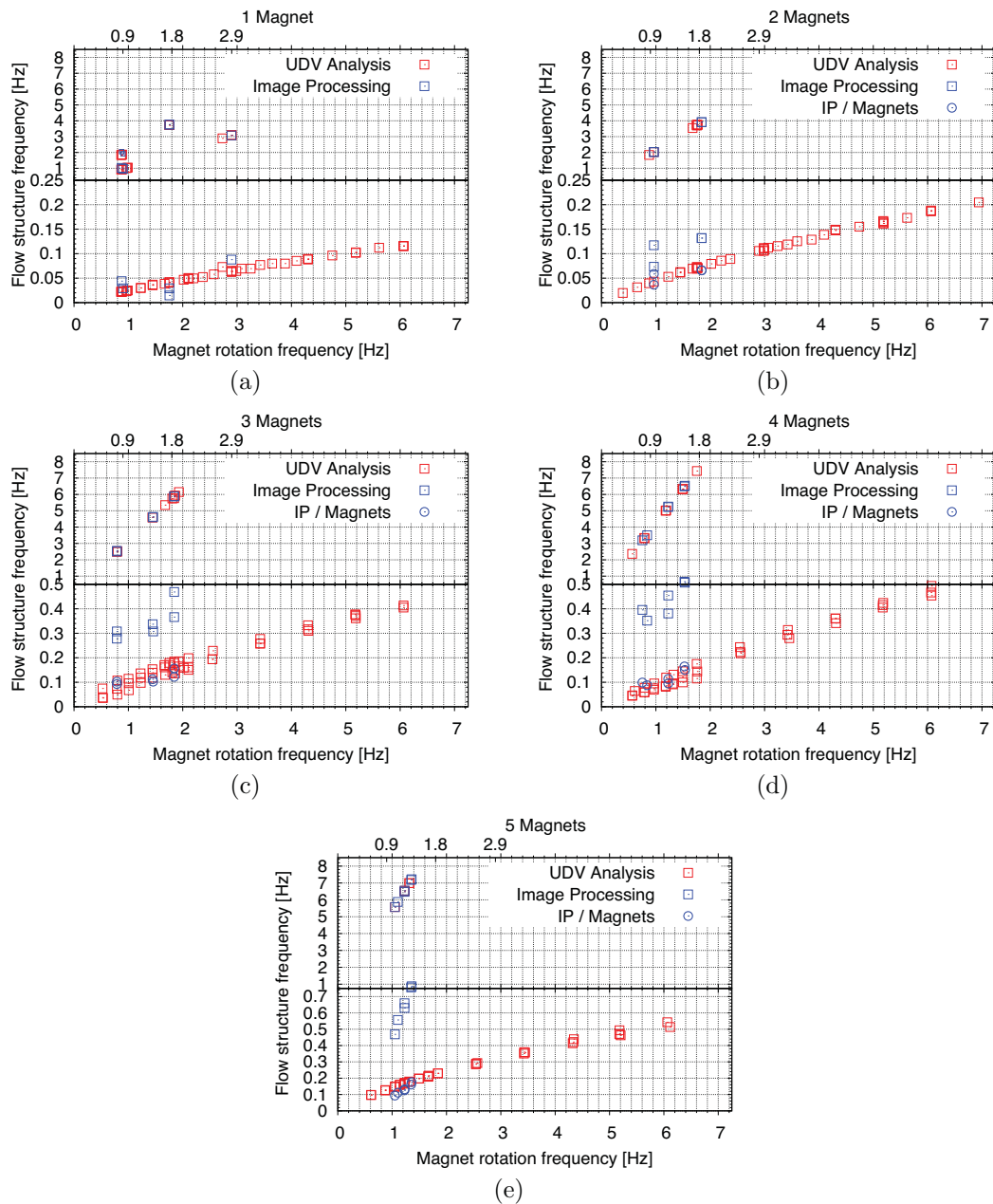


Fig. 4.21. Comparison of frequencies obtained by UDV and Image Processing analysis for 1 magnet (a), 2 magnets (b), 3 magnets (c), 4 magnets (d) and 5 magnets (e) for a rotation radius of 42.2 mm.

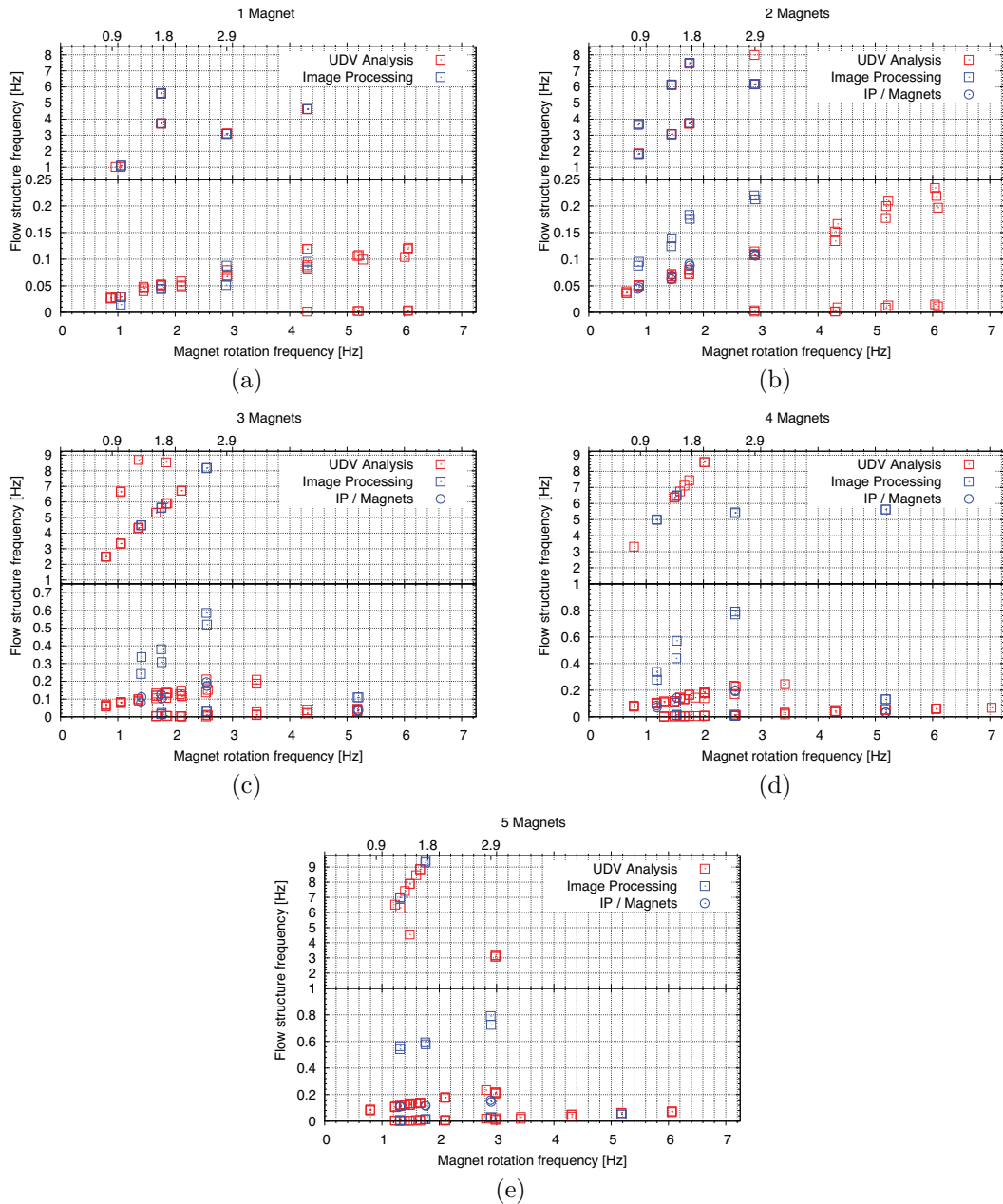


Fig. 4.22. Comparison of frequencies obtained by UDV and Image Processing analysis for 1 magnet (a), 2 magnets (b), 3 magnets (c), 4 magnets (d) and 5 magnets (e) for a rotation radius of 29.1 mm.

In both figures we may see that the results obtained by both methods agree well, specially the frequencies corresponding to free surface oscillation (in both analysed cases) and single vortex structure (just in the case of 29.1 mm). A particular mention must be done about the frequencies corresponding to what we assume as “Leaves-like” pattern. The result is presented as blue squares, we observe that these frequencies are higher than the obtained by UDV analysis, but has the same tendency. If we divide this frequencies by the number of magnets used, seeing

as blue circles in figures, we notice that the *normalized frequency* coincides with the results of UDV analysis. This apparent mismatching in the results may be attributed to the noise generated by well defined forms shown in Figures 4.21 and 4.22 which we argued previously are related to the number of magnets used.

4.4 Conclusions

It was presented the study of the flow in an acrylic cylindrical container, filled with GaInSn, produced by an array of magnets rotating behind it. Two configurations were used: magnets equidistantly located at 42.2 mm and at 29.1 mm from rotation axis. The analysis was made by ultrasound Doppler velocimetry and complemented with image processing analysis. FFT analysis was applied to the data obtained by UDV, $v_{USBeam}(z, t)$. Results show the existence of three different structures characterized by a different ranges of frequencies. One is the free surface oscillations. These appear in both analysed cases and it does at frequencies higher than 0.7 Hz and up to 8.5 Hz. Second, a single vortex translating in a circular loop whose range of frequencies is 0 - 0.065 Hz. It only appears for magnets located at 29.1 mm from axis when either the number of magnets or the magnet rotation frequency is high enough to destabilize the proposed pattern flows defined as “Leaves-like” flow. This latter occurs in both cases and corresponds to the third structure whose frequencies range is from 0.02 - 0.6 Hz. In the cases of magnets at 29.1 mm from axis, a transition from a “Leaves-like” pattern to a single vortex pattern takes place. This transition takes places at smaller frequencies as the number of magnets or the magnet rotation frequency increase. In fact we purpose that at the very beginning of the motion a $4n$ pattern is formed, it change to a $2 + 4n$ pattern in the threshold zone and finally all vortices collapse into one bigger that eventually becomes eccentric. Even that these structures agree with experimental data, other patterns may also agree.

In the other hand, if we look to the comparison of the normalized free surface oscillation frequency for all arrays, we notice that the most of frequencies fitted to a linear function whose slope is $m = 1.06$. This means that the flow structure frequency is slightly higher than the corresponding MRF. The difference in frequencies leads to a phase shift that was seen in the image processing analysis as a desynchronized rotation of the observed depressions (spots). Results obtained through image processing analysis have a good agreement with that obtained by UDV analysis.

Additionally, the velocity fluctuation definition was used to determine the characteristic distribution of places where momentum is mainly being transferred. Results show that each pattern has a well defined profile: the “leaves-like” pattern is characterized by a μ -shape profile, while the travelling single vortex by a Gaussian profile. In general, we can say that as the number of magnets or their rotation frequency is increased, it is possible to modify the flow pattern from a “leaves-like” one to a travelling single vortex. In the 29.1 mm case this change occurs within the experimental parameters. In the other hand, when magnets are located at

42.2 mm from axis it is probably needed a higher magnet rotation frequency as suggested by Figure 4.13 or a higher number of magnets Figure 4.14(b).

Chapter 5

Concluding remarks

Several magnetohydrodynamic (MHD) flows were studied experimentally. The importance of their analysis lies on its applications; mhd pumping is relevant in microfluidics and electromagnetic stirring in electromagnetic processing of materials (EPM). Specifically three different problems were studied. The first part was devoted to the study of MHD pumps. Firstly the consequences on the flow of consider fluid/wall slippage in micropumps were analysed analytical and numerically, and comparison with available experimental data was done. It was found that when slippage in all walls exists with a slip length as small as one hundredth of the characteristic length, significant increments on the flow rate can be achieved. These may lead to considerable savings on energy, or in other words, to increase the efficiency of the micropump. Additionally, the flow in an open channel forming a closed loop and driven by a conduction MHD pump at millimetric scale was studied using the PIV technique. Results confirm the fully developed flow, characterized by a parabolic profile, in the hydrodynamic zone. In the pumping zone a more complicated flow was observed, where recirculations in the electrodes region appear. In order to have a better understanding it is necessary to perform experiments at different positions, for example, after and before the electrodes zone where inhomogeneities in electric and magnetic fields exist. Measurements at different heights would be very helpful also in order to reconstruct the three dimensional velocity field. Such measurements could be used to validate numerical models developed at the UNAM as well as obtained by commercial software.

In the second part, two configurations of flows past a magnetic obstacle were characterized by Ultrasound Doppler Velocimetry (UDV). All experiments were performed at the facilities of the Ilmenau University of Technology, Germany where and academic stay was done. The purposes of this stay were to get training in the usage of UDV and in handling of the liquid metal (GaInSn) in order to apply this knowledge at the facilities of the UNAM. These two objectives can be considered as two main goals of current project.

Finally, the design and analysis of a MHD stirring device based on a localized rotating magnetic field was presented. Analysis was done to the velocity data obtained by UDV and to the free surface recordings. Results obtained by both ways

shown a good agreement. Even that flow produced by the rotation of magnets is complex, some flow patterns were purposed. The methodology used for the analysis was developed and its implementation to measurements of the three components of velocity by UDV is rather simple. In present work just the analysis of magnets located at two different rotation radii with a fixed liquid metal layer were done, but an extensive study of flows at other radii, layer depths and cylinder diameter are needed. This measurements could include the usage of several transducers located radially and axially or even 2D- or 3D-UDV, depending on the experiment setup. Also, some improvements can be made to the actual device, for example the cylindrical container can be done in one piece of Teflon. This avoids the apparition of fractures due to strains in the acrylic joints, but visual access to the free surface is restricted.

Summarizing, to our knowledge, liquid metal (GaInSn) experiments performed at the CIE-UNAM facilities have not been preformed previously Mexico. Experience gained with this project will be helpful for the consolidation of the experimental group of the Thermosciences department. Methodology and computational tools to help in the analysis of liquid metal flow were also developed, and these could serve as the basis of further investigations.

Appendix A

MHD equations

The equations that govern the flow of electrically conducting incompressible fluids under magnetic fields involve the equation of continuity and the Navier-Stokes equation with a Lorentz force term. This term couples the hydrodynamic equations with the electromagnetic equations in their pre-Maxwellian form. In addition to this set of equations, a constitutive relation is needed, namely, the Ohm's law. The formulation based on the induced magnetic field (B -formulation) and the velocity is used, despite the fact that different primitive variables can be chosen^[163].

Fluid Dynamics Equations

Gases and liquids are treated as incompressible fluids in a wide range of applications and thus their density can be considered constant. Under this assumption the mass balance equation is

$$\nabla \cdot \vec{u} = 0 , \tag{A.1}$$

where \vec{u} is the velocity field. In the other hand, we are interested in Newtonian fluids, namely liquid metals (for instance, the eutectic ally GaInSn^[164]) and electrolytes. The momentum equation that describes the dynamics of such fluids is the Navier-Stokes equation, namely,

$$\frac{\partial \vec{u}}{\partial t} + (\vec{u} \cdot \nabla) \vec{u} = \frac{1}{\rho} \nabla p + \nu \nabla^2 \vec{u} + \frac{1}{\rho} \vec{f} , \tag{A.2}$$

where ρ , ν , p , and \vec{f} are the density, kinematic viscosity, pressure and external forces, respectively. In particular, when an electrically conducting fluid interacts with electromagnetic fields, the relevant force is the Lorentz force which it is explicitly presented below.

Although heat transfer processes are not considered in this work, the energy balance or heat transfer equation is presented for completeness. If electromagnetic interaction exists, this equation takes the form

$$\rho c_p \left[\frac{\partial T}{\partial t} + (\vec{u} \cdot \nabla) T \right] = \nabla \cdot (k \nabla T) + \frac{\vec{j}^2}{\sigma} + \Phi_\nu , \quad (\text{A.3})$$

where T is temperature, \vec{j} the electric current density, Φ_ν the viscous dissipation function, c_p the heat capacity at constant pressure, k the thermal conductivity and σ the electric conductivity of the medium. The second term of the right hand side (*rhs*) of Eq. (A.3) is the Joule dissipation due to the electric currents circulating in the fluid. Evidently, the former set of equations (A.1)-(A.3) is not complete and must be complemented with the electromagnetic field equations, that in addition to the Maxwell equations and Lorentz force include constitutive equations that characterize the fields in distinct mediums.

Electromagnetic Field Equations

Experimental laws of electricity and magnetism can be summarized in a set of expressions known as Maxwell equations. These equations relate electric field strength vector, E , and magnetic induction field, B , with their sources, namely charges and electric currents. In an isotropic, homogeneous and linear medium the macroscopic Maxwell equations are the following:

The *Gauss law* establishes that the electric flux through any closed surface is proportional to the enclosed electric charge. In differential form this law is expressed as

$$\nabla \cdot \vec{E} = \frac{\rho_e}{\epsilon} , \quad (\text{A.4})$$

where ρ_e is the total electric charge density and ϵ the electric permittivity in the medium.

The *Gauss law for magnetism* expresses the nonexistence of isolated magnetic charges or magnetic monopoles. The distribution of magnetic sources is always neutral in the sense that they have north and south poles such that the net magnetic flux through any enclosed surface is always zero. This can be expressed as

$$\nabla \cdot \vec{B} = 0 . \quad (\text{A.5})$$

The *Faraday law of induction* states that the induced electromotive force (EMF) in any closed circuit is equal to minus the rate of change of the magnetic flux through the circuit. This law establishes the possibility to produce electric fields from magnetic fields varying in time. In differential form this law can be expressed as

$$\nabla \times \vec{E} = - \frac{\partial \vec{B}}{\partial t} . \quad (\text{A.6})$$

The *Ampère-Maxwell law* states that magnetic fields can be generated by means of electric conduction currents (original Ampère's law) and by electric fields varying

in time (Maxwell correction). The Maxwell correction term is called the displacement current and is fundamental in the description of radiative phenomena. The differential expression of this law is

$$\nabla \times \vec{B} = \mu \vec{j} + \mu \epsilon \frac{\partial \vec{E}}{\partial t}, \quad (\text{A.7})$$

where μ is the magnetic permittivity of the medium.

If we apply the divergence operator to Eq. (A.7) and use the Gauss law (A.4), we obtain the conservation equation for the electric current or continuity equation, namely,

$$\nabla \cdot \vec{j} + \frac{\partial \rho_e}{\partial t} = 0. \quad (\text{A.8})$$

Maxwell equations must be complemented with a constitutive equation that relates the electric current density in the medium with the electric and magnetic fields \vec{E} and \vec{B} . The constitutive equation that is found to be suitable in a wide range of physical situations, and in particular with liquid metals and electrolytes, is the *Ohm's law*. This law states a linear relation between the electric current density and the “effective” electric field in the medium. In the laboratory reference frame respect to which the fluid moves with a velocity \vec{u} , the *Ohm's law* is expressed as

$$\vec{j} = \sigma \left(\vec{E} + \vec{u} \times \vec{B} \right) + \rho_e \vec{u}, \quad (\text{A.9})$$

where last term in the *rhs* is known as the convection current density.

Finally, we must consider the electromagnetic force exerted on the medium due to the presence of electric and magnetic fields. In a continuous medium with charge density ρ_e and electric current density \vec{j} , the electromagnetic force is given by

$$\vec{f} = \rho_e \vec{E} + \vec{j} \times \vec{B}, \quad (\text{A.10})$$

which is known as *Lorentz force*.

MHD Approximation

Fluid dynamics equations are non-relativistic and invariant to Galilean transformations. On the other hand, electromagnetic field equations are relativistic and invariant to Lorentz transformations. In order to combine the two sets of equations consistently it is necessary to simplify these equations by using what is known as the MHD approximation, based on the following assumptions:

- The fluid velocity is much smaller than the velocity of light, $u^2 \ll c^2$ (non-relativistic approximation).
- Magnetic fields are quasi-stationary or at low frequencies.
- Electric fields are of the order of magnitude of the induced electromotive forces $\vec{u} \times \vec{B}$.

Under the MHD approximation it is possible to simplify the electromagnetic field equations so that altogether with the fluid dynamics equations, conform the complete system of MHD equations. Among the most important simplifications is to neglect the Maxwell displacement current in Ampere-Maxwell law as well as the convection current density in Ohm's law and the electric term in the Lorentz force. It can be shown that these terms are $\mathcal{O}(u^2/c^2)$, and can be neglected. A detailed analysis of the MHD approximation can be found in Shercliff^[165] and Hughes & Young^[166]. Under this approximation the MHD fundamental equations are

$$\nabla \cdot \vec{u} = 0 , \quad (\text{A.11})$$

$$\frac{\partial \vec{u}}{\partial t} + (\vec{u} \cdot \nabla) \vec{u} = \frac{1}{\rho} \nabla p + \nu \nabla^2 \vec{u} + \frac{1}{\rho} \vec{j} \times \vec{B} , \quad (\text{A.12})$$

$$\nabla \times \vec{E} = -\frac{\partial \vec{B}}{\partial t} , \quad (\text{A.13})$$

$$\nabla \times \vec{B} = \mu \vec{j} , \quad (\text{A.14})$$

$$\nabla \cdot \vec{B} = 0 , \quad (\text{A.15})$$

$$\vec{j} = \sigma \left(\vec{E} + \vec{u} \times \vec{B} \right) . \quad (\text{A.16})$$

These constitute a complete set of equations that describes the dynamics of the flow of an electrically conducting fluid under an electromagnetic field. In this approximation is appropriate to ignore the Gauss law (A.4) because the electric field is fully determined by the Faraday's law (A.13) and the Ohm's law (A.16). Furthermore, the electric charge distribution is not of interest in MHD. Moreover, in Eq. (A.14) for liquid metals and electrolytes, it is a good approximation to consider the medium magnetic permittivity as that of the vacuum. In the equation system (A.11) - (A.16) heat transfer equation (A.3) does not appear but it can be included when heat transfer phenomena are considered.

From equations (A.13)-(A.16) it is possible to obtain the induction equation of the magnetic field^[55] that describes the transport of magnetic field by convection and diffusion. In order to obtain it, we substitute the electric current from Eq. (A.14) into Ohm's law (A.16), then the electric field from the resulting equation is substituted into Faraday's law (A.13). The final expression of the induction equation is reached using the Gauss law for magnetism, resulting

$$\frac{\partial \vec{B}}{\partial t} = \nu_m \nabla^2 \vec{B} + \nabla \times \left(\vec{u} \times \vec{B} \right) , \quad (\text{A.17})$$

where $\nu_m = 1/\mu_0\sigma$ is known as the magnetic diffusivity. The first term of the *rhs* of Eq. (A.17) corresponds to the transport by diffusion, the second one to the transport by convection. We notice that the dominant mechanism of transport for a given problem is determined basically by the electrical conductivity of the fluid. If is a highly conducting fluid convection dominates, if is a poor conductor

diffusion does. In the most of the MHD flows in laboratory and industry diffusive effects of the magnetic field dominates.

Equations (A.11), (A.12) and (A.17) constitute a system of seven unknown quantities, \vec{u} , p and \vec{B} . These will be the variables that we will consider in this work. However, the solution of these equations does not ensure a solenoidal magnetic field, the condition (A.15) must be imposed. Once that the magnetic field has been determined, the electric current density can be obtained from Eq. A.14.

REFERENCES

- [1] H. Li, C. D. Dowell, A. Goodman, R. Hildebrand, and Novakm G. Anchoring magnetic field in turbulent molecular clouds. *The Astrophysical Journal*, 704(2), 2009.
- [2] J. Larmor. Possible rotational origin of magnetic fields of sun and earth. *Electrical Review*, 85:412, 1919.
- [3] P. H. Roberts. *An Introduction to Magnetohydrodynamics*. American Elsevier, 1967.
- [4] E. N. Parker. The origin of magnetic fields. *Astrophysical Journal*, 160:383–404, May 1970.
- [5] N. Ma and J. S. Walker. Electromagnetic stirring in crystal growth processes. *Fluid Dynamics & Materials Processing*, 2(2):119–125, 2006.
- [6] M. Motokawa, M. Hamai, T. Sato, I. Mogi, S. Awaji, K. Watanabe, N. Kitamura, and M. Makihara. Crystal growth and materials processing in the magnetic levitation condition. *Journal of Magnetism and Magnetic Materials*, 226 - 230:2090 – 2093, 2001.
- [7] K. Sassa, S. Ninagawa, and S. Asai. Liquid metal atomization by the use of electromagnetic force. *Magnetohydrodynamics*, 28(3):248–252, 1992.
- [8] G. Kronkalns, M. M. Maiorov, and E. Blums. Heating of magnetic fluids by a low frequency alternating magnetic field. *Magnetohydrodynamics*, 47(3):249 – 264, 2011.
- [9] E. Ya. Blum. Heat and mass transfer in a magnetic field. *Magnetohydrodynamics*, 11(1):27 – 36, 1975.
- [10] J. P. Verkamp and R. G. Rhudy. Electromagnetic alkalimetal pump research program. Technical report, National Aeronautics and Space Administration, February 1966.
- [11] J. Hartman and F. Lazarus. Hg-dynamics II - theory of the laminar flow of an electrically conductive liquid in a homogeneous magnetic field. *Mathematisk-Fysiske Meddelelser*, 15(7), 1937.
- [12] H. Branover. *Metallurgical Technologies, Energy Conversion, and Magnetohydrodynamic Flows*, volume 148. American Institute of Aeronautics and Astronautics, 1993.
- [13] Peter Mitchell. Microfluidics - downsizing large-scale biology. *Nature Biotechnology*, 19:717–721, 2001.

- [14] N.-T. Nguyen and S. T. Wereley. *Fundamentals and applications of microfluidics*. Artech House, 2002.
- [15] G. Karniadakis, A. Beskok, and N. Aluru. *Microflows and Nanoflows: Fundamentals and Simulation*. Springer, 2005.
- [16] S. Hardt and F. Schönfeld, editors. *Microfluidic Technologies for Miniaturized Analysis Systems*. MEMS Reference Shelf. Springer, 2007. Chapter 2.
- [17] S. Qian and H.H. Bau. Magneto-hydrodynamics based microfluidics. *Mechanics Research Communications*, 36(1):10–21, 2009.
- [18] Richard Ellson. Picoliter: enabling precise transfer of nanoliter and picoliter volumes. *Drug Discovery Today*, 7(5):S32S34, March 2002.
- [19] Y.-Y. Lin, Erin R. F. Welch, and R. B. Fair. Low voltage picoliter droplet manipulation utilizing electrowetting-on-dielectric platforms. *Sensors and Actuators B: Chemical*, In Press, Corrected Proof, 2012.
- [20] Ph. Luginbuhl, P.-F. Indermuhle, M.-A. Grétilat, F. Willemin, N. F. de Rooij, D. Gerber, G. Gervasio, J.-L. Vuilleumier, D. Twerenbold, M. Düggelin, D. Mathys, and R. Guggenheim. Femtoliter injector for DNA mass spectrometry. *Sensors and Actuators B: Chemical*, 63(3):167 – 177, 2000.
- [21] Satoko Yoshizawa. Micro and nanotechnological tools for study of RNA. *Biochimie*, 94(7):1588 – 1594, 2012.
- [22] N.-T. Nguyen, X. Huang, and T. K. Chuan. Mems-micropumps: A review. *Journal of Fluids Engineering*, 124(2):384–392, 2002.
- [23] D. J. Laser and J. G. Santiago. A review of micropumps. *Journal of Micromechanics and Microengineering*, 14(6):R35, 2004.
- [24] Peter Woias. Micropumps-past, progress and future prospects. *Sensors and Actuators B: Chemical*, 105(1):28 – 38, 2005.
- [25] Dongqing Li. *Encyclopedia of Microfluidics and Nanofluidics*. Springer, 2008.
- [26] B. Jian-Bin and D.J. Harrison. Fabrication of microchips for running liquid chromatography by magnetohydrodynamic flow. In *7th International Conference on Miniaturized Chemical and Biochemical Analysis Systems*, pages 407–410, July 2003.
- [27] A. Homsy, S. Koster, J. C. T. Eijkel, A. van den Berg, F. Lucklum, E. Verpoorte, and N. F. de Rooij. A high current density dc magnetohydrodynamic (mhd) micropump. *Lab on a Chip*, 5:466–471, 2005.

- [28] B. Nguyen and S. K. Kassegne. High-current density dc magnetohydrodynamics micropump with bubble isolation and release system. *Microfluidics and Nanofluidics*, 5(3):383–393, 2008.
- [29] Shigeo Asai. *Electromagnetic Processing of Materials*, volume 99 of *Fluid Mechanics and its Applications*. Springer, 2012.
- [30] S. Cuevas, S. Smolentsev, and M. A. Abdou. On the flow past a magnetic obstacle. *Journal of Fluid Mechanics*, 553:227–252, 2006.
- [31] E. V. Votyakov, Yu. Kolesnikov, O. Andreev, E. Zienicke, and A. Thess. Structure of the wake of a magnetic obstacle. *Physical Review Letters*, 98:144504, Apr 2007.
- [32] E. V. Votyakov, E. Zienicke, and Yu. B. Kolesnikov. Constrained flow around a magnetic obstacle. *Journal of Fluid Mechanics*, 610:131–156, 2008.
- [33] E. V. Votyakov and S. C. Kassinos. On the analogy between streamlined magnetic and solid obstacles. *Physics of Fluids*, 21(9), 2009.
- [34] O. Andreev, Yu. Kolesnikov, and A. Thess. Application of the ultrasonic velocity profile method to the mapping of liquid metal flows under the influence of a non-uniform magnetic field. *Experiments in Fluids*, 46(1):77–83, 2009.
- [35] A. Thess, E.V. Votyakov, and Y. Kolesnikov. Lorentz force velocimetry. *Physical Review Letters*, 96(16), 2006. cited By (since 1996) 31.
- [36] V. Minchenya, Ch. Karcher, Y. Kolesnikov, and A. Thess. Calibration of the lorentz force flowmeter. *Flow Measurement and Instrumentation*, 22(3):242 – 247, 2011.
- [37] C. Heineke and A. Thess. Lorentz force velocimetry of turbulent MHD duct flow: Experimental study. In *8th PAMIR International Conference on Fundamental and Applied MHD*, volume 1, pages 341–345, Borgo, France, Sept 2011.
- [38] A. Wegfrass, C. Diethold, M. Werner, C. Resagk, B. Hilbrunner, F. Halbedel, and A. Thess. Development of a novel flow rate measurement device for poorly conducting fluids using lorentz force velocimetry. In *8th PAMIR International Conference on Fundamental and Applied MHD*, volume 1, pages 353–357, Borgo, France, Sept 2011.
- [39] A. Figueroa, F. Demiaux, S. Cuevas, and E. Ramos. Electrically driven vortices in a weak dipolar magnetic field in a shallow electrolytic layer. *Journal of Fluid Mechanics*, 641:245, November 2009.

- [40] A. Figueroa, S. Cuevas, and E. Ramos. Electromagnetically driven oscillatory shallow layer flow. *Physics of Fluids*, 23(1):013601, January 2011.
- [41] J. Jang and S. S. Lee. Theoretical and experimental study of mhd (magneto-hydrodynamic) micropump. *Sensors and Actuators A: Physical*, 80(1):84 – 89, 2000.
- [42] L. Huang, W. Wang, M. C. Murphy, K. Lian, and Z.-G. Ling. Liga fabrication and test of a dc type magnetohydrodynamic (mhd) micropump. *Microsystem Technologies*, 6:235–240, 2000.
- [43] A. V. Lemoff and A. P. Lee. An ac magnetohydrodynamic micropump. *Sensors and Actuators B: Chemical*, 63(3):178 – 185, 2000.
- [44] J. Zhong, M. Yi, and H. H. Bau. Magnetohydrodynamic (mhd) pump fabricated with ceramic tapes. *Sensors and Actuators A: Physical*, 96(1):59–66, 2002.
- [45] B. Jian-Bin and D. J. Harrison. Design and fabrication of microchannels for magnetohydrodynamic flow. In *International Conference on MEMS, NANO and Smart Systems*, pages 396–399, July 2003.
- [46] P. U. Arumugam, E. S. Fakunle, E. C. Anderson, S. R. Evans, K. G. King, Z. P. Aguilar, C. S. Carter, and I. Fritsch. Characterization and pumping redox magnetohydrodynamics in a microfluidic channel. *Journal of The Electrochemical Society*, 153(12):E185E194, 2006.
- [47] H. H. Bau, J. Zhu, S. Qian, and Y. Xiang. A magneto-hydrodynamically controlled fluidic network. *Sensors and Actuators B: Chemical*, 88(2):205–216, 2003.
- [48] H.-J. Kang and B. Choi. Development of the mhd micropump with mixing function. *Sensors and Actuators A: Physical*, 165(2):439 – 445, 2011.
- [49] Y. Deng and J. Liu. Design of practical liquid metal cooling device for heat dissipation of high performance cpus. *Journal of Electronic Packaging*, 132(3):031009, 2010.
- [50] K.-Q. Ma and J. Liu. Heat-driven liquid metal cooling device for the thermal management of a computer chip. *Journal of Physics D: Applied Physics*, 40(15):4722–4729, 2007.
- [51] P.-J. Wang, C.-Y. Chang, and M.-L. Chang. Simulation of two-dimensional fully developed laminar flow for a magneto-hydrodynamic (mhd) pump. *Biosensors and Bioelectronics*, 20(1):115 – 121, 2004.
- [52] Je-Ee Ho. Characteristic study of mhd pump with channel in rectangular ducts. *Journal of Marine Science and Technology*, 15(4):315–321, 2007.

- [53] H. Kabbani, A. Wang, X. Luo, and S. Qian. Modeling redox-based magnetohydrodynamics in three-dimensional microfluidic channels. *Physics of Fluids*, 19(8), 2007.
- [54] H. S. Kabbani, M. J. Mack, S. W. Joo, and S. Qian. Analytical prediction of flow field in magnetohydrodynamic-based microfluidic devices. *Journal of Fluids Engineering*, 130(9):091204, 2008.
- [55] U. Müller and L. Bühler. *Magnetofluidynamics in channels and containers*. Springer, 2001.
- [56] V. Patel and S. K. Kassegne. Electroosmosis and thermal effects in magnetohydrodynamic (mhd) micropumps using 3d mhd equations. *Sensors and Actuators B: Chemical*, 122(1):42–52, 2007.
- [57] Patrick Tabeling. *Introduction to microfluidics*. Oxford, 2005.
- [58] N. V. Priezjev, A. A. Darhuber, and S. M. Troian. Slip behavior in liquid films on surfaces of patterned wettability: Comparison between continuum and molecular dynamics simulations. *Phys. Rev. E*, 71:041608, 2005.
- [59] A. Martini, A. Roxin, R. Q. Snurr, Q. Wang, and S. Lichter. Molecular mechanisms of liquid slip. *Journal of Fluid Mechanics*, 600:257–269, 2008.
- [60] Pierre-Gilles de Gennes. On fluid/wall slippage. *Langmuir*, 18(9):3413–3414, 2002.
- [61] A. D. Stroock, M. Weck, D. T. Chiu, W. T. S. Huck, P. J. A. Kenis, R. F. Ismagilov, and G. M. Whitesides. Patterning electro-osmotic flow with patterned surface charge. *Physical Review Letters*, 84:3314–3317, Apr 2000.
- [62] U. Tallarek, E. Rapp, A. Seidel-Morgenstern, and H. Van Ass. Electroosmotic flow phenomena in packed capillaries: From the interstitial velocities to intraparticle and boundary layer mass transfer. *Journal of Physical Chemistry B*, 106:12709–12721, 2002.
- [63] Y. Ben and H.-C. Chang. Nonlinear smoluchowski slip velocity and microvortex generation. *Journal of Fluid Mechanics*, 461:229–238, 2002.
- [64] S. Smolentsev. Mhd duct flows under hydrodynamic slip condition. *Theoretical and Computational Fluid Dynamics*, 23:557–570, 2009.
- [65] R. Peyret. *Spectral Methods For Incompressible Viscous Flow*. Springer, 2002.
- [66] Y. Xiang and H. H. Bau. Complex magnetohydrodynamic low-reynolds-number flows. *Physical Review E*, 68:016312, 2003.

- [67] W. I. Wu, P. R. Selvaganapathy, and C. Y. Ching. Transport of particles and microorganisms in microfluidic channels using rectified ac electro-osmotic flow. *Biomicrofluidics*, 5:013407, 2011.
- [68] G. F. Naterer. Reducing energy availability losses with open parallel microchannels embedded in a micropatterned surface. *International Journal of Energy Research*, 29:12151229, 2005.
- [69] M. H. Yazdi, S. Abdullah, I Hashim, and K. Sopian. Entropy generation analysis of open parallel microchannels embedded within a permeable continuous moving surface: application to magnetohydrodynamics (mhd). *Entropy*, 14(1):1–23, 2012.
- [70] M. Trypuć and U. Kiełkowska. Solubility in the $\text{NH}_4\text{HCO}_3 + \text{NaHCO}_3 + \text{H}_2\text{O}$ system. *Journal of Chemical and Engineering Data*, 43(2):201–204, 1998.
- [71] F. J. Millero, G. K. Ward, and P. V. Chetirkin. Relative sound velocities of sea salts at 25 °C. *Journal of the Acoustical Society of America*, 61(6):1492–1498, 1977.
- [72] O. Ozdemir, M. S. Çelik, Z. S. Nickolov, and J.D. Miller. Water structure and its influence on the flotation of carbonate and bicarbonate salts. *Journal of Colloid and Interface Science*, 314:545–551, 2007.
- [73] P. M. Sipos, G. Hefter, and P. M. May. Viscosities and densities of highly concentrated aqueous MOH solutions (M^+) Na^+ , K^+ , Li^+ , Cs^+ , $(\text{CH}_3)_4\text{N}^+$ at 25.0 °C. *Physics of Fluids*, 21(9):613–617, 2009.
- [74] C. Kleinstreuer. *Modern Fluid dynamics: Basic Theory and Selected Applications in Macro- and Micro- Fluidics*. Springer, 2010.
- [75] M. M. Zdrakovich. *Flow around Circular Cylinders. Vol. 1: Fundamentals*. Oxford, 1997.
- [76] Alberto Beltrán, Eduardo Ramos, Sergio Cuevas, and Morten Brøns. Bifurcation analysis in a vortex flow generated by an oscillatory magnetic obstacle. *Physical Review E*, 81:036309, Mar 2010.
- [77] D. E. Peterson Yu. M. Gel’fgat and E. V. Shcherbinin. Velocity structure of flows in nonuniform constant magnetic fields I. Numerical calculations. *Magnetohydrodynamics*, 14(1):55–61, 1978.
- [78] Yu. M. Gel’fgat and S. V. Ol’shanskii. Velocity structure of flows in nonuniform constant magnetic fields. II. Experimental results. *Magnetohydrodynamics*, 14(2):151–154, 1978.

- [79] E. V. Votyakov and S. C. Kassinos. Core of the magnetic obstacle. *Journal of Turbulence*, page N49, 2010.
- [80] Signal Processing S.A. <http://www.signal-processing.com/>.
- [81] Yasushi Takeda. Velocity profile measurement by ultrasonic doppler method. *Experimental Thermal and Fluid Science*, 10(4):444 – 453, 1995.
- [82] M. Rivero, O. Andreev, A. Thess, and S. Cuevas. Experimental study of flows past a magnetic obstacle. In pamir, editor, 8th *PAMIR International Conference on Fundamental and Applied MHD*, volume 1, pages 347–351, 2011.
- [83] P. A. Davidson. *An Introduction to Magneto-hydrodynamics*. Cambridge, 2001.
- [84] D. Jian and Ch. Karcher. Electromagnetic flow control using lorentz force velocimetry: experimental investigations and numerical modeling. In *8th PAMIR International Conference on Fundamental and Applied MHD*, volume 2, pages 665–669, Borgo, France, Sept 2011.
- [85] D. Jian and Ch. Karcher. Electromagnetic flow measurements in liquid metals using time-of-flight Lorentz force velocimetry. *Measurement Science and Technology*, 23(7):074021, 2012.
- [86] O. Andreev, Yu. Kolesnikov, and A. Thess. Experimental study of liquid metal channel flow under the influence of a nonuniform magnetic field. *Physics of Fluids*, 18:065108, 2006.
- [87] Ch. Karcher, Y. Kolesnikov, and A. Thess. German patent DE 10 2007 038 635 B3, 12 2008.
- [88] I. E. Buceniaks. Perspectives of using rotating permanent magnets in the design of electromagnetic induction pump. *Magnetohydrodynamics*, 36(2):151–156, 2000.
- [89] I. E. Buceniaks. High pressure and high flowrate induction pumps with permanent magnets. *Magnetohydrodynamics*, 39(4):411–418, 2003.
- [90] I. Buceniaks and K. Kravalis. Efficiency of EM induction pumps with permanent magnets. *Magnetohydrodynamics*, 47(1):89–96, 2011.
- [91] K. Kravalis I. Buceniaks and R. Krishbergs. Pressure-flow rate characteristics of the pumps with permanent magnets. *Magnetohydrodynamics*, 47(1):97–104, 2011.
- [92] R. Ricou and Vives C. Local velocity and mass transfer measurements in molten metals using an incorporated magnet probe. *International Journal of Heat and Mass Transfer*, 25(10):15791588, 1982.

- [93] U. Müller and L. Bühler. *Magneto-fluid-dynamics in Channels and Containers*. Springer, 2001.
- [94] *Magnetohydrodynamics*. Kulver Academic Publishers, 1990.
- [95] Michel Rivero. Análisis de dispositivos magnetohidrodinámicos de bombeo. Master’s thesis, Centro de Investigación en Energía, UNAM, 2008.
- [96] R. Moreau, S. Smolentsev, and S. Cuevas. Flow in an insulating rectangular duct at the entry of a magnet. *Magnetohydrodynamics*, 45(2):181–192, 2009.
- [97] R. Moreau, S. Smolentsev, and S. Cuevas. MHD flow in an insulating rectangular duct under a non-uniform magnetic field. *PMC Physics B*, 3:1–43, 2010.
- [98] Signal Processing S.A. DOP 3010 Manual.
- [99] S. Asai. Birth and recent activities of electromagnetic processing of materials. *ISIJ International*, 12:981–992, 1989.
- [100] S. Asai. Recent development and prospect of electromagnetic processing of materials. *Science and Technology of Advanced Materials*, 1(4):191, 2000.
- [101] *McGraw Hill Encyclopedia of Science & Technology*. McGraw Hill, 2007.
- [102] H. Maecker. *The Electric Arc*.
- [103] <http://simap.avantagemedia.com/lectures.php>.
- [104] S. Molokov, R. Moreau, K. Moffatt, S. Eckert, A. Cramer, and G. Gerbeth. Velocity measurement techniques for liquid metal flows. In *Magnetohydrodynamics*, volume 80 of *Fluid Mechanics and Its Applications*, pages 275–294. Springer Netherlands, 2007.
- [105] Y. Takeda. Velocity profile measurement by ultrasound doppler shift method. *International Journal of Heat and Fluid Flow*, 7(4):313 – 318, 1986.
- [106] Y. Takeda. Development of an ultrasound velocity profile monitor. *Nuclear Engineering and Design*, 126(2):277 – 284, 1991.
- [107] S. Eckert, G. Gerbeth, and V.I. Melnikov. Velocity measurements at high temperatures by ultrasound doppler velocimetry using an acoustic wave guide. *Experiments in Fluids*, 35:381–388, 2003. 10.1007/s00348-003-0606-0.
- [108] Hans J Schneider-Muntau and Hitoshi Wada, editors. *Materials Processing In Magnetic Fields*. World Scientific, 2005.
- [109] P. Nikrityuk, K. Eckert, and R. Grundmann. Contactless mixing of liquid metals. *Metallurgical and Materials Transactions B*, 41:94–111, 2010.

- [110] P. A. Davidson. Magnetohydrodynamics in material processing. *Annual Review of Fluid Mechanics*, 31:273–300, January 1999.
- [111] P. Rudolph. Travelling magnetic fields applied to bulk crystal growth from the melt: The step from basic research to industrial scale. *Journal of Crystal Growth*, 310(7-9):1298–1306, 2008.
- [112] R. Lantzsch, V. Galindo, I. Grants, C. Zhang, O. Pätzold, G. Gerbeth, and M. Stelter. Experimental and numerical results on the fluid flow driven by a traveling magnetic field. *Journal of Crystal Growth*, 305:249–256, July 2007.
- [113] A. Cramer, J. Pal, K. Koal, S. Tschisgale, J. Stiller, and G. Gerbeth. The sensitivity of a travelling magnetic field driven flow to axial alignment. *Journal of Crystal Growth*, 321(1):142 – 150, 2011.
- [114] V. Galindo, I. Grants, R. Lantzsch, O. Pätzold, and G. Gerbeth. Numerical and experimental modeling of the melt flow in a traveling magnetic field for vertical gradient freeze crystal growth. *Journal of Crystal Growth*, 303:258–261, May 2007.
- [115] C. Zhang, S. Eckert, and G. Gerbeth. The impact of a vertically traveling magnetic field on the flow in a cylindrical liquid metal bubble plume. *Metallurgical and Materials Transactions B*, 40:700–711, 2009.
- [116] Z. Min, J. Shen, L. Wang, and L. Liu. Effect of traveling magnetic field on dendrite growth of Pb-Sn alloy during directional solidification. *Transactions of Nonferrous Metals Society of China*, 21(9):1976 – 1980, 2011.
- [117] X. Wang, Y. Fautrelle, J. Etay, and R. Moreau. A Periodically Reversed Flow Driven by a Modulated Traveling Magnetic Field: Part I. Experiments with GaInSn. *Metallurgical and Materials Transactions B*, 40:82–90, February 2009.
- [118] X. Wang, R. Moreau, J. Etay, and Y. Fautrelle. A periodically reversed flow driven by a modulated traveling magnetic field: Part II. Theoretical model. *Metallurgical and Materials Transactions B*, 40:104–113, 2009.
- [119] R.U. Barz, G. Gerbeth, U. Wunderwald, E. Buhrig, and Yu.M. Gelfgat. Modelling of the isothermal melt flow due to rotating magnetic fields in crystal growth. *Journal of Crystal Growth*, 180(34):410 – 421, 1997.
- [120] I. Grants and G. Gerbeth. Stability of axially symmetric flow driven by a rotating magnetic field in a cylindrical cavity. *Journal of Fluid Mechanics*, 431:407–426, March 2001.
- [121] I. Grants and G. Gerbeth. Experimental study of non-normal nonlinear transition to turbulence in a rotating magnetic field driven flow. *Physics of Fluids*, 15(10):2803–2809, 2003.

- [122] S. Steinbach and L. Ratke. The effect of rotating magnetic fields on the microstructure of directionally solidified Al-Si-Mg alloys. *Materials Science and Engineering A*, 413-414:200–204, 2005.
- [123] C. Zhang, V. Shatrov, J. Priede, S. Eckert, and G. Gerbeth. Intermittent behavior caused by surface oxidation in a liquid metal flow driven by a rotating magnetic field. *Metallurgical and Materials Transactions B*, 42:1188–1200, 2011.
- [124] Y. M. Gelfgat and A. Y. Gelfgat. Experimental and numerical study of rotating magnetic field driven flow in cylindrical enclosures with different aspect ratios. *Magnetohydrodynamics*, 40:147–160, June 2004.
- [125] K. Mazuruk, N Ramachandran, M.P. Volz, and D. Gillies. Study of frequency effects of a rotating magnetic field on fluid flow in vertical cylinders. In *Materials Research in Low Gravity*, volume 3123 of *Proceedings of SPIE*, pages 262–271.
- [126] R. Rakoczy and S. Masiuk. Influence of transverse rotating magnetic field on enhancement of solid dissolution process. *American Institute of Chemical Engineers Journal*, 56(6):1416–1433, 2010.
- [127] R. Rakoczy and S.Masiuk. Studies of a mixing process induced by a transverse rotating magnetic field. *Chemical Engineering Science*, 66(11):2298 – 2308, 2011.
- [128] S. Eckert, P.A. Nikrityuk, D. Rübiger, K. Eckert, and G. Gerbeth. Efficient melt stirring using pulse sequences of a rotating magnetic field: Part I. Flow field in a liquid metal column. *Metallurgical and Materials Transactions B*, 38:977–988, 2007.
- [129] K. Mazuruk. Control of melt convection using traveling magnetic fields. *Advances in Space Research*, 29(4):541–548, 2002.
- [130] S. Eckert, B. Willers, P.A. Nikrityuk, K. Eckert, U. Michel, and G. Zouhar. Application of a rotating magnetic field during directional solidification of Pb-Sn alloys: Consequences on the CET. *Materials Science and Engineering: A*, 413414(0):211 – 216, 2005.
- [131] P.A. Nikrityuk, K. Eckert, and R. Grundmann. A numerical study of unidirectional solidification of a binary metal alloy under influence of a rotating magnetic field. *International Journal of Heat and Mass Transfer*, 49(78):1501 – 1515, 2006.
- [132] V. Metan, K. Eigenfeld, D. Rübiger, M. Leonhardt, and S. Eckert. Grain size control in Al-Si alloys by grain refinement and electromagnetic stirring. *Journal of Alloys and Compounds*, 487(12):163 – 172, 2009.

- [133] B. Willers, S. Eckert, P.A. Nikrityuk, D. Rübiger, J. Dong, K. Eckert, and G. Gerbeth. Efficient melt stirring using pulse sequences of a rotating magnetic field: Part II. Application to solidification of Al-Si alloys. *Metallurgical and Materials Transactions B*, 39:304–316, 2008.
- [134] W.D. Griffiths and D.G. McCartney. The effect of electromagnetic stirring during solidification on the structure of Al-Si alloys. *Materials Science and Engineering: A*, 216(12):47 – 60, 1996.
- [135] P. Dold and K.W. Benz. Rotating magnetic fields: fluid flow and crystal growth applications. *Progress in Crystal Growth and Characterization of Materials*, 38(1):7–38, 1999.
- [136] R. Rakoczy and S. Masiuk. Experimental study of bubble size distribution in a liquid column exposed to a rotating magnetic field. *Chemical Engineering and Processing: Process Intensification*, 48(7):1229 – 1240, 2009.
- [137] A. Cramer, S. Eckert, V. Galindo, G. Gerbeth, B. Willers, and W. Witke. Liquid metal model experiments on casting and solidification processes. *Journal of Materials Science*, 39:7285–7294, 2004.
- [138] J. Pal, A. Cramer, Th. Gundrum, and G. Gerbeth. MULTIMAG - A MULTI-purpose MAGnetic system for physical modelling in magnetohydrodynamics. *Flow Measurement and Instrumentation*, 20(6):241 – 251, 2009.
- [139] T. Vogt, I. Grants, D. Rübiger, S. Eckert, and G. Gerbeth. On the formation of Taylor-Göetler vortices in RMF-driven spin-up flows. *Experiments in Fluids*, 52:1–10, 2012.
- [140] A.Yu. Gelfgat, P.Z. Bar-Yoseph, and A. Solan. Effect of axial magnetic field on three-dimensional instability of natural convection in a vertical bridgman growth configuration. *Journal of Crystal Growth*, 230(12):63 – 72, 2001.
- [141] A. Y. Gelfgat. On three-dimensional instability of a traveling magnetic field driven flow in a cylindrical container. *Journal of Crystal Growth*, 279:276–288, June 2005.
- [142] I. Grants and G. Gerbeth. Linear three-dimensional instability of a magnetically driven rotating flow. *Journal of Fluid Mechanics*, 463:229–239, July 2002.
- [143] P. A. Davidson. Analytical models of rotary electromagnetic stirring. *Journal of Mathematics Applied in Business and Industry*, 7:89–108, 1996.
- [144] P. Nikrityuk, K. Eckert, and R. Grundmann. Numerical study of a laminar melt flow driven by a rotating magnetic field in enclosed cylinders with different aspect ratios. *Acta Mechanica*, 186:17–35, 2006.

- [145] K. Fraňa, J. Stiller, and K. Horáková. A numerical study of flows driven by a rotating magnetic field in a square container. *Proceedings in Applied Mathematics and Mechanics*, 8(1):10953–10954, 2008.
- [146] V. Travnikov, K. Eckert, P.A. Nikrityuk, S. Odenbach, T. Vogt, and S. Eckert. Flow oscillations driven by a rotating magnetic field in liquid metal columns with an upper free surface. *Journal of Crystal Growth*, 339(1):52 – 60, 2012.
- [147] Marius Ungarish. The spin-up of liquid metal driven by a rotating magnetic field. *Journal of Fluid Mechanics*, 347:105–118, 1997.
- [148] Petr A. Nikrityuk, Sven Eckert, and Kerstin Eckert. Spin-up and spin-down dynamics of a liquid metal driven by a single rotating magnetic field pulse. *European Journal of Mechanics - B/Fluids*, 27(2):177 – 201, 2008.
- [149] D. Rübiger, S. Eckert, and G. Gerbeth. Measurements of an unsteady liquid metal flow during spin-up driven by a rotating magnetic field. *Experiments in Fluids*, 48:233–244, 2010.
- [150] John A. S. Green, editor. *Aluminum Recycling and Processing for Energy Conservation and Sustainability*. ASM International, 2007.
- [151] K.-H. Müller, G. Krabbes, J. Fink, S. Gruß, A. Kirchner, G. Fuchs, and L. Schultz. New permanent magnets. *Journal of Magnetism and Magnetic Materials*, 226230, Part 2(0):1370 – 1376, 2001. Proceedings of the International Conference on Magnetism (ICM 2000).
- [152] J.M.D. Coey. Permanent magnet applications. *Journal of Magnetism and Magnetic Materials*, 248(3):441 – 456, 2002.
- [153] Advanced Magnetic Materials. www.rare-earth-magnets.com.
- [154] China Rare Earth Magnet Ltd. www.permanentmagnet.com.
- [155] J. F. Liu, Y. Ding, Y. Zhang, D. Dimitar, F. Zhang, and G. C. Hadjipanayis. New rare-earth permanent magnets with an intrinsic coercivity of 10 kOe at 500 °C. *Journal of Applied Physics*, 85(8), 1999.
- [156] L. Peng, Q. Yeng, H. Zhang, G. Xu, M. Zhang, and J. Wang. Rare earth permanent magnets $\text{Sm}_2(\text{Co}, \text{Fe}, \text{Cu}, \text{Zr})_{17}$ for high temperature applications. *Journal of Rare Earths*, 26(3):378 – 382, 2008.
- [157] Charles Vivès. Elaboration of metal matrix composites from thixotropic alloy slurries using a new magnetohydrodynamic caster. *Metallurgical Transactions B*, 24B:493–510, 1993.

- [158] X.D. Wang, T.J. Li, Y. Fautrelle, M.D. Dupouy, and J.Z. Jin. Two kinds of magnetic fields induced by one pair of rotating permanent magnets and their application in stirring and controlling molten metal flows. *Journal of Crystal Growth*, 275(12):e1473 – e1479, 2005.
- [159] A. Bojarevics and T. Beinerts. Experiments on liquid metal flow induced by a rotating magnetic dipole. *Magnetohydrodynamics*, 46(4):333–338, 2012.
- [160] V. W. Ekman. On the influence of the earth’s rotation on ocean currents. *Arkiv för matematik, astronomi och fysik*, 2(11):1–52, 1905.
- [161] A. D. Chepelianskii, F. Chevy, and E. Raphaël. Capillary-gravity waves generated by a slow moving object. *Physical Review Letters*, 100:074504, February 2008.
- [162] M. A. Sutton, J.-J. Orteu, and H. Schreier. *Image Correlation for Shape, Motion and Deformation Measurements: Basic Concepts, Theory and Application*. Springer, 2009.
- [163] Alberto Beltrán Morales. *Dinámica de Flujos en Obstáculos Magnéticos*. PhD thesis, Universidad Nacional Autónoma de México, Sep 2010.
- [164] N. B. Morley, J. Burris, L. C. Cadwallader, and M. D. Nornberg. Gainsn usage in the research laboratory. *Review of Scientific Instruments*, 79(5), 2008. cited By (since 1996) 7.
- [165] J. A. Shercliff. *A Textbook of Magnetohydrodynamics*. Pergamon Press, 1965.
- [166] W. F. Hughes and F. J. Young. *Electromagnetodynamics of Fluids*. Krieger Publishing Company, 1989.